DISSERTATION

submitted to the
Combined Faculty of Mathematics, Engineering
and Natural Sciences
of
Heidelberg University,
Germany

for the degree of
Doctor of Natural Sciences

Put forward by
Claudius Leander Rosendahl, M.Sc.
born in Stuttgart

Oral examination: July 12, 2022

Proxy to fossil-fuel CO_2 emission ratios: in-situ versus inventory data

Referees:

Prof. Dr. Ingeborg Levin
Prof. Dr. Werner Aeschbach

Erklärung

Hiermit erkläre ich, dass ich die eingereichte Dissertation selbständig verfasst und keine anderen als die angegebenen Hilfsmittel benutzt habe. Alle wörtlich oder inhaltlich übernommenen Stellen sind als solche gekennzeichnet.

Heidelberg, den 14. Juli 2022

Claudius Leander Rosendahl

Abstract

Are inventory-based CO to fossil fuel CO_2 and NO_x to fossil fuel CO_2 emission ratios correct? Three measurement campaigns are conducted for this thesis, investigating highway traffic and residential heating to find their sector-dominated CO to fossil fuel CO_2 and NO_x to fossil fuel CO_2 emission ratios.

Two mobile laboratories equipped with ten meter tall masts are used to ensure proximity to the emitters in order to isolate emissions from the sector in question. The determined sector-dominated effective atmospheric emission ratios are compared to emission ratios from an emission inventory. The long-term trend of measured CO emission ratios in Heidelberg are evaluated and compared to modelled CO emission ratios based on an inventory combined with an atmospheric transport model.

It is found that CO emissions from highway traffic are underestimated by the inventory. Correcting the modelled CO emission ratios with the highway traffic results leads to a better agreement between measured and modelled CO emission ratios for the long-term trend. These results call for an investigation of the problem by the traffic modelling community.

Kurzfassung

Sind die Verhältnisse von CO und NO_x zu fossilem CO_2 in Emissionsinventaren korrekt? Drei Messkampagnen werden im Zuge dieser Arbeit durchgeführt, die für Autobahnverkehr und Heizungen diese Emissionsverhältnisse feststellen.

Zwei mobile, mit zehn Meter hohen Masten ausgestattete Labors werden eingesetzt, um die Nähe zu den Emittenten zu gewährleisten und die Emissionen des jeweiligen Sektors zu isolieren. Die ermittelten sektorbezogenen Emissionsverhältnisse werden dann mit den Emissionsverhältnissen aus einem Emissionsinventar verglichen. Der langfristige Trend der gemessenen CO-Emissionsverhältnisse in Heidelberg wird ausgewertet und mit modellierten CO-Emissionsverhältnissen verglichen, die auf einem Inventar in Kombination mit einem atmosphärischen Transportmodell basieren.

Die Ergebnisse der Autobahnmesskamagne zeigen, dass CO Emissionen vom Emissionsinventar unterschätzt werden. Korrigiert man die modellierten CO-Emissionsverhältnissen mit den Ergebnissen der Autobahnkampagne, führt dies zu einer besseren Übereinstimmung zwischen gemessenen und modellierten CO-Emissionsverhältnissen für den langfristigen Trend. Dieses Ergebnis sollte von der Verkehrsmodellierungscommunity weiter untersucht werden.

Table of contents

Chapter 1

Introduction

The climate on our planet experiences continuous change. On geological time scales, change is linked to Earth's orbit (Paillard, 2001). The largest variations are glacial and inter-glacial cycles. While the sun is the most significant driver of this system, the interconnections between hydrosphere, cryosphere, biosphere, atmosphere, and lithosphere bring nonlinear responses to the sun's radiative forcing (Beer et al., 2000).

The atmosphere has a special role when it comes to radiative forcing. Depending on the wavelength of the incoming light, gases may interact with radiation. If a gas has absorption lines in the infrared spectrum, it is called a greenhouse gas. Greenhouse gases effectively trap radiation close to the surface by absorbing radiation from the Earth's surface, known as the greenhouse effect. The most important greenhouse gas is CO_2 (IPCC, 2014), not because it is the most efficient greenhouse gas, CH_4 for instance, cause more additional radiative forcing per molecule on the timescale of a century, but because it is the most abundant. Its abundance is directly linked to its atmospheric lifetime, i.e. the duration it stays in the atmosphere, which can be in the order of hundreds to thousands of years (Archer et al., 2009). As long as no major emissions such as volcanic eruptions disturb the equilibrium, interactions between biosphere and hydrosphere keep the CO_2 in balance.

Anthropogenic emissions of CO_2 through the burning of fuels, especially fossil fuels, lead to increased concentrations in the atmosphere. Charles David Keeling was the first to report increasing CO_2 concentrations at Mauna Loa in Hawaii in 1958 (Hofmann et al., 2009). Humanity has used fire for more than a million years (Gowlett, 2016), but only in the last 250 years the CO_2 concentration has increased at an unprecedented rate, that is, when fossil fuels became the energy source of the industrial revolution. Yearly emissions of gigatons of CO_2 previously stored underground into the atmosphere disrupts the equilibrium between the atmosphere and, e.g. the ocean and the biosphere. The increase in radiative forcing due to CO_2 from fossil fuel burning could have catastrophic consequences for humanity. Industrialised countries have recognised the danger of climate change and began reducing CO_2 emissions.

1.1 Motivation

In order to check if pledged emission reduction goals are reached, countries of the United Nations established the United Nations Framework Convention on Climate Change (UNFCCC, 2022). Yearly National Inventory Reports (NIR, 2022) are submitted to the UNFCCC. The NIR are based on consumption statistics and calculations according to guidelines of the Intergovernmental Panel for Climate Change (Intergonvernmental Panel on Climate Change, 2022). The general formula is $E = F \cdot A$. The emission E is equivalent to the activity A multiplied with an emission factor F.

Activity is an overarching term and describes something different for every sector. Some examples are mass of coal burned in power plants for heat and electricity, sum of driven kilometers in the traffic sector, and number of livestock in agriculture. Even though the equation is simple, determining A and F is a complex problem, requiring measurements and models to obtain good estimates. NIRs are the data basis for emission inventories. Emission inventories spatially disaggregate the emissions to model surface flux emission maps.

Atmospheric greenhouse gas concentrations are an independent measure of emissions. Linking atmospheric CO_2 concentration enhancements to anthropogenic (human made) fossil fuel combustion emissions is challenging because of the interactions of CO_2 with the biosphere (Miles et al., 2021). Respiration and photosynthesis can lead to strong fluctuations of CO_2 concentrations. Separating biospheric CO_2 ($bioCO_2$) and fossil fuel CO_2 ($ffCO_2$) is therefore essential. The state-of-the-art method involves measuring $^{14}CO_2$ (Levin et al., 2003), an isotope that can be found in $bioCO_2$ but is completely absent in $ffCO_2$ due to its radioactive decay with a half-life time of 5730 years. Measuring $^{14}CO_2$ is laborious and costly. In consequence, quasi-continuous measurements rely on weekly or bi-weekly accumulated samples. This poses a problem for models.

Inverse atmospheric models estimate *a posteriori* surface fluxes of $ffCO_2$ by updating *a priori* surface fluxes from emission inventories with atmospheric concentration measurements using Bayesian statistics (Joyce, 2021; Bayes, 1764). This requires atmospheric $ffCO_2$ concentration measurements on an hourly timescale, but the current technology only allows for weekly or biweekly measurements. One proposed solution to this problem is inferring $ffCO_2$ concentrations from concentrations of gas species co-emitted in combustion (Levin and Karstens, 2007; Vogel et al., 2010; Super et al., 2017). These so-called proxy gases, e.g. CO and NO_x, can easily be measured on an hourly timescale. To estimate $ffCO_2$, the proxy/$ffCO_2$ emission ratios have to be determined precisely.

Inventory emission ratios are directly coupled to emission factors. When calculating an emission ratio of a proxy R_{proxy} for a sector

$$R_{\text{proxy}} = \frac{E_{\text{proxy}}}{E_{\text{ffCO}_2}} = \frac{\frac{E_{\text{proxy}}}{A}}{\frac{E_{\text{ffCO}_2}}{A}} = \frac{F_{\text{proxy}}}{F_{\text{ffCO}_2}},$$

the activity A cancels out. Determining F_{ffCO_2} is comparatively easy, because besides H_2O, ffCO_2 is one of two main products of the fossil fuel combustion. If the carbon content of the educts (fuel) are known and the fuel is fully oxidised, calculating the emission factor is straight-forward. However, fuels are usually not fully oxidised. Hence, in addition, a small fraction of CO is produced. Determining F_{proxy}, e.g. F_{CO} precisely is challenging, because it depends strongly on combustion conditions. While F_{ffCO_2} may change by 0.1 to 1 %, depending on oxygen availability, F_{CO} changes by a factor of 10 simultaneously. Emission factors for inventories necessarily depend on models that inherently contain uncertainties. e.g. in the traffic sector (Hausberger et al., 2009), a sample of vehicles is tested for each vehicle group. From the test data, the Passenger Car Heavy duty Emission Model (PHEM) estimates emission factors. Hausberger et al. (2009) list three categories of uncertainties related to (1) the sample of vehicles for each group, (2) the model and (3) other problems like cold start conditions, fuel influence, load conditions et cetera.

Atmospheric measurements can be an independent check of proxy/ffCO_2 emission ratios. Many studies already investigated atmospheric emission ratios (Zondervan and Meijer, 1996; Potosnak et al., 1999; Levin and Karstens, 2007; Djuricin et al., 2010; Vogel et al., 2010; Newman et al., 2013; Janssen et al., 2013; Gamnitzer et al., 2006; Turnbull et al., 2006; Vollmer et al., 2007; Graven et al., 2009; Turnbull et al., 2015) for different reasons. However, proxy/ffCO_2 emission ratios are source dependent, spatially heterogeneous and ever-changing. Consequently, continuous monitoring and investigation of atmospheric proxy/ffCO_2 emission ratios is necessary.

1.2 State of the art

Quantification of surface flux via emission inventories is the foundation of ffCO_2 monitoring. Necessary independent verification is possible with inverse atmospheric models. The models require continuous ffCO_2 concentration measurements, a feat that can only be achieved indirectly by using proxy gases and their corresponding emission ratios.

Emission inventory. A multitude of emission inventories are publicly available. However, no two emission inventories are the same and differences already arise just by what is included and what is not (Andrew, 2020). In the following I list a few prominent emission inventories and their corresponding institutions.

- Open-source Data Inventory for Anthropogenic CO_2 (ODIAC), National Institute for Environmental Studies, Japan (ODIAC, 2022)
- Carbon Dioxide Information Analysis Center inventory (CDIAC), U.S. Department of Energy (CDIAC, 2022)
- Emissions Database for Global Atmospheric Research (EDGAR), Joint Research Centre of the European Commission (EDGAR, 2022)
- Copernicus Atmosphere Monitoring Service REGional inventory (CAMS-REG), Netherlands Organisation for Applied Scientific Research (TNO) (Kuenen et al., 2022)
- Hestia, National Institute for Standards and Technology, U.S.A. (Hestia, 2022)

ODIAC estimates global $ffCO_2$ emissions based on satellite nighttime light data and individual power plant emission/location profiles (ODIAC, 2022). CDIAC uses energy statistics provided by the United Nations to estimate global $ffCO_2$ emissions (CDIAC, 2022). EDGAR uses international statistics as well, but provides information on other greenhouse gases in addition to $ffCO_2$ by using a consistent IPCC methodology (EDGAR, 2022). CAMS-REG is based on National Inventory Reports instead of energy statistics and is a European, not a global emission inventory (Kuenen et al., 2022). Hestia is a high-resolution, city-level emission inventory for US cities, e.g. Indianapolis (Gurney et al., 2012).

Ratio measurements. Emission ratios can only be determined if proxy gases and $ffCO_2$ are measured simultaneously. There is a wide range of instruments capable of measuring CO and CO_2 – but not $ffCO_2$ – at high temporal resolution using characteristic light absorption to determine concentrations. Two examples are the Fourier-transform infrared spectrometer (FTIR, Griffith (1996); Hammer et al. (2013)) and the cavity ring-down spectrometer (CDRS Busch and Busch (1999)). For NO_x, inexpensive in-situ instruments are also readily available, e.g. the ICAD instruments used in the measurement campaigns (Horbanski et al., 2019). Directly measuring $ffCO_2$ is currently not possible, instead air samples have to be collected. CO_2 is extracted from the air samples cryogenically, before it is graphitised to carbon. The graphitised carbon is then analysed for ^{14}C either by low-level counting (LLC, Kromer and

Münnich (1992)) or isotope measurements with an accelerator mass spectrometer (AMS, Miller et al. (2013); Hammer et al. (2017)). Lux (2018) describes the processing at the Heidelberg Central Radiocarbon Laboratory of the Integrated Carbon Observation System (ICOS CRL, 2022). The same methods are used all over the world, cf. Turnbull et al. (2015, 2017); Levin and Rödenbeck (2008).

Proxy ratios in previous studies. Traffic studies often only measure CO_2, not ffCO_2, since 5 % or less of the CO_2 is non-fossil (Popa et al., 2014; Ammoura et al., 2014). Two prominent methods to determine traffic emission ratios are tailpipe emission measurements (Bishop and Stedman, 2008; Vollmer et al., 2010) and tunnel studies (Vollmer et al., 2007). Today, tailpipe measurements are performed during real driving conditions by portable emission measurement systems (PEMS) in the vehicle, that capture exhaust gases directly and analyse them on board (Weiss et al., 2012). Besides PEMS, test-stand measurements can be used to determine traffic emission factors. Keller et al. (2017) model traffic emission factors for Austria, Germany, and Switzerland based on such measurements. Tunnel studies typically use two measurement stations, one at medium distance to the entrance and one close to the exit of a one directional car tunnel (Vollmer et al., 2007; Popa et al., 2014). Bradley et al. (2000) used an Open Path FTIR (i.e. the light path is across the street) to measure absolute emission ratios. While emission ratios are usually determined by dividing CO enhancement by CO_2 enhancement (Popa et al., 2014), here total concentrations were divided. The two in-situ methods, tailpipe measurements and tunnel measurements, are suitable to investigate some aspects of traffic emissions. However, tailpipe emissions are limited to individual vehicles and capture the gas before any atmospheric chemistry processes take effect. Tunnel studies are physically limited to tunnels.

The approach in this thesis yields an effective average traffic emission ratio, representative for a highway traffic signal that reaches a potential measurement station. The distinction 'effective' is important, since traffic plumes that reach a measurement station have been affected by some atmospheric chemistry, e.g. the interaction of CO with OH (Crutzen and Fishman, 1977). With the accompanying traffic count data and the month-long continuous measurements, separate ratios for heavy duty vehicles and passenger cars can be identified. The fleet composition is crucial for the measured emission ratio, a fact that was omitted, overseen or not quantifiable in previous studies.

Studies of residential heating usually focus on comparing stoves or boilers (Johansson et al., 2004; McDonald, 2009; Win et al., 2012) in test-bed environments. However, even when residential areas are studied, the focus is not on residential heating emission ratios (Helfter et al., 2016). To the best of my knowledge, no study focusing on effective atmospheric emission ratios from residential heating exists to date.

Once proxy/ffCO_2 emission ratios are determined, they help to improve the ability to detect ffCO_2 concentration enhancements (ΔffCO_2) in the atmosphere. Proxies have improved the temporal resolution of ΔffCO_2 (Levin and Karstens, 2007), the spatial localisation of ΔffCO_2 plumes, estimation of ΔffCO_2 emissions from satellite measurements (Reuter et al., 2019; Konovalov et al., 2016), and the sectoral attribution of ΔffCO_2 (Turnbull et al., 2015).

Levin and Karstens (2007) showed that continuous CO measurements can be used as a proxy for regional ΔffCO_2. They estimated uncertainties between 20 % and 40 % for hourly ffCO_2 values. In satellite studies, proxy measurements are used for constraining the spatial extent of urban or industrial CO_2 plumes (Reuter et al., 2019). Konovalov et al. (2016) developed an inverse modelling method using satellite proxy measurements and emission inventory NO_x/ffCO_2 ratios to estimate ffCO_2. These examples demonstrate the broad application range of ffCO_2 proxies.

As part of the INdianapolis FLUX experiment (INFLUX) (Miles et al., 2021; Davis et al., 2017; Richardson et al., 2017; Miles et al., 2017; Cambaliza et al., 2015), Turnbull et al. (2015) use CO_2, CO, and $^{14}CO_2$ in-situ measurements from tall towers in and around the city to quantify urban emissions. With the emission inventory developed by Gurney et al. (2012) and the tall tower measurements, Lauvaux et al. (2016) designed a high-resolution inversion system to estimate the carbon budget of Indianapolis. INFLUX is one of the largest comprehensive experiments investigating anthropogenic urban emissions. Turnbull et al. (2015) used characteristic ΔCO/ΔffCO_2 ratios to identify the contribution of different source sectors over the course of a day. The measurements have also been used to evaluate inventory-based CO/ffCO_2 ratios for the traffic sector.

Modern emission inventories can provide ffCO_2 as well as proxy gas emissions. The ratio between proxy gas emissions and ffCO_2 emissions contain uncertainties originating in the emission factors of the proxy gas and – to a lesser degree – the emission factors of ffCO_2. Consequently, independent verification in the form of atmospheric measurements is necessary. Although many studies on atmospheric proxy/ffCO_2 emission ratios exist, none focus on residential heating and most that focus on traffic are either restricted to individual vehicles or tunnels and thus cannot capture traffic emissions in all their complexity. Long-term comparisons of proxy/ffCO_2 emission ratios between measurements and inventories are necessary to check the consistency over an extended time period. Unfortunately, long-term $^{14}CO_2$ records for (semi-)polluted measurement stations are rare. However, for Heidelberg such a record exists.

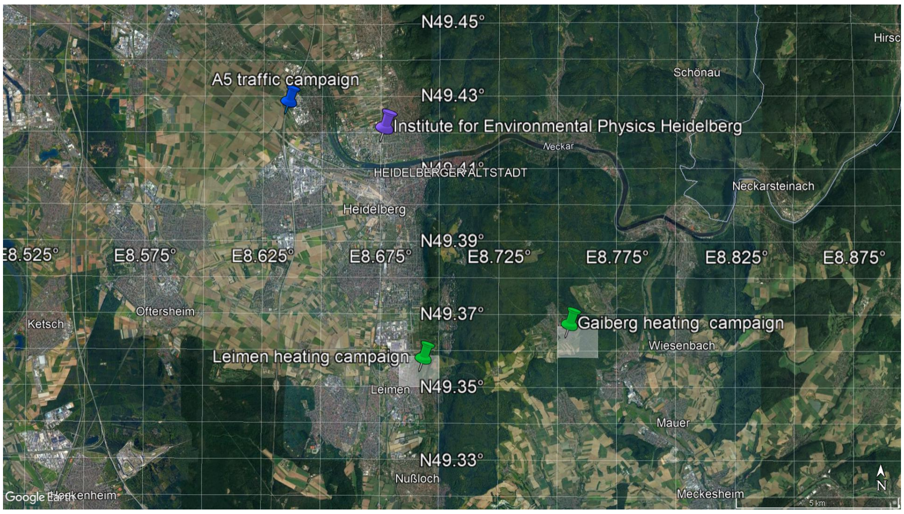

Fig. 1.1 Overview of the campaign sites. White rectangles indicate emission inventory cells used for comparison with collected data.

1.3 Objectives and structure

This thesis aims to provide a quantitative comparison of inventory-based proxy to ffCO$_2$ emission ratios with atmospheric effective Δproxy/ΔffCO$_2$ ratios. To this end, sector-dominated emission ratios were measured in three campaigns: two for the heating sector, one for highway traffic. For this purpose, two semi-mobile laboratories, capable of sample collection for ^{14}C analysis and continuous trace gas measurements of CO$_2$, CO, CH$_4$, NO$_x$, and NO$_2$ using spot samples (also denoted flasks) are built for the three campaigns. The campaigns are conducted in proximity to Heidelberg (Fig. 1.1). Their goal is to (1) demonstrate that in-situ measurements of sector-dominated Δproxy/ΔffCO$_2$ ratios is possible and (2) use the measured data to verify proxy/ΔffCO$_2$ ratios provided by the emission inventory of TNO (Kuenen et al., 2014). This novel approach brings new insight because it determines effective atmospheric proxy/ffCO$_2$ emission ratios, i.e. emission ratios as they would be measured at in-situ measurement stations. In addition, a 15-year time series of ffCO$_2$ at the Heidelberg measurement site is analyzed to investigate the long-term ΔCO/ΔffCO$_2$ trend.

Chapter 2 describes the conceptual and methodical tools used to answer the questions above. Chapters 3 and 4 present a traffic campaign at the A5 highway and two heating campaigns in Leimen and Gaiberg, respectively. The sections for each campaign are structured in the same way, starting with a description of the campaign site, followed by results, discussion, and perspectives. Both heating campaigns are discussed jointly. Chapter 5 describes the comparison of long-term trends in measured and modelled CO/ffCO$_2$ emission ratios in Heidelberg. Finally, in Chapter 6 I conclude the thesis by bringing the results from campaigns and long-term record into perspective. The appendices contain detailed information about the instruments used during the campaigns (Appendix A), the quality check of the traffic campaign (Appendix B), and the data used in the long-term record calculations (Appendix C).

Chapter 2

Background and methods

This chapter introduces theoretical concepts behind the measurements and models used in this thesis. Relevant atmospheric trace and proxy gases are discussed. The measurement principles for proxy/ffCO_2 emission ratios and the corresponding modelling approach are presented. Additionally, intricacies of the used emission inventory concerning the two sectors of interest – traffic and residential heating – are discussed. Calculations of average emission ratios, a dispersion model and wind direction statistics are presented.

Experimental design is the key to successful measurement campaigns. In-situ measurements are unable to distinguish between CO_2 from different sources, e.g. traffic or a coal-fired power plant. Focusing on one sector, e.g. residential heating, requires spatial and/or temporal separation from sources of other sectors. Consequently, the conducted measurement campaigns were designed to maximise temporal and spatial separation in order to measure sector-dominated emission ratios with as little interference from other sectors as possible.

2.1 Atmospheric tracers and proxies

Environmental physics as a field relies heavily on tracers and proxies to reconstruct natural processes and phenomena. Tracers are substances that are are present in processes, sometimes substituting other molecules or elements without affecting the process itself. A good example is dying a water stream with a chemically inert dye. Proxies of species are produced in the same environment and by the same process, but in a different chemical reaction. For instance, CO as a proxy for CO_2 where their only difference is that CO is not fully oxidised. In other words, tracers *trace* processes, while proxies are *stand-ins* for the gas species of interest.

Radon. ^{222}Rn is progeny of ^{238}U exhaled from soils at a rate of in the order of 1 atom $cm^{-2}s^{-1}$ (Karstens et al., 2015). The exhalation rate varies depending on soil texture, local water table depth, and uranium content. For simplicity, we assume a constant exhalation rate. With a half-life of 3.83 days, ^{222}Rn is an excellent tracer for local atmospheric transport and mixing. During nightly inversions, ^{222}Rn and other trace gases accumulate in the planetary boundary layer. While accumulation of other trace gases depend on local sources, the exhalation rate of ^{222}Rn is approximately constant. Hence, the ^{222}Rn concentration increase over time only depends on the mixing height. During well mixed atmospheric conditions, ^{222}Rn is diluted, same as other trace gases.

Carbon dioxide. $^{14}CO_2$ is a tracer for fossil fuel contributions to a CO_2 enhancement. CO_2 from fossil fuel burning is chemically indistinguishable from CO_2 emitted by the biosphere. Physically, however, fossil fuel CO_2 misses the isotopologue $^{14}CO_2$ because ^{14}C is a radioactive isotope with a half-life of 5730 years[1]. The reduction of the ratio $R = {}^{14}C/{}^{12}C$ due to fossil fuel burning is called the Suess effect (Suess, 1955) and consequently, $^{14}CO_2$ can be used as a tracer of the fossil contribution to a local, temporary increase in CO_2. ^{14}C abundance is given in reference to the United States' National Bureau of Standards (NBS, now named National Institute of Standards and Technology, NIST) oxalic acid (Stuiver and Polach, 1977) as

$$\Delta = \left(\frac{R_{\text{sample}}}{R_{\text{standard}}} - 1\right) \cdot 1000\,‰. \tag{2.1}$$

With this, following Levin et al. (1989, 2003); Levin and Rödenbeck (2008); Levin et al. (2008, 2011), we can calcuate ffCO$_2$ with the following mass balance equations:

$$\begin{aligned}
{CO_2}^{\text{meas}} &= {CO_2}^{\text{bg}} + {CO_2}^{\text{bio}} + {CO_2}^{\text{nuc}} + {CO_2}^{\text{ff}} \qquad (2.2)\\
{CO_2}^{\text{meas}}(\Delta^{14}C^{\text{meas}} + 1000\,‰) &= {CO_2}^{\text{bg}}(\Delta^{14}C^{\text{bg}} + 1000\,‰)\\
&\quad + {CO_2}^{\text{bio}}(\Delta^{14}C^{\text{bio}} + 1000\,‰)\\
&\quad + {CO_2}^{\text{ff}}(\Delta^{14}C^{\text{ff}} + 1000\,‰) \qquad (2.3)\\
&\quad + {CO_2}^{\text{nuc}}(\Delta^{14}C^{\text{nuc}} + 1000\,‰)
\end{aligned}$$

where the superscript *meas* denotes the measured quantity at the station of interest, *bg* denotes to background station, *bio* denotes a biospheric origin, *nuc* denotes nuclear origin, and *ff* denotes the origin from fossil fuel. The nuclear term was added to this equation more recently (Maier et al., 2021) and was not present in the original publications (e.g. Levin et al., 2003; Levin and Rödenbeck, 2008; Levin et al., 2011).

---

[1] The isotope ^{14}C is formed in the upper troposphere in an (n,p) reaction where Nitrogen absorbs a thermal neutron ($n + {}^{14}_{7}N \rightarrow {}^{14}_{6}C + p$). ^{14}C is then oxidised in two steps to form $^{14}CO_2$, which, in return, is photosynthesised by plants, joining the biosphere carbon cycle.

The simplest solution to calculate ffCO_2 assumes no influence from nuclear sources (${CO_2}^{nuc} = 0$) and the biosphere in very close equilibrium with atmospheric CO_2, i.e. $\Delta^{14}{CO_2}^{bio} = \Delta^{14}{CO_2}^{bg}$ (Levin et al., 2003). Then, assuming $\Delta^{14}C^{ff} = -1000$ ‰, i.e. $R_{sample} = 0$ in Eq. (2.1), we obtain

$$ {CO_2}^{ff} = {CO_2}^{meas} \frac{\Delta^{14}C^{bg} - \Delta^{14}C^{meas}}{\Delta^{14}C^{bg} + 1000\,‰}. \tag{2.4} $$

Taking into account that in reality $\Delta^{14}{CO_2}^{bio} \neq \Delta^{14}{CO_2}^{bg}$, Levin and Rödenbeck (2008) used model calculations by Naegler (2005) to obtain a better estimate for $\Delta^{14}{CO_2}^{bio}$ by assuming $\Delta^{14}{CO_2}^{bio}$ in Heidelberg is comprised of roughly equal parts of heterotrophic and autotrophic respiration, i.e.

$$ \Delta^{14}{CO_2}^{bio} = 0.5 \cdot \Delta^{14}CO_2^{het} + 0.5 \cdot \Delta^{14}CO_2^{auto}, \tag{2.5} $$

where *het* and *auto* denote heterotrophic and autotrophic respiration, respectively. Naegler (2005) estimated monthly $\Delta^{14}{CO_2}^{het}$ values, whereas $\Delta^{14}{CO_2}^{auto}$ is estimated to be equal to the background, i.e. $\Delta^{14}CO_2^{bg} = \Delta^{14}CO_2^{auto}$. With this and the modelled influence of nuclear facilities (Kuderer et al., 2018), the new equation to calculate $\Delta {CO_2}^{ff}$ is

$$ \Delta {CO_2}^{ff} = \frac{{CO_2}^{bg}(\Delta^{14}C^{bg} - \Delta^{14}C^{bio}) - {CO_2}^{meas}(\Delta^{14}C^{meas} - \Delta^{14}C^{nuc} - \Delta^{14}C^{bio})}{\Delta^{14}C^{bio} + 1000\,‰}. \tag{2.6} $$

At this time, no instrument is readily available to measure $^{14}CO_2$ with high temporal resolution. The current procedure involves collection of air samples, either in Raschig-tubes or in flasks, graphitisation of CO_2, and analysis in an AMS.[2] Because this is a costly and laborious processing chain, so-called proxy gases are investigated by numerous studies (Zondervan and Meijer, 1996; Potosnak et al., 1999; Levin and Karstens, 2007; Djuricin et al., 2010; Vogel et al., 2010; Newman et al., 2013; Janssen et al., 2013; Gamnitzer et al., 2006; Turnbull et al., 2006). Proxy gases are co-emitted during combustion and can typically be measured relatively easily, continuously, and cheaply. An ideal proxy for the present case would have no sources other than combustion of fossil fuels (i.e. is chemically inert) with a constant Δproxy/ΔffCO_2 emission ratio and a short life time (hours). The proxy gases used in this thesis are CO and NO_x. Their characteristics will be described in the following.

In general, the emission ratios of proxy gases depend on many factors, e.g. source type, fuel, combustion conditions, or after-treatment of exhaust gases. A

---

[2] A detailed description of the whole workflow is beyond the scope of this thesis but is given by Lux (2018).

particular challenge is bio-fuel burning, which increases proxy concentrations while not increasing $ffCO_2$, and hence increasing the proxy emission ratios. New technologies such as new catalysts, increases in combustion efficiency, or changes in heating systems, constantly change proxy emission ratios creating a need for new studies. While many studies focus only the transport sector (Ammoura et al., 2014; Popa et al., 2014; Vollmer et al., 2007; Bradley et al., 2000), because it is one of the largest contributors to climate change and air pollution, I additionally measured residential heating emissions with an approach different from other studies (McDonald, 2009; Johansson et al., 2004). To quantify the change in Δproxy/$\Delta ffCO_2$ emission ratios over time, a long term record for CO and $ffCO_2$ is analysed and compared to bottom-up inventory emission ratios.

Carbon monoxide. CO is generated in every carbon-fuel combustion process and is therefore a proxy candidate. The amount of CO produced generally depends on oxygen availability, i.e. if enough oxygen is readily available, fossil fuel combustion will produce very little CO. Typically, the $CO/ffCO_2$ emission ratio lies somewhere between 0.3 ppb/ppm and 35 ppb/ppm. Power plants ideally are at the lower end because they run at nearly perfect combustion efficiency by monitoring flue gases and increasing oxygen supply when CO concentrations exceed the acceptable threshold (Nicks Jr et al., 2003). $CO/(ff)CO_2$ ratios of residential heating systems depend on fuel-type and efficiency. According to McDonald (2009), fossil fuel systems (oil, gas) emit very little CO (<1 ppb/ppm), whereas bio fuel systems have high CO/CO_2 emission ratios (1 to 6 ppb/ppm).

Similarly, traffic emission ratios depend mostly on the engine type. As will be explained later in this section, gasoline-fuelled vehicles emit large amounts of CO, with $CO/ffCO_2$ emission ratios of up to 35 ppb/ppm (Tietge et al., 2020). Even larger CO emissions occur during cold-start conditions when the catalyst is not yet hot enough. Here, $CO/ffCO_2$ emission ratios can be 3 to 5 times higher, i.e. $CO/ffCO_2$ emission ratios of 100 ppb/ppm or more are possible (Dey et al., 2019). Diesel vehicles exhibit $CO/ffCO_2$ emission ratios from 1 ppb/ppm for heavy duty vehicles down to 0.3 ppb/ppm for passenger cars (Tietge et al., 2020).

Nitrogen oxides. NO_x is also produced during combustion, making it another proxy candidate. In the so-called Zeldovich mechanism (Zeldovich, 1946; Glarborg et al., 2018), where an O radical attacks the triple bond in N_2. The left-over N atom is rapidly oxidised to NO by reaction with OH or O_2. The Zeldovich mechanism is the main production pathway for NO_x and is promoted by high temperatures. Typically, the $NO_x/ffCO_2$ emission ratio is <1 ppb/ppm for industry and power plants according to the TNO inventory (Kuenen et al., 2022). Heating $NO_x/ffCO_2$ emission ratios usually fall between 0.1 and 1.3 ppb/ppm for oil, gas, and wood-pellet heating systems (McDonald, 2009). Burning green cuttings, e.g. from barley or corn, can lead to much higher NO_x emission ratios of ≈5 ppb/ppm (Dell'Antonia et al., 2012).

Diesel and gasoline engines. Traffic exhaust emissions, i.e. the emissions measurable with the set-up used here, are affected by fuel composition, engine type, combustion temperature, the after-treatment, and many more parameters of the combustion process (Wallington et al., 2006). Here, I will focus on passenger cars and explain (1) why gasoline engines emit significantly more CO than diesel engines and (2) why diesel engines emit significantly more NO_x than gasoline engines.

The most commonly known difference between diesel and gasoline engines is the ignition. While diesel engines rely on self-ignition of compressed fuel, gasoline engines ignite the fuel with a spark. However, the difference in the air-fuel mixing ratio between diesel and gasoline engines is more consequential for NO_x and CO emissions.

While most gasoline engines work with a stoichiometric air-fuel mixing ratio, i.e. just enough air to completely convert the fuel to CO_2 and H_2O, diesel engines work with a lean air-fuel mix ratio, i.e. more air than needed is present during combustion. As a consequence, the exhaust gas of a diesel engine contains more O_2 than that of a gasoline engine. A surplus of O_2 in diesel exhaust gas means that the reduction of NO_x to N_2 is more difficult to catalyse, leading to elevated exhaust NO_x emissions[3]. At the same time, CO is easily oxidised to CO_2, leading to low exhaust CO emissions. For gasoline engines, it is the other way around: low O_2 levels in the exhaust gas mean more NO_x is reduced in catalytic reactions, leading to lower NO_x exhaust emissions, while at the same time CO oxidisation is more difficult, leading to higher CO exhaust emissions (Wallington et al., 2006).

Offset and background. Trace gas enhancements, also known as offsets, are calculated from in-situ concentrations by subtracting an appropriate background. How exactly the background is chosen, depends on what emissions are of interest. For example, a background for continental Europe can be determined from measurements from the station Mace Head on the west coast of Ireland which measures the maritime background. If emissions on a sub-regional, local scale are of interest, the single-station and two-station approach (Section 2.8) are effective and efficient ways to determine background and offset.

---

[3] This is despite the fact that diesel engines usually run at lower combustion temperatures than gasoline engines, which speaks to the fact that combustion temperature is not the only determining factor for exhaust NO_x emissions.

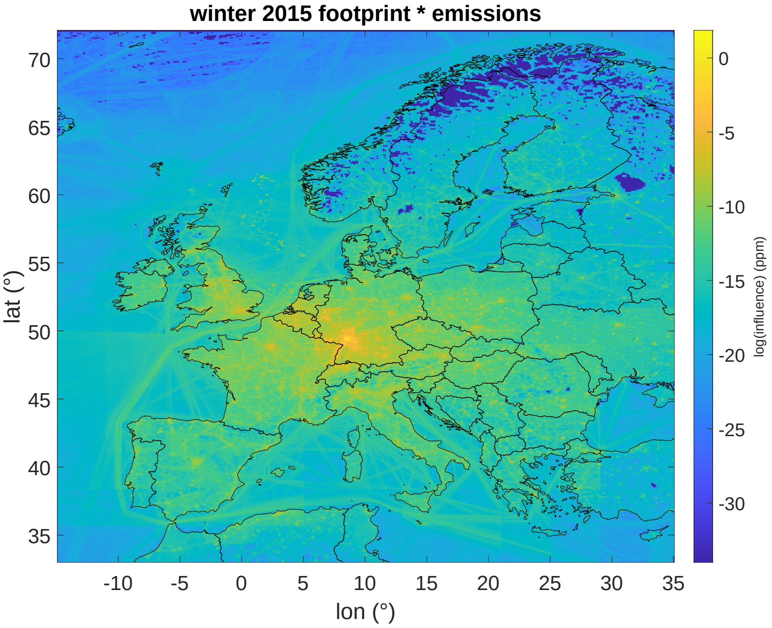

Fig. 2.1 TNO emissions folded with STILT footprints for winter 2015 (December 2014, January and February 2015). The color scale is logarithmic.

2.2 Modelling trace gas enhancements

Trace gas enhancements at the Heidelberg Institute for Environmental Physics can be calculated using surface flux maps folded with surface influence maps. Surface influence maps, also referred to as ‘footprints’, are the result of atmospheric transport modelling and show how emissions have to be weighted. Folding inventory emission maps with footprints weights each inventory cell surface flux appropriately and summation over the weighted emission for every cell yields the concentration enhancement in Heidelberg. A map of emissions folded with footprints is shown in Fig. 2.1.

Footprints are acquired through the Carbon Portal (2022) and based on the Stochastic Time-Inverted Lagrangian Transport model (STILT), see Lin et al. (2003). STILT transports a particle ensemble backwards in time to calculate footprints. Conceptually, Lagrangian transport models differ from their counterparts, Eulerian transport models, in what is observed. Eulerian models essentially calculate in-flow and out-flow of grid cells, whereas Lagrangian models transport particles on a sub-grid scale, achieved by interpolating meteorological data. ‘Time-inverted’ means that particles are transported backwards in time. That is, if Heidelberg is the point of interest, particles start there and are transported to where they came from originally by inverting the time axis. The STILT is stochastic in the sense that turbulent flow is 'simulated by a Markov chain process based statistically on observed meteorological parameters.' (Lin et al., 2003).

STILT can be run in conjunction with different meteorological prediction models. The implementation on the Carbon Portal (2022) uses the model of the European Center for Medium-Range Weather Forecasts (ECMWF). For instance, Maier et al. (2021) used the Weather and Research Forecasting (WRF) model to increase the spatial resolution of meteorological data fed into STILT. This modus operandi is commonly referred to as WRF-STILT (Nehrkorn et al., 2010).

The representation of the planetary boundary layer height is essential for near-surface observations (Lin et al., 2003). Without the correct planetary boundary layer height, emissions are incorrectly diluted. Closely connect to this problem is the question of emission height. The footprints I use, strictly use the surface source influence ansatz, i.e. everything is emitted at the surface. Maier et al. (2021) show how the emission height of sources influence modelled CO_2 concentrations in Heidelberg by comparing the surface source influence ansatz (SSI) with the volume source influence ansatz (VSI), where emissions happen at the correct height. Running 20 years of STILT with the VSI ansatz was beyond the scope of this thesis. Instead, I use a constant factor of 3.4 (Fig. C.6) to reduce the emissions of point sources with large stack heights around Heidelberg (closer than 50 km) that was determined by Maier et al. (2021) in their study of the years 2018 to 2020.

2.3 Emission inventories

Maps of emission data, categorised according to gas species, emission sector, and possibly fuel type, are called emission inventories. Most emission inventories are based on reports like the National Inventory Reports (NIR) and Informative Inventory Reports (IIR), which are handed to the UNFCCC (2022) every year by each contributing country. Reported emissions can be disaggregated (e.g. brought down to a sub-national scale) using proxies like local energy consumption data or statistical data and a consistent set of emission factors, e.g. Hestia (Gurney et al., 2012) or the Emissions Database for Global Atmospheric Research (EDGAR, 2022).

The TNO inventory (Denier van der Gon et al., 2013; Kuenen et al., 2014; Denier Van Der Gon et al., 2017; Kuenen et al., 2022) and its temporal profiles (Guevara et al., 2020) are used in conjunction with STILT to create a 15 year record of the $\Delta CO/\Delta ffCO_2$ ratio at the Heidelberg Institute for Environmental Physics to compare this to the measured emission ratio. Emission ratios from TNO will also be used as a frame of reference for the campaigns of heating and traffic emissions.

To model concentration enhancements in Heidelberg, footprints from the STILT tool on Carbon Portal are combined with TNO inventory emission maps. Unfortunately, the grids of the footprints and the emission maps do not match. I used the Climate Data Operators (CDO, Climate Data Operators, 2022; Schulzweida, 2021) provided by the Max Planck Institute for Meteorology (MPI-MET) to adjust TNO maps to the STILT grid. In doing so, point source emissions are assigned to the whole grid-cell (the information of the precise locations for point sources provided by TNO is lost).

Traffic. How are traffic emission factors (EF) determined? As previously explained, EFs are not constant but depend on environmental circumstances, combustion efficiency, vehicle, and engine type. Measuring EFs is not straight forward, especially when engines are manipulated to fit pollution norms when driving in a testing facility. Small, stable instruments (so-called Portable Emissions Measurement Systems, or PEMS) allow for on-board testing with real driving emission (RDE) levels, improving the accuracy of EFs. A range of vehicles from each vehicle group is tested to prevent biasing the EFs[4]. For Germany and a number of other countries, EFs are available in the form of the Handbook Emission Factors for Road Transport (Keller et al., 2017), which 'provides emission factors, i.e. the specific emission in g/km for all current vehicle categories (PC, LDV, HDV, buses, and motor cycles), each divided into different categories, for a wide variety of traffic situations.' (HBEFA, 2022)

With the EFs from the HBEFA, the Institute for Energy and Environmental Research (Ifeu, 2022) in Heidelberg runs a Transport Emission Model (Tietge et al., 2020) that 'maps motorised traffic in Germany with regard to its traffic and mileage, energy consumption and the associated climate gas and air pollutant emissions [...]' (TREMOD, 2022)[5]. Emissions calculated by TREMOD are part of the yearly NIR (NIR, 2022) and the IIR (Informative Inventory Report, 2022) data reported by the German Environmental Agency (Umweltbundesamt, 2022). 92 % of traffic CO_2 emissions are caused by cars (diesel 32 %, gasoline 29 %, others 1 %) and heavy duty trucks (30 %), while the rest is comprised of motor cycles (1 %) and light duty trucks (7 %) (NIR, 2022). Road transport emissions are split into fuel types and road types based on data from EMISIA[6]. for spatial disaggregation

---

[4] How many vehicles are tested varies from group to group. According to Stefan Hausberger (personal communication September 30, 2021), diesel passenger cars have the largest test pool of about 80 vehicles.

[5] TREMOD data were provided by Wolfram Knörr of ifeu via personal communication (May 17, 2021.

[6] EMISIA is a spin-off company of the Aristotle University Thessaloniki (AUTh) in Greece that developed COPERT, a software similar to TREMOD supported by the European Environment Agency and the Joint Research Centre (Emisia, 2022).

TNO, uses their own proxies based on OpenStreetMaps and OpenTransportMaps[7]. TNO traffic data are based on the reference year 2017 and extrapolated for recent years. Consequently, emissions may be sightly misestimated.

Heating. Like traffic emissions, heating emissions, too, are primarily tied to fuel consumption statistics. The fuel types are gas, oil, coal, and biomass (e.g. wood pellets). For residential heating in Germany, gas (46 %) and oil (31 %) are the most prevalent fuel types, while biomass burning (22 %) is less prominent, and coal is negligible (NIR, 2022). The TNO emission inventory uses LandScan (2022) based population density maps as a proxy to distribute emissions from gaseous and liquid fuels. Solid, non-biomass fuel emissions are distributed using the rural population density (<250 inhabitants per km^2), while biomass emissions are distributed by population density and in proximity to forested (mostly rural) areas.[8]

2.4 Averaging emission ratios

There are many ways to average emission ratios. For brevity, I will use the CO emission ratio as an example. Of course, this paragraph applies to NO$_x$, too. Imagine two data points with $P_1 = [\Delta\mathrm{CO} = 10\,\mathrm{ppb}, \Delta\mathrm{ffCO_2} = 1\,\mathrm{ppm}]$ and $P_2 = [\Delta\mathrm{CO} = 50\,\mathrm{ppb}, \Delta\mathrm{ffCO_2} = 10\,\mathrm{ppm}]$. To calculate the average emission ratio $\Delta\mathrm{CO}/\Delta\mathrm{ffCO_2}$, one could calculate the means of the components first (i.e. $\langle\Delta\mathrm{CO}\rangle/\langle\Delta\mathrm{ffCO_2}\rangle$) or one could calculate n individual ratios and then calculate their average (i.e. $\langle\Delta\mathrm{CO}/\Delta\mathrm{ffCO_2}\rangle$). The difference lies in the weighting. Calculating the mean according to $\langle\Delta\mathrm{CO}/\Delta\mathrm{ffCO_2}\rangle$ conceptually means giving each individual emission ratio the same weight. In our example $R_1 = \Delta\mathrm{CO}(P_1)/\Delta\mathrm{ffCO_2}(P_1) = 10\,\mathrm{ppb/ppm}$ and $R_2 = \Delta\mathrm{CO}(P_2)/\Delta\mathrm{ffCO_2}(P_2) = 5\,\mathrm{ppb/ppm}$. The mean emission ratio then is $\langle R\rangle = 7.5\,\mathrm{ppb/ppm}$. Using $\langle R\rangle = \langle\Delta\mathrm{CO}\rangle/\langle\Delta\mathrm{ffCO_2}\rangle = 60/11 \approx 5.5\,\mathrm{ppb/ppm}$. Here, emission ratios are weighted according to their contribution. This is akin to what is measured, since $\Delta\mathrm{ffCO_2}$ is derived from (bi)weekly integrated samples. However, measurements contain errors that have to be accounted for. Weighting measurements with the inverse square of their errors approximating the maximum likelihood, is common practise to obtain weighted means. Maier et al. (2021) have shown that this method introduces a bias for emission ratios, because of the uncertainty of $\Delta\mathrm{ffCO_2}$.

For Heidelberg measurements, Maier et al. (2021) plotted $\Delta\mathrm{CO}/\Delta\mathrm{ffCO_2}$ against $\Delta\mathrm{ffCO_2}$, and found the ratios rapidly increase for low values of $\Delta\mathrm{ffCO_2}$, giving

---

[7] Personal communication Stijn Dellaert, April 21, 2021.

[8] Personal communication Stijn Dellaert, January 31, 2022.

the impression of a $1/x$ curve. With synthetic data[9] it can be shown that this originates from the measurement uncertainty of $\Delta^{14}CO_2$, which is fixed at ≈2 ‰ and translates to an uncertainty of 1.0 ppm to 1.2 ppm $\Delta ffCO_2$. Measurements with $\Delta ffCO_2 < 5$ ppm therefore have uncertainties of 20 % to 100 %, while the uncertainty in CO is low (<10 %). This means, that for small $\Delta ffCO_2$, the denominator of the ratio varies enormously, while the numerator does not, leading to the observed $1/x$-behaviour.

An alternative calculation method for mean emission ratios is orthogonal regression, also known as weighted total least squares regression. Graphically, this means plotting ΔCO against $\Delta ffCO_2$ and fitting a regression line through the available data points, minimising the orthogonal distance of the points to the regression. Maier et al. (2021) have shown that such an orthogonal weighted least squares regression yields unbiased results with the same synthetic data that showed the bias due to the uncertainty in $\Delta^{14}CO_2$.

An algorithm for such a regression is described by Krystek and Anton (2007). Here, the two-dimensional problem is reduced to a one-dimensional problem by a shift from the equation $y = ax + b$ to $0 = y \cos\alpha - x \sin\alpha - p$, where α is the angle between abscissa and regression line and p is the orthogonal distance to the origin. An initial value for α is guessed (unweighted linear regression) from which p is then calculated (weighted mean of y multiplied by $\cos\alpha$ minus weighted mean of x multiplied by $\sin\alpha$). Finally only α is optimised and p recalculated with the new α. For physical reasons, the distance from the origin (p or b) should be zero: if no $ffCO_2$ is emitted, no CO is emitted. Wurm (2022) provides a version of the weighted total least square regression that allows forcing the regression through the origin.

2.5 Gaussian plume model

Atmospheric dispersion models describe how emission plumes behave or in other words how emitted particles disperse. The Gaussian plume model (GPM) is one widely used standard variant, where the emission distribution is assumed to be shaped like a Gaussian bell curve, both in vertical and in horizontal direction (Turner, 1970). Conventionally, the coordinate system is oriented such that the x-axis points in the direction of the plume, y is the horizontal direction and z is the vertical direction (Fig. 2.2). The most important parameters of this model are the horizontal and vertical standard deviation of the plume concentration

---

[9] Generate a data-set of ΔCO and $\Delta ffCO_2$ with a fixed emission ratio, add or subtract values in the uncertainty range from and to both components, calculate the resulting ratio, and compare this to the original ratio.

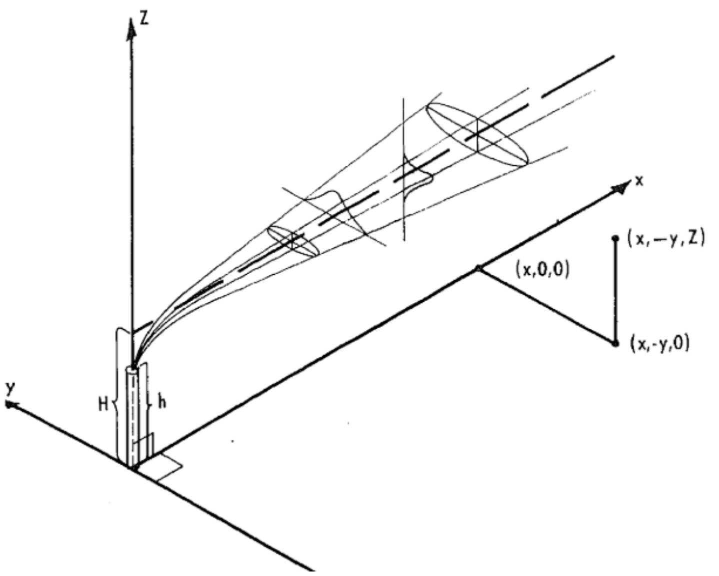

Fig. 2.2 Sketch of the Gaussian plume model, taken from Turner (1970) Fig. 3-1.

distribution, σ_y and σ_z, respectively. σ_y and σ_z depend on the meteorological factors wind speed, solar radiation and (during the night) cloud cover. Pasquill (1961) postulated six stability classes (A–F), see Table 2.1. For each class, the calculation of σ_y and σ_z is different. The comprehensive formula for the Gaussian plume model is given by Turner (1970). For my estimations for the traffic campaign, I calculate concentrations along the center line of the plume at ground level and assume no effective plume rise, which reduces the equation to

$$c(x) = \frac{1}{\sigma_{\mathrm{y}}(x)\,\sigma_{\mathrm{z}}(x)} \frac{Q}{\pi\,u} \tag{2.7}$$

where $c(x)$ is the concentration (in $\mathrm{g/m^3}$) in downwind distance x (in km) from the source, Q is the source emission flux (in g/s), σ_y and σ_z are the horizontal and vertical standard deviation of the plume concentration distribution (in m), respectively, and u is the wind speed (in m/s) at 10 m above ground. I calculate σ_y and σ_z according to the EPA's handbook for the ISC3 model (model guide, 2022):

$$\sigma_y(x) = 465.11628\,x\tan(\theta(x))\,, \tag{2.8}$$

with

$$\theta(x) = 0.017453293\big(c'd'\ln x\big), \tag{2.9}$$

and

$$\sigma_z(x) = a'x^{b'}. \tag{2.10}$$

The parameters a', b', c', and d' depend on the stability class and can be found on pages 1-16 and 1-17 in the EPA handbook for ISC3 (model guide, 2022).

Table 2.1
Pasquill–Gifford stability classes, taken from Turner (1970) Table 3-1.

Surface wind speed at 10 m (m/s)	Day			Night	
	Incoming solar radiation Strong	Moderate	Slight	Thinly overcast or ≥ 4/8 low cloud	Thinly overcast or ≤ 3/8 cloud
< 2	A	A–B	B		
2-3	A–B	B	C	E	F
3-5	B	B–C	C	D	E
5-6	C	C–D	D	D	D
> 6	C	D	D	D	D

2.6 Wind direction statistics

Calculating a mean wind direction requires viewing wind as a vector. Calculations in this section are adapted from Farrugia et al. (2009); Farrugia and Micallef (2017).

Consider a coordinate system such that the positive x direction is north and the positive y direction is east. Then, the angle with the x axis is the same as the wind direction. From the measured wind speed w_i and wind direction ϕ_i (in degrees) at time i, we calculate

$$\overline{v}_x = -\frac{1}{n}\sum_{i=1}^{n} w_i \cos\left(\phi_i\right), \tag{2.11}$$

$$\overline{v}_y = -\frac{1}{n}\sum_{i=1}^{n} w_i \sin\left(\phi_i\right), \tag{2.12}$$

where $\overline{v}_x$ is the mean component of the vector in x direction and $\overline{v}_y$ is the mean component of the vector in y direction. Note that the minus sign is necessary due to a difference in conventions: the vectors point in direction of the wind, but in meteorology, wind is defined by the direction it is coming from, i.e. wind from the west at 27° corresponds to a vector pointing east. The mean wind speed reads

$$\overline{w} = \sqrt{\overline{v}_x^2 + \overline{v}_y^2}, \tag{2.13}$$

and the mean wind direction is given by

$$\overline{\phi} = \arctan\left(\frac{\overline{v}_y}{\overline{v}_x}\right). \tag{2.14}$$

As quality check during the traffic campaign the fluctuations of the wind direction have to be quantified. The vector weighted standard deviation s according to

Eq. (25) of Farrugia and Micallef (2017) is

$$s^2 = \frac{1}{n\,\overline{w}} \sum_{i=1}^{n} \Big(w_i \, \Delta\big(\phi_i, \overline{\phi}\big) \Big) \,, \tag{2.15}$$

where $\Delta\big(\phi_i, \overline{\phi}\big)$ is the minimum angular distance, calculated according to Eq. (13) of Farrugia et al. (2009) as

$$\Delta\big(\phi_i, \overline{\phi}\big) = \arctan \Big(\tan \big(0.5\, \phi_i - \overline{\phi} \big) \Big)^2 \,. \tag{2.16}$$

2.7 Sampling strategies for sector-dominated measurements

Considerable efforts were undertaken to overcome the problem of spatial separation. Two mobile laboratories were designed, built, and maintained over the course of two years to allow measurements (1) in the middle of residential areas and (2) at a major highway. Each mobile laboratory requires a 220 V power supply, limiting the choice of location to a 50 m radius from a power outlet. For the traffic campaign, spatial separation was excellent and no temporal separation was required. For the residential heating sector, spatial separation from traffic is impossible. Thus, temporal separation of the traffic sector and the heating sector is key. The temporal separation of traffic and heating emissions requires knowledge about their diurnal time profile. Fig. 2.3 shows the normalised diurnal pattern of the heating load (Heitkoetter et al., 2020, cf. Figs. 14 and 15) and traffic emissions (TNO inventory time profile). The normalisation is such that any point below the line $y = 1$ shows below average load and any point above shows above average load. Traffic peaks during commuting rush-hours (7:00 h to 9:00 h in the morning and 16:00 h to 18:00 h in the evening) and reaches 5 % of average hourly emissions during the night (1:00 h to 5:00 h).

Demand for space heating and hot water during workdays starts one hour earlier in the morning than traffic, peaking just as workers begin to commute. Over the day, the demand for space heating remains constant until it drops to half the daytime demand from 22:00 h to 4:00 h. Consequently, the sampling strategy for the heating emission campaigns was to collect samples during the night, when traffic emissions are virtually absent in residential areas (the remaining fraction of traffic emissions are mostly trucks on the highway) and heating systems operate at base load conditions.

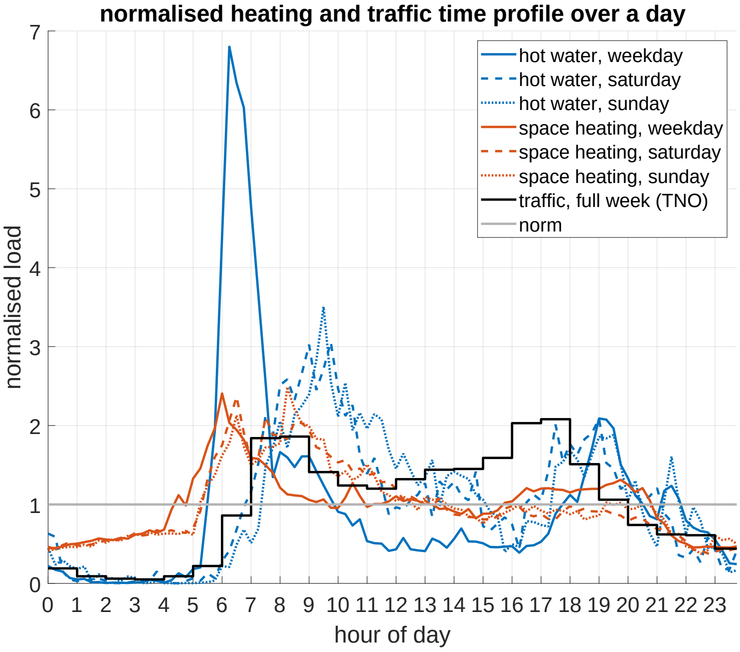

Fig. 2.3 Diurnal time profile of normalised traffic, domestic hot water, and space heating loads based on TNO time profile for traffic and supplementary material of Heitkoetter et al. (2020) for space heating and domestic hot water. Note that for the heating data from Heitkoetter et al. (2020), load refers to area specific heat demand (without declaring how the demand is met i.e. by which heating system), while the TNO traffic load refers to emissions directly.

2.8 Mobile laboratories

Each mobile laboratory (ML) is equipped with instruments for CO_2, CO, and NO_x measurements and for flask sampling. Flask samples are 3 l air containers that are necessary for $\Delta^{14}CO_2$ analyses. The main mobile laboratory, ML1, is additionally equipped with a weather station for measurements of wind speed, wind direction, and temperature and a Rn-monitor (Levin et al., 2002). That is, ML1 is equipped to monitor atmospheric transport. A picture of the exterior of ML1 is shown in Fig. 2.4. Both MLs are equipped with a 10 m mast which mounts the inlet lines for the instruments, and in the case of ML1 the weather station. Air conditioning units were mounted on the draw-bar and the inner front wall to keep the instruments at a stable temperature, stabilising the measurements.[10] Depending on the conditional requirements of the measurement campaign, either just one or both of MLs were used.

---

[10] All construction jobs in and around the MLs were done by the staff of the Institute's workshop. Please refer to the acknowledgements, where their contributions are honoured accordingly.

Fig. 2.4 Main mobile laboratory (ML1) with fully extended mast.

Table 2.2
Intake lines attached to the 10 m mast of both Mobile Laboratories.

Line material	Outer ⌀	Instrument ML1	Instrument ML2	Comment
Dekabon	1/4"	Flask sampler, (and Picarro/AEROLASER)	FTIR	Main air intake, flexible
Teflon	1/4"	ICAD	ICAD	NO_x instruments require reaction-inert material
Dekabon	1/2"	Rn-Monitor	Flask sampler	Rn-monitor requires larger inner diameter for aerosols

Exterior modifications. The mobile laboratories were built into two box trailers with inside measures of 3060×1750×1900 mm (L × W × H). Exterior modifications were the same for both MLs, while the interior setups are different, based on the instrument used. Descriptions of the basic working principles of the instruments can be found in Appendix A. Air inlets for the instruments have to be at a certain height above ground to capture emissions from sources in the vicinity. To this end, a 10 m mast was installed, equipped with three detachable intake lines (Table 2.2). A meteorological station can be placed on top of the mast. For all measurements described in this thesis, the station was atop ML1. For temperature stability as required by the instruments, a split air conditioner system was installed.

Main mobile laboratory. The main mobile laboratory, also denoted mobile laboratory 1 (ML1) in the following, contains a Cavity Ring-Down Spectrometer (CDRS, Picarro model G2301)[11], a fluorescence CO analyser (AEROLASER model L5001) and a flask sampler accompanied by a drying unit (both provided by ICOS Flask and Calibration Laboratory in Jena). Figure 2.5 shows the gas flow setup of the instruments. Gas from mast is pumped through the drying unit by either the flask sampler (during sampling) or the external pump (only online when no sampling takes place). Five solenoid valves (V1 to V5), controlled by the CRDS instrument, are used to switch between air (V2) and calibrated gas cylinders. Three of the gas cylinders are for calibration (W1, C1, C2), while the other (T1) is for quality control. The gas tubing behind the valve array splits and goes to the CO analyser and the CRDS instrument (CO_2 and CH_4, the following called Picarro). The CO analyser (in the following called AEROLASER) requires two supply gases (N_2 at a purity of at least 99.999 % and a mix of 99.75 % Ar (6.0) and 0.25 % CO_2) and an independent calibration standard (WA). During the internal calibration of the AEROLASER, gas from the cylinder (pressure around 1000 mbar) displaces gas from the sample intake. However, the valve does not close the intake line causing back-flushing: The pressure in the sample line is lower. Consequently, calibration gas not only enters the AEROLASER, but also the tubing connected to the valve array and the CRDS instrument. Sampling of flasks, calibration of the AEROLASER, and measurements of the calibration cylinders attached to the solenoid valves all have to be timed meticulously to avoid interference by the back-flushing of AEROLASER calibration gas.

During the traffic campaign, the ML1 setup had to be adapted due to failure of AEROLASER L5001 and Picarro G2301. The failure was caused by failure of the air conditioning unit and by a power outage. Thanks to our colleague Olivier Laurant of LSCE, the campaign could continue nonetheless, because he provided a Picarro G2401, capable of measuring CO_2, CO, and CH_4. The setup depicted in Fig. 2.5 only changes downstream of the drying unit, flask sampler, and external pump. The solenoid valves were replaced by a multi-port valve directly controlled by the Picarro G2401. The tank N_2, $ArCO_2$ and CA were no longer in use. This new setup was also used during the second heating campaign in 2021.

Background mobile laboratory. The background mobile laboratory, also denoted Mobile Laboratory 2 (ML2) in the following, contains a Fourier-transform infrared spectrometer (FTIR) and an institute-built flask sampler (see Rieß (2019) and Kneuer (2020) for details), each on a separate line with their individual air drying systems ($Mg(ClO_4)_2$ for the flask sampler and a combination of $Mg(ClO_4)_2$ and counter-flow drying for the FTIR). The FTIR spectrometer is capable of measuring

---

[11] I will refer to CDRS instruments as 'Picarro' throughout this thesis.

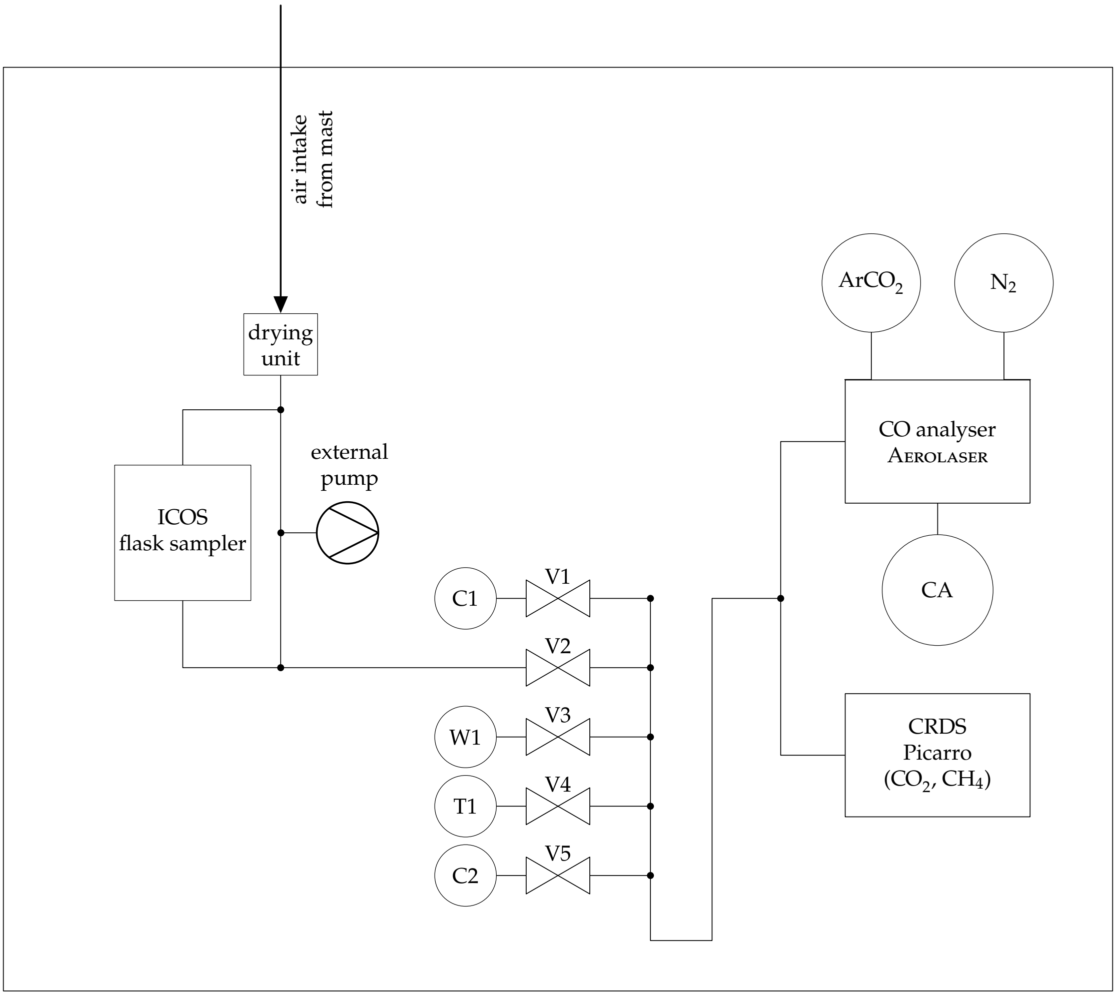

Fig. 2.5 Gas flow diagram for Mobile Laboratory 1. V1 to V5 are solenoid valves controlled by the Picarro instrument. Calibrated gas cylinders are C1 (low calibration), W1, T1, C2, and WA. C1, W1, and C2 are calibration cylinders for external calibration listed from low to high trace gas concentrations. T1 is a target cylinder, i.e. a reference gas not used in calibration to check the quality of the data. CA is the calibration cylinder for the AEROLASER required for the internal calibration. $ArCO_2$ and N_2 are supply gases for the AEROLASER.

CO_2, CO, CH_4, N_2O, and H_2O simultaneously at a time resolution of 3 minutes. Similar to ML1, the spectrometer is calibrated with three gas cylinders and quality-checked by a target cylinder. For drying and case-flushing, N_2 has to be supplied at all times, too. Instrument specifications are given by Hammer et al. (2013).

Single-station approach. For diffuse area sources, e.g. heating in residential areas, a single-station approach is applicable. Measurements from a single station are used in conjunction with prior knowledge of emission patterns of the source, as discussed above. Using ^{222}Rn as a tracer for atmospheric conditions, well-mixed situa-

Table 2.3
Tanks in Mobile Laboratory 1. Uncertainties assigned by ICOS FCL in Jena were <0.01 ppm for CO_2. For CO, uncertainties assigned by FCL were <0.005 ppb for UHEI30 and UHEI34, 0.07 ppb for UHEI32, and 0.25 ppb for UHEI36. CH_4 uncertainties were ≤0.05 ppb. PIC4_3 was measured in the IUP laboratory with a CRDS instrument (Picarro).

Tank	Function, label	CO_2 (ppm)	CO (ppb)	CH_4 (ppb)	Value assignment
UHEI30	C1	400.31	95.89	2008.41	FCL Jena
UHEI32	W1	553.18	560.82	2403.75	FCL Jena
UHEI34	T1	499.61	369.20	2206.73	FCL Jena
UHEI36	C2	714.47	976.67	2815.85	FCL Jena
PIC4_3	CA	490.12	450.85	2203.02	Own measurements

tions are sampled as a background, while during an inversion, when trace gas concentrations build up, 'signal' samples are collected. There are two ways to identify the background when using the single station approach. First, taking one sample each noon during well-mixed conditions, one can determine a background for the next 24 h. Conceptually, this means it is assumed that every day, fresh air with trace gas concentrations at background level is mixed into the planetary boundary layer at noon. When an inversion develops during the afternoon and the night, emissions from local sources accumulate in the planetary boundary layer. Hence, concentration enhancements during the night with respect to the noon background originate from local sources and their emission ratios can be identified. I call this the day-by-day ansatz for background determination. However, Peter (2020) found that noon flasks do not necessarily reflect the true (free troposphere) background, but contain residual anthropogenic emissions that pollute the background sample, leading to skewed proxy emission ratios. In practise this means that I aim to find one 'global' background, in the sense that it preferably applies to the whole campaign or at least multiple flasks. This global background is still based on noon flasks, but the concentrations may now be the average of said flasks, so conceptually, the day-by-day linking of noon concentrations to nightly concentration increases is avoided.

Two-station approach and same air-mass approach. For spatially isolated sources, the two-station approach is applicable. Its applicability was first demonstrated by Rieß (2019) in the 'Research Infrastructures: Needs, Gaps and Overlaps' Project (RINGO, 2022). In this thesis, the two-station approach is realised by positioning two mobile laboratories such that the source of interest is the only, or at least the dominant, emitter between the two stations. Usually, sampling takes place when an air parcel moves directly from one station to the other, loading up on emissions from the source of interest on the way. Then, the concentrations at the station first passed by the air parcel are the background for the other station.

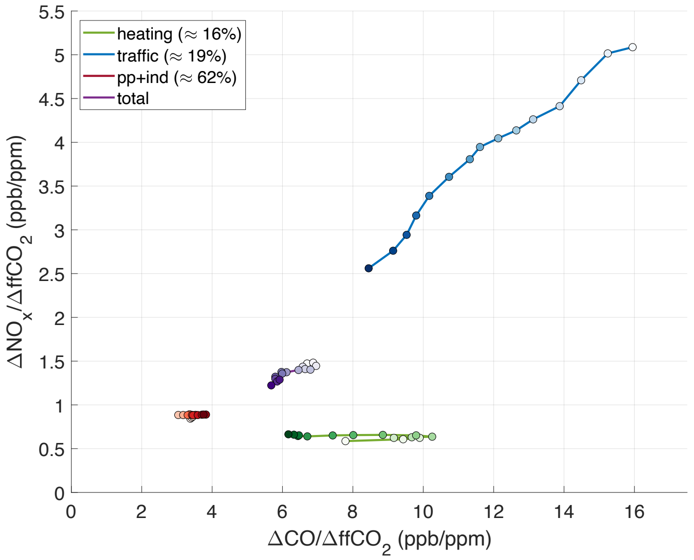

Fig. 2.6 Double ratio plot of TNO emission ratios for Germany from winter 2005/2006 until winter 2019/2020. Darker tones indicate later years. For each sector, the average $ffCO_2$ contribution is given in the legend. The numbers do not add up to 100 % because not all but only the largest sectors are shown. Public power and industry (pp+ind) were combined in an effort to display emissions from all point sources together.

Another way to use this setup is the *same air-mass approach*. The *same air-mass approach* assumes well-mixed conditions, i.e. homogeneous trace gas concentrations perpendicular to the wind direction. This assumption is justified if the air-mass was previously influenced only by homogeneous surface sources or sinks or if sufficient horizontal mixing occurred after the air-mass passed heterogeneous source or sink areas. The question of sufficient horizontal mixing depends not only on the heterogeneity of the source, but also on the horizontal distance between the upwind and downwind stations, and a close distance is advantageous. (Rosendahl et al., 2021) The *same air-mass approach* requires a much higher effort, since it is necessary to verify the (approximate) homogeneity of the air-mass. However, once this is sufficiently shown, the *same air-mass approach* greatly increases the number of possible sampling situations.

2.9 Double ratio plots

For all campaigns the results will presented in so-called double ratio plots. Double ratio plots show the $\Delta CO/\Delta ffCO_2$ ratio on the x-axis and the $\Delta NO_x/\Delta ffCO_2$ ratio on the y-axis. In other words, with a double ratio plot we can assess both proxy ratios simultaneously. Assessing both proxies for all samples at the same time enables better separation of sources. For instance, with only CO as a proxy, it is sometimes difficult to distinguish traffic from residential heating in residential areas, since both can show $\Delta\mathrm{CO}/\Delta\mathrm{ffCO}_2$ ratios in the range of 4 ppb/ppm to 10 ppb/ppm as the measurement campaigns will show. Diesel light duty vehicles and heavy duty vehicles have roughly the same $\Delta\mathrm{CO}/\Delta\mathrm{ffCO}_2$ emission ratio, but passenger cars emit markedly more $\mathrm{NO_x}$. Hence, traffic and residential heating can be differentiated on the $\mathrm{NO_x}$ scale.

Fig. 2.6 shows a double ratio plot for winter (December, January, February) TNO emission ratios for years 2005 to 2020. Progression of time is indicated by colors from light to dark, i.e. 2005 is the lightest tone and 2020 the darkest. CO emissions from residential heating increased until winter 2010/2011, decreasing afterwards and stagnating close to 6 ppb/ppm. The traffic sector shows the largest progress, both in $\mathrm{NO_x}$ and CO emissions. The decrease in total emission ratios (all sectors combined) is much smaller than that of traffic and heating sector, because power plants and industry are the largest emitters (≈62 % of ffCO_2 emissions), and the total emission ratios are dominated by these two sectors, when all German emissions are considered.

Chapter 3

Traffic campaign

I conducted a measurement campaign at the A5 highway, north-west of Heidelberg from October 2020 until February 2021 using both mobile laboratories. With the background mobile laboratory (ML2) to the west of the highway and the main mobile laboratory (ML1) to the east of it, the goal was to measure the traffic-dominated proxy/ffCO_2 emission ratios. I find that emission ratios strongly depend on fleet composition. In general, NO_x emissions by heavy duty vehicles are overestimated, whereas CO emissions by light duty vehicles are underestimated by the TNO inventory.

Parts of this chapter – most of Section 3.1 and parts of Section 3.2 – are taken (sometimes verbatim) from Deliverable 2.8 of the VERIFY Project[12]. Section 3.2.2 was crafted after the submission of Deliverable 2.8.

3.1 Campaign setup and site description

To study traffic emissions from a highway, the two-station approach (cf. Section 2.8) using both mobile laboratories was applied. The experimental setup was located in the Rhine Valley to the north-west of Heidelberg and targeted highway A5 that connects Frankfurt and Karlsruhe. The highway speed limit at this location is 120 km/h, and there were no construction sites nearby. The campaign lasted from October 2020 until February 2021. Typical vehicle densities during daytime are between 50 and 100 vehicles per minute (both directions combined). Figure 3.1 shows the location in three levels of detail. The mobile laboratories were in west-east alignment, approximately 800 m apart.

The downwind station (ML1) was installed about 20 m from the centre of the highway. The height difference between the highway and the intake of the downwind station was about 8.5 m. To the west, shrubs lower than the extended

---

[12] I authored Deliverable 2.8 in collaboration with Samuel Hammer. Please refer to the online documentation (Rosendahl et al., 2021). All Deliverable contributions written by Carlos Alberti and Frank Hase (Karlsruhe Institute of Technology; remote sensing approach) are not in this thesis.

Table 3.1
Instruments used in ML1 for the traffic campaign. Reproducibility is based on quality control (target) cylinder measurements: offset ± standard deviation to the calibrated values are given. Entry for ICAD and weather station based on precision described in instrument manual.

Use period	Instrument	Function	Reproducibility	Temporal resolution
Oct 13 to Nov 11, 2020	Picarro G2301	CO_2, CH_4 recordings	CO_2: -0.02 ± 0.13 ppm	1 s, averaged to minutes
Oct 13 to Nov 11, 2020	Aerolaser L5001	CO recordings	CO: -15.07 ± 6.18 ppb	1 s, averaged to minutes
Dec 03, 2020 to end	Picarro G2401	CO_2, CO, and CH_4 recordings	CO_2: -0.03 ± 0.05 ppm CH_4: 0.45 ± 0.10 ppb CO: -2.50 ± 1.92 ppb	1 s, averaged to minutes
Whole campaign	ICAD05	NO_2 and NO_x recordings	NO_x: 0.15 ppb or 2 % NO_2: 0.15 ppb or 2 %	60 s
Whole campaign	Flask sampler	collects 1 h-accumulated air samples	–	–
Whole campaign	Heidelberg Radon Monitor	^{214}Po recording, ^{222}Rn estimation	–	30 min
Whole campaign	Thies weather station	wind speed, wind direction	speed: ±0.3 m/s direction: ±2°	1 s, averaged to minutes

10 m mast separated ML1 from the highway. To the north, tall conifers slightly hindered the air flow from that direction.The selection of sampling locations had to consider that both laboratories require a wired power supply. The instruments used in mobile laboratories 1 (ML1) and 2 (ML2) are listed in Tables 3.1 and 3.2, respectively, each with their corresponding reproducibility. Instrument failure in ML1 forced a change of instruments in November 2020. The campaign was without continuous measurements of CO_2, CO and CH_4 in ML1 until December 3, 2020. Tables 3.1 and 3.2 are inadequate to fully validate the data to the required accuracy. An in-depth discussion of the quality check, bias and uncertainty estimation for the traffic campaign is given in Appendix B. The traffic campaign requires higher levels of accuracy for the in-situ data than the other campaigns because the in-situ data are used to calculate emission ratios in the later parts of Section 3.2 (whereas normally, the precise flask sample measurements by the ICOS Flask and Calibration Laboratory in Jena are used).

We installed the upwind station on the western boundary of a pig farm. The farmhouse is located downwind of the upwind station (see Fig. 3.1 c) for winds from the northwestern sector (250° to 345°). The area enclosed by the two stations comprises the highway, the farmhouse, and agricultural fields. In this

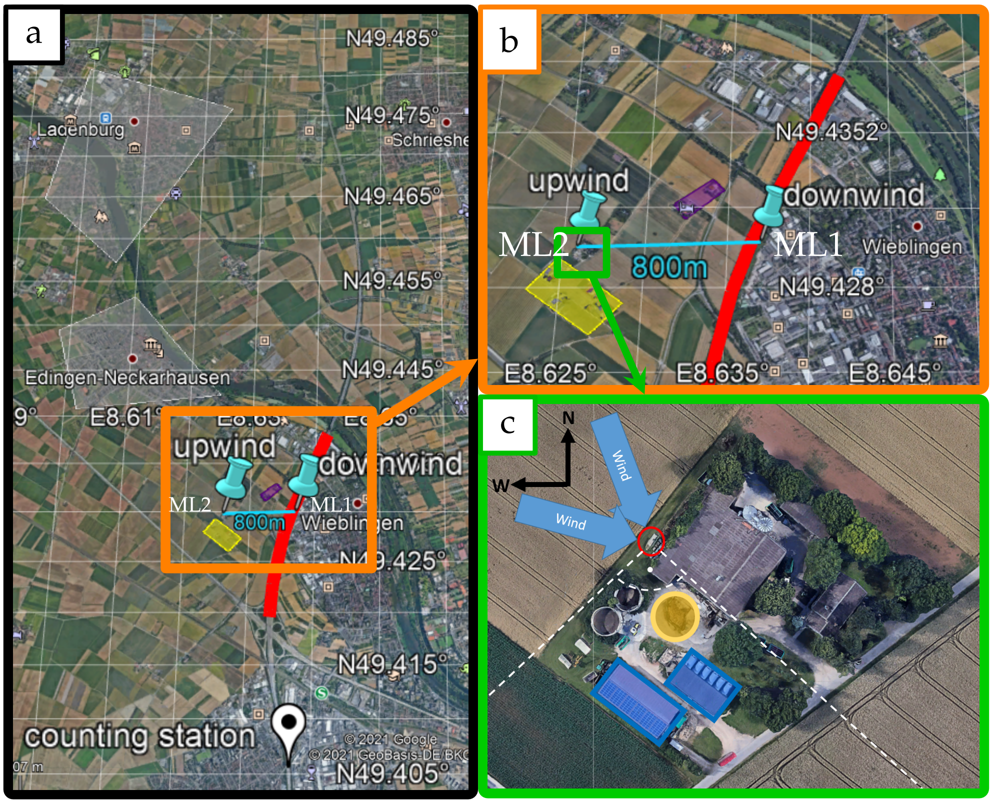

Fig. 3.1 Traffic campaign set up. (a) Overview. Mobile laboratories are cyan pins. Highway marked red, traffic counting station Eppelheim is the white pin at the bottom. Grey polygons are close-by towns that are relevant for the same air-mass approach (Edingen-Neckarhausen, Ladenburg). (b) Sampling region. Mobile laboratories are in West-East alignment, 800 m apart, shown here as a cyan line. The yellow rectangle indicates farms near ML2, the upwind station. The purple rectangle indicates two farms 350 m to the north-west of ML1, the downwind station. (c) Detailed view of the upwind station. ML2 is circled red, the South quadrant (135° to 225°) is indicated by white dashed lines. Blue rectangles mark animal housings, and the open slurry storage is the yellow circle. Large arrows indicate main wind directions (west, north-west).

experimental setting, the highway is the dominant fossil fuel source contributing to the concentration enhancements between the two stations. To estimate the fossil fuel CO_2 influence of the farmhouse on the downwind station, a Gaussian plume model (Turner, 1970) was applied as described in Section 2.5. The ffCO_2 emissions of the farmhouse are assumed to correspond to the averaged heating emissions per house in the Heidelberg area, calculated based on the TNO emission inventory. We assume that the total residential heating emissions occur during the three winter months and are constant in time. These assumptions result in a mean winter ffCO_2 emission of 1.2 g/s for the farmhouse. Using the Gaussian plume model, the calculated farmhouse influence on downwind station (ML1) is smaller than 0.02 ppm CO_2 for all Pasquill–Gifford atmospheric stability classes (Pasquill,

Table 3.2
Instruments used in ML2 for the traffic campaign. Reproducibility is based on quality control cylinder measurements. Multiple targets were measured at the FTIR and gave no consistent results. The displayed reproducibilities give the range of offsets. An in-depth discussion of the quality checks of the traffic campaign is given in Appendix B. Entry for ICAD and weather station based on precision described in instrument manual.

Use period	Instrument	Function	Reproducibility	Temporal resolution
Whole campaign	FTIR	CO_2, CH_4, CO recordings	CO_2: ±0.2 ppm CH_4: ±0.5 ppb CO:±2 ppb	3 min
Whole campaign	ICAD04	NO_2 and NO_x recordings	NO_x: 0.15 ppb or 2 % NO_2: 0.15 ppb or 2 %	20 s, averaged to minutes
Whole campaign	Heidelberg Flask Sampler	collects 1 h-accumulated air samples	–	–

1961) applied in Turner (1970). The farmhouse influence on the downwind station (ML1) is thus smaller than the measurement precision and much smaller than the observed CO_2 enhancements. In order to increase the number of suitable wind conditions for up- and downwind sampling, we applied the *same air-mass approach* (Section 2.8).

Figures 3.1b and 3.1c show the upwind station's location (ML2) in detail. The farm, including the animal housings and the slurry storage, excludes the southern wind sector from the *same air-mass approach*. Significant CH_4 emissions, partly accompanied by NO_x emissions from the slurry storage and animal housing (Bava et al., 2017), are observed from this southern wind sector. There are no buildings directly to the north or west of both stations. The closest buildings to the downwind station are two farms in 350 m distance in north-western director, marked purple in Fig. 3.1b. Both farms do not have livestock. We estimated the influence of the farmhouses $ffCO_2$ emissions by using same residential heating emission flux as before for the Gaussian plume model and obtained a $ffCO_2$ contribution of smaller than 0.1 ppm for the downwind station (ML1) during daytime. This is less than 2 % of the average observed total CO_2 difference between the laboratories and less than the detection limit.

In the larger catchment area (Fig. 3.1a), two medium-sized towns (Edingen-Neckarhausen: 14 000 inhabitants, Ladenburg: 11 500 inhabitants) are located to the north west of the setup (at approx. 315° and 330°, and distances of 2.5 km and 4.5 km, respectively). TNO emission data suggest comparable $ffCO_2$, CO, and NO_x emissions for the two towns. In the Gaussian plume model, the

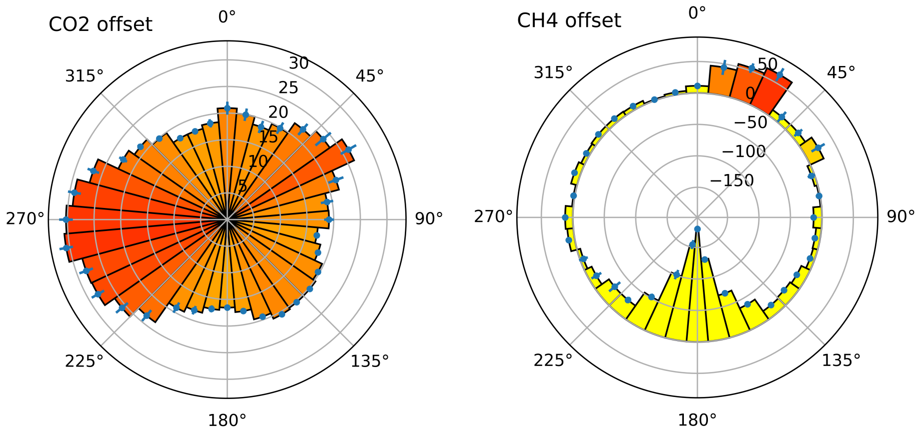

(a) CO_2 offset at ML2.

(b) CH_4 offset between ML1 and ML2.

Fig. 3.2 Windrose plots of average measured concentrations enhancements for **(a)** CO_2 offset at ML2 (relative to 3-day minimum at ML2) and **(b)** CH_4 offset between ML1 and ML2 (concentration at ML1 minus concentration at ML2). Concentration enhancements are plotted on the radial axes, wind direction on the angular axis. Colors only emphasise values. If the towns north-west of the setup had significant influence on our measurements, a corresponding large offset would be visible to the north-west in **(a)**. In **(b)**, negative values indicate higher CH_4 concentrations at ML2 – mostly from the south, where the pig sties, slurry storage, and other farm houses are located. The positive offset to the north-north-east can be attributed to either the recycling facility Recyclinghof Wieblingen or the chemical plants Kluthe GmbH.

horizontal dispersion coefficient σ_y at a distance of 2 km is between 150 m and 500 m depending on the atmospheric conditions. At a distance of 5 km, σ_y increases to between 300 m and 800 m. Thus, plumes of point sources in a distance of 2 km cannot be treated as well-mixed across the horizontal distance of both stations. However, in neither of the two towns, significant point sources are present. Therefore, we regard the towns as expanded anthropogenic area sources. The spatial west-east extend of both towns (parallel to the line between ML2 and ML1) is 1.2 km and 2 km, respectively, exceeding the laboratories' distance. The upwind in-situ observations were examined for enhanced concentration during situations when the emission plumes of the cities turn over the station.

Neither for CO_2, CO, or NO_x a significant concentration enhancement, larger than the typical temporal variability were found. CO_2 is shown as an example in Fig. 3.2a. Plotting the CH_4 difference between ML1 and ML2 in a similar way in Fig. 3.2b, we find that ML2 shows large CH_4 enhancements from the south and ML1 shows large CH_4 enhancements from the north north-east (25°). Because we do not know what else this source may emit (CO, CO_2 and NO_x emissions would be indistinguishable from traffic emissions), air from that direction is not suitable for traffic-dominated emission ratio measurements. Based on these results, we conclude that the *same air-mass approach* is applicable to the western and northwestern catchments. Urban influence can affect the downwind station (ML1) for easterly wind directions and highway emissions would be too diluted at ML2. Hence, easterly winds are excluded. We chose wind directions such that to the south west (<250°) of ML2, the closest neighbour houses are excluded (yellow rectangle in Fig. 3.1). For northerly winds, we excluded situations where air would pass over the industrial area (at >345°).

For the *same air-mass approach*, the condition of air-mass homogeneity is only fulfilled if the broad (laterally extended) air parcel travels along the main wind direction without strong disturbance from lateral air currents (i.e. air currents that are not parallel to the main wind direction). For the direct two station approach, the assumptions require the air to travel more or less directly from the upwind station to the downwind station. Therefore, I introduce a 20° wind direction spread[13] threshold. The value of 20° originates from a closer look at the second flask pair (October 16, 19:30 h). The spread of the wind direction over the hour is 24°. While the wind direction is relatively stable for the most time, for 11 min the wind direction changed from roughly 330° to somewhere between 0° and 80° (19:56 h to 20:07 h). In other words, for roughly 1/6 of the sampling, the wind came from an undesirable direction. I chose the wind direction criterion such that this kind of situation would be excluded, i.e. the threshold is 20° of variation. All valid flask pairs fall way below this value. Only two virtual flasks (explanation of the term in Section 3.2.2) fall above 10° of variation and were examined more closely, finding that both have reasonable wind conditions.

In addition to these spatial (wind direction related) sample selection criteria, a valid sample must fulfil additional quality criteria. The difference between the in-situ measurement of the mobile laboratories and the offline flask measurement in the ICOS Flask and Calibration Laboratory (FCL) must not exceed 1 ppm and 10 ppb for CO_2 and CO, respectively. If the two measurement methods diverge beyond these thresholds, this indicates that the flask air sample may not correspond to the hourly averaged ambient air concentrations. Since ΔNO_x can only be determined from hourly averaged ambient air concentrations, it is important that in-situ measurements and flask measurements agree.

The applied sample selection criteria can be summarised as follows:

(1) Hourly mean wind direction between 250° and 345°

(2) Hourly wind direction variation less than 20°

(3) absolute difference between in-situ and flask measurements in CO_2 <1 ppm

---

[13] Calculation of this spread can be found in Section 2.6.

(4) absolute difference between in-situ and flask measurements in CO <10 ppb

Consult Section 2.6 for the calculations of mean wind direction and wind direction variation.

3.2 Results

This section has two parts. First, I discuss the flask samples taken during the campaign according to the criteria laid out above. Second, I will discuss a broader approach, in which I identified and analysed episodes with suitable wind conditions and estimated emission ratios for those episodes from continuous measurements (by assuming a large fraction of ΔCO_2 is of fossil origin). The episodes were split into time frames of 45 to 90 min to make them comparable to the flask samples. Since the episodes are like flask samplings but without $ffCO_2$ (or rather $^{14}CO_2$) measurements, I will refer to them as 'virtual flasks' from this point on. Virtual flasks will be discussed in section 3.2.2.

3.2.1 Flask samples

Initially, 33 flask pairs were collected. For six pairs, no $\Delta^{14}CO_2$ measurements were possible due to mislabelling (flasks were emptied completely by FCL in Jena, because they were not marked for $\Delta^{14}CO_2$ measurements in the flask sampling program). Another 15 pairs were discarded because they violated the wind selection criteria (wind direction outside the range of 250° to 345° or variation larger than 20°). Of the remaining 12 pairs, two pairs had a ΔCO_2 >1 ppm between flask and average atmospheric concentration and another pair had no discernible $\Delta ffCO_2$ (<0.1 ppm). A very low $\Delta ffCO_2$ value results in very large ratios with relative errors of >1000 ‰. Such results do not further our understanding of the issue at hand and I discarded the corresponding flask.

Of the remaining nine pairs, two pairs (numbered #2, #6, according to the row of the result table (not shown), where odd rows are background flasks and even rows are signal flasks) were not taken simultaneously, but with a 30 min offset (background samples taken too early) due to an operational error. Asynchronous flask sampling is mainly a problem of $\Delta^{14}CO_2$. All other components necessary for ratio calculation can be taken from continuous in-situ data synchronously to the downwind sample time-frame. If all trace gas concentrations are stable over the 1.5 hours of sampling (30 min early start at upwind station plus one full hour of sampling at the downwind station), I assume this is the case for $\Delta^{14}CO_2$ as well.

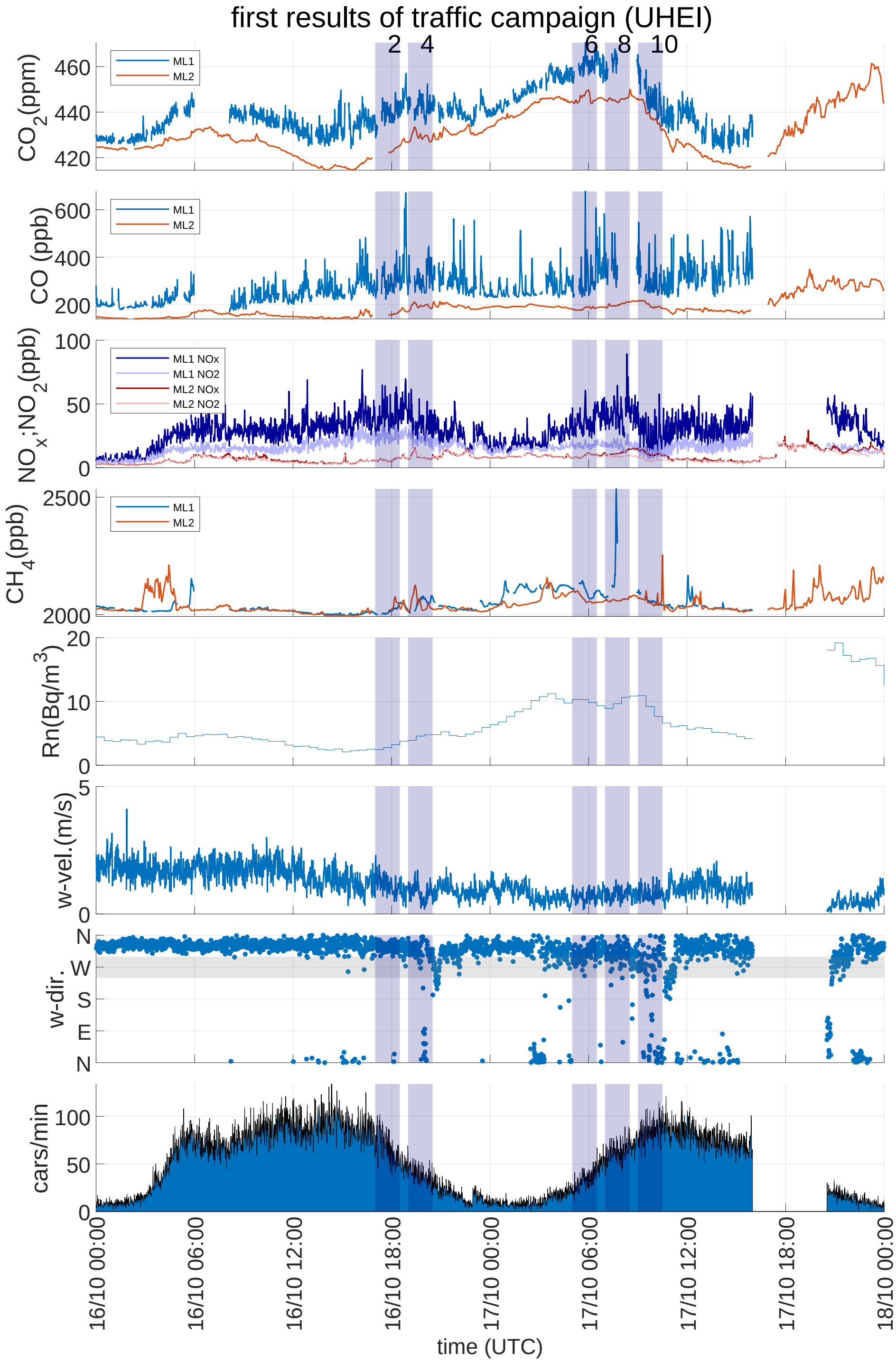

Fig. 3.3 In-situ data for the first two days of the (active) traffic campaign with the first five flask pairs shown as vertical blue bars.

Fig. 3.3 shows the data for the two days surrounding the first five flask samples. The first four panels give the in-situ CO_2, CO, NO_x, NO_2, and CH_4 concentrations of the downwind station (ML1, blue) and the upwind station (ML2, red). The ^{222}Rn activity concentration, wind speed and wind direction – all measured at the downwind station – are given in panels 5 to 7, and the traffic load for the Eppelheim counting station[14] is plotted in the bottom panel. Vertical blue shading indicates flask sampling times.

Are flask pairs #2 and #6 suitable for evaluation, despite the asynchronicity? Flask pair #2 cannot be used, since the in-situ data do not cover the full 1.5 hours which can be seen in Fig. 3.3 as the line-break of the red line during the sampling marked '2' (first blue-shaded bar). Flask pair #6 spikes in CO_2 in the overlap period and is near-constant in the half-hour before and the half-hour after. Hence, the spike does not affect the mean CO_2 significantly (difference <1 ppm). Comparing $\Delta^{14}CO_2$ for pair #6 (-20.3 ± 1.5 ‰) and pair #8 (-22.0 ± 1.5 ‰) shows that the plateau in CO_2 (03:00 h until 07:30 h) had an almost constant $\Delta^{14}CO_2$ value, i.e. the measured $\Delta^{14}CO_2$ value of pair #6 is very close (within uncertainties) to the value we would have measured half an hour later. For further calculations I use the measured $\Delta^{14}CO_2$ value of pair #6 in combination with in-situ data at the time of downwind sampling.

Remaining is a total of eight flask pairs. This scarcity of valid flask pairs led to the concept of virtual flasks (Section 3.2.2) and subsequently to a deeper insight into the issue.

Figure 3.4 shows a full day of the in-situ traffic campaign measurement from January 22, 2021 as an example. It has the same structure as Fig. 3.3. I chose this day to illustrate how wind direction affects trace gas concentrations. A different way to show this data is Fig. 3.5, where the in-situ CO_2, CO, and NO_x concentration enhancements (downwind minus upwind) for the example day of January 22, 2021, are displayed.

We find a good correlation between the CO_2, CO and NO_x enhancements and the traffic volume for wind directions fulfilling the *same air-mass approach* requirements in Fig. 3.5. Consider, for instance, the period after the second flask pair was sampled (labelled #34). When the wind direction changes from north to east, the CO_2 enhancement drops to zero. As the wind turns back north, the CO_2 concentration enhancement returns. The ^{222}Rn concentration also strongly indicates that the measured enhancements are from a source in the immediate

---

[14] Note that between the sampling site and the Eppelheim counting station there is a highway intersection where vehicles can get on and off the highway (Fig. 3.1). Consequently, the counts at the station in Eppelheim do not represent the exact amount of traffic that is sampled, but give a realistic estimate of traffic activity.

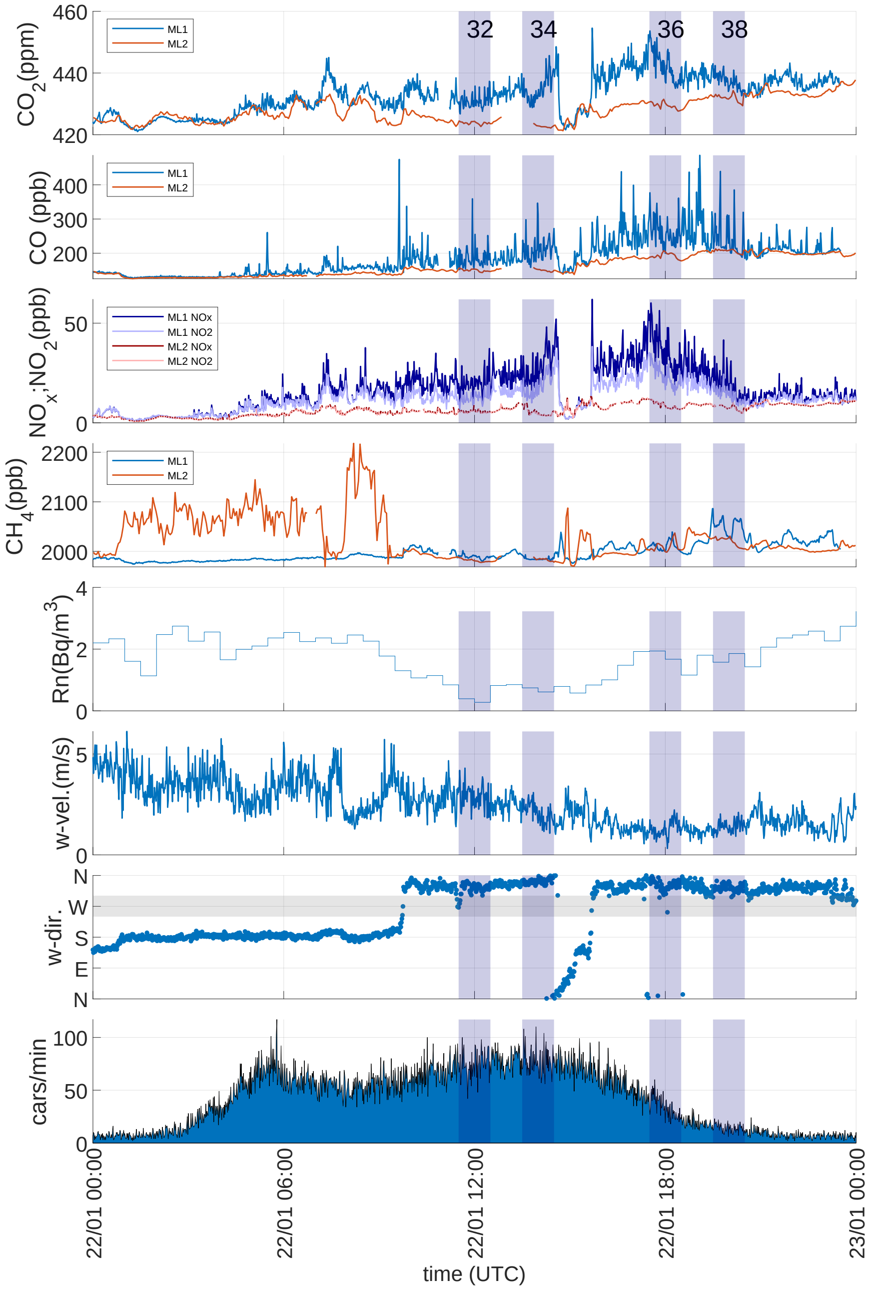

Fig. 3.4 Continuous data from upwind (red) and downwind (blue) station on January 22, 2021. Traffic counts according to sampling station Eppelheim. Shaded blue bars are flask sampling times.

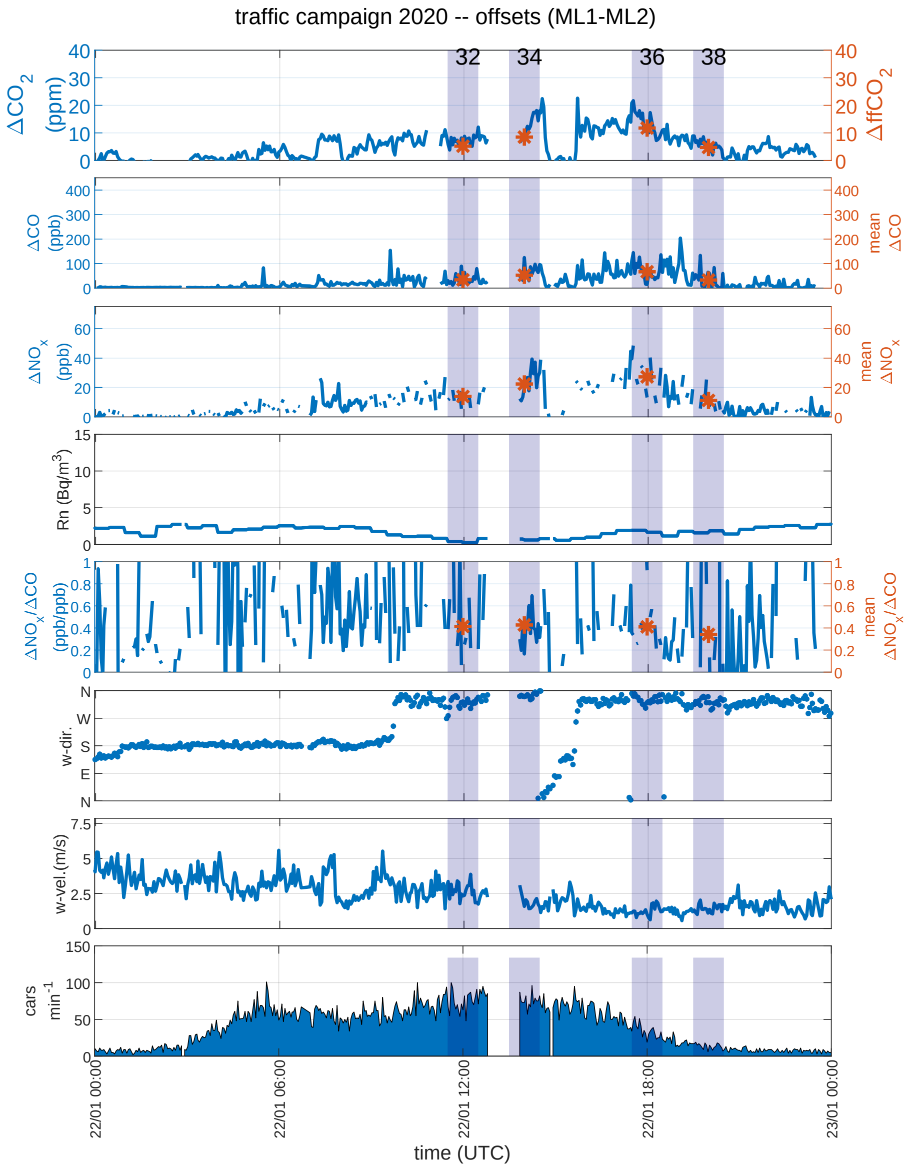

Fig. 3.5 CO_2, CO, and NO_x concentration enhancements between down- and upwind station on January 22, 2021. The auxiliary parameters (^{222}Rn and wind) are measured at the downwind station. Traffic counts according to sampling station Eppelheim. Vertical blue shaded areas indicate flask sampling times. The ^{14}C-based ffCO$_2$ enhancement during the flask sampling periods is shown as red stars with respect to the right y-axis in the CO_2 panel. CO enhancements plotted as red stars are based on the flask samples and correspond to the right axis, too. The same holds for hourly mean NO_x concentrations in the NO_x panel.

vicinity, because the usual inversion-based correlation between ^{222}Rn concentrations and concentration enhancements of other trace gases is absent. Such high concentration enhancements without an inversion require a strong close-by source. That is, the data confirm that the highway must be the dominant source of the concentration enhancements (since no other strong sources are nearby).

The ^{14}C-based ΔffCO_2 concentrations make up the major share ($\approx$ 90 %) of the CO_2 enhancement. To see this graphically, compare the blue line (CO_2 enhancement) with the red stars (ΔffCO_2) in the top panel of Fig. 3.5. Due to the addition of bio-fuels to diesel and petrol, we expect a non-fossil CO_2 contribution from traffic emissions. Measurements by Friedrich and Hammer (2017) show that the average bio-fuel admixture for diesel and petrol in the Rhine Valley region was 5 % in 2017. TREMOD suggests a bio-fuel contribution of of 5.2 % for all of German highways (Tietge et al., 2020). The average bioCO_2 fraction in the valid flasks was 10 ± 20 % (the error is the standard deviation). The >10 % measured bioCO_2 fraction and the large standard deviation indicate that some non-fossil CO_2 (other than from bio fuels) is emitted between ML2 and ML1. The prime suspect is soil respiration, which is low, but non-zero in winter (Dörr and Münnich, 1987). Therefore, I do not use a bioCO_2 fraction of 5 % that is expected from traffic, but rather a bioCO_2 fraction of 10 ± 20 % for the ffCO_2 estimation for the virtual flasks, carrying over the large uncertainty into the uncertainties of the ratios.

3.2.2 Virtual flasks

With the information from the valid flask samples, a solid understanding of our sampling setup, and the *same air-mass approach*, we hypothesise that for west to north-west wind (wind direction 250° to 345°) ΔffCO_2 can be approximated by $\Delta\text{ff}CO_2 \approx 0.9\,\Delta CO_2$. Consequently, $\Delta\text{proxy}/\Delta\text{ff}CO_2$ ratios can be calculated for these episodes, which I call *virtual flasks*. Since no comparison between in-situ and flask measurements is possible, virtual flasks must only fulfil the following conditions:

- average wind direction 250° to 345°
- stable wind (deviation <20°)

This selection yields 112 virtual flasks, spread over all hours of the day, a variety of traffic compositions and atmospheric conditions, representing many different situations. The results are shown in Fig. 3.6. Please refer to Appendix B for an in-depth analysis of quality checks, bias corrections, and uncertainty estimates. Everything described in Appendix B is applied to the results shown in Fig. 3.6.

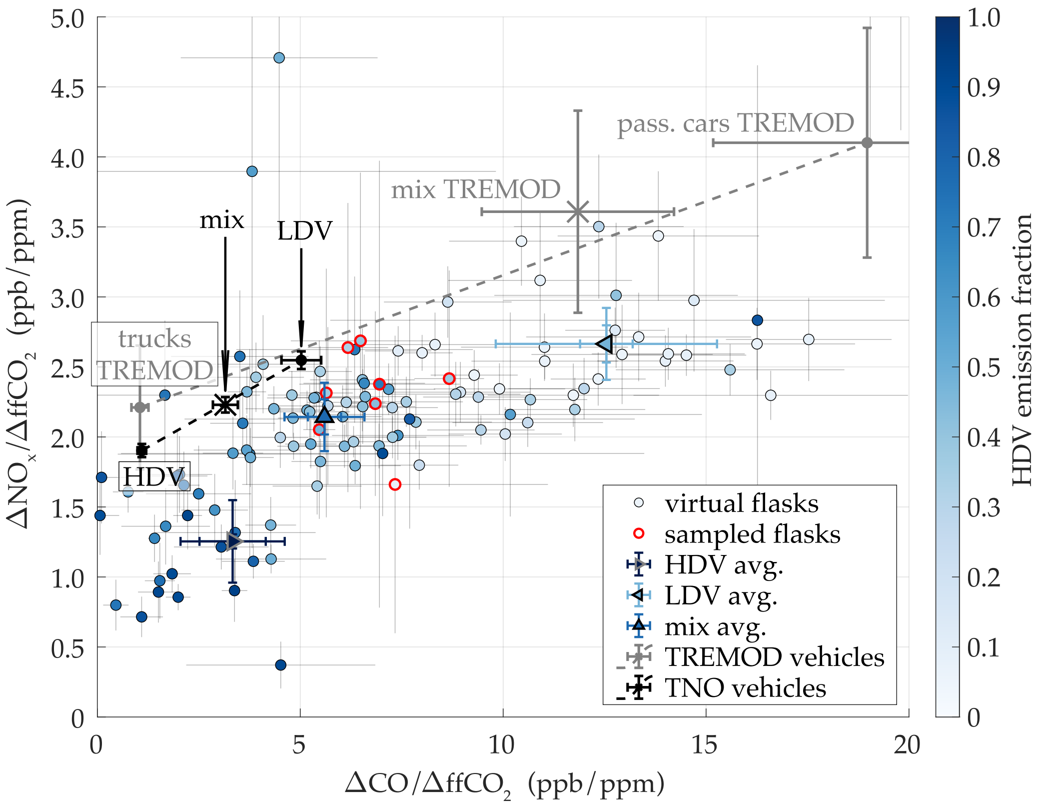

Fig. 3.6 Proxy ratios of traffic campaign flasks plotted against each other. Points in shades of blue represent virtual flasks: the darker the color, the higher the fraction of trucks on the highway. Flask samples are indicated by a red border. Black dots show TNO emission ratios for three traffic vehicle categories: light duty vehicles (LDV), heavy duty vehicles (HDV), and mix (LDV & HDV). Similarly, TREMOD emission ratios for truck-only traffic (bottom left) and car-only traffic (top right) are shown in grey and connected by a dashed line of the same color.

In Fig. 3.6, every virtual flask is assigned a 'heavy duty vehicle (HDV) emission fraction'. The HDV emission fraction is the percentage of CO_2 emissions that is caused by HDV. I calculate the HDV emission fraction by using traffic density data provided by the Bundesanstalt für Straßenwesen (BASt) and emission factors (in units of g/km) provided by HBEFA (Section 2.3). The CO_2 emission factors for HDV are roughly four times higher than for LDV[15]. Weighting the HDV fraction f_{HDV} = #HDV/(#HDV + #LDV) (i.e. the percentage of vehicles that are HDV) with

---

[15] The grouping into LDV and HDV is done according to BASt (Vehicle Groups according to Bundesamt für Straßenwesen, 2022). Here, the German Pkw is equivalent to LDV and Lkw is equivalent to HDV. The difference to TREMOD is, that TREMOD has an own category for motor cycles and passenger cars with trailers are not considered HDVs. Since both motor cycles and cars with trailers are rather rare, the difference is small.

the emission factors yields the HDV emission fraction

$$f_{\mathrm{HDV}}^{\mathrm{emis}} = \frac{4\,\#\mathrm{HDV}}{4\,\#\mathrm{HDV} + \#\mathrm{LDV}}\ . \tag{3.1}$$

Black dots in Fig. 3.6 represent single-cell[16] highway TNO emission ratios for the different vehicle classes light duty vehicle (LDV), heavy duty vehicle (HDV), and both light and heavy duty (mix) and are labelled accordingly. The 'all roads mix' data point represents not only highway emissions but also emissions from all other road types in the area. Grey points represent emission ratios according to TREMOD for all of Germany. For clarification, passenger cars (TREMOD point at the top left) are a subgroup of LDV. LDV additionally include vans and small transporters, which only make up 10 % of the LDV traffic on highways. Similarly, trucks are a subgroup of HDV. HDV additionally include (travel) busses, which make up ≈ 3 % of the highway HDV traffic (according to TREMOD). The difference between HDV and trucks, as well as between LDV and passenger cars is graphically visible in the point 'mix TREMOD' where all vehicles are combined. The distance of this point from the dashed line is due to the influence of all other vehicle categories (if passenger cars and trucks truly where the only vehicles that emit gases on the highway, the mix TREMOD point would be exactly on the line between the points 'trucks TREMOD' and 'pass. cars TREMOD'). Uncertainties for TREMOD are estimated at 20 %, based on the educated guess of Stefan Hausberger (personal communication, October 14, 2021), whose group is responsible for the modelling of the emission factors for the vehicle fleets of Germany, Austria and Switzerland, i.e. providing the emission factors in HBEFA. For details on the emission factors, revisit Section 2.3.

While the category LDV is not strictly the same as passenger cars and the category HDV is not strictly the same as trucks, the corresponding TREMOD and TNO points in Fig. 3.6 should be in close proximity to each other. However, this is not the case. While the truck and HDV points are reasonably close together, the LDV and passenger cars points are not. TREMOD assigns much higher CO ratios to gasoline passenger cars than TNO (individual emission ratios of gasoline passenger cars for TNO and TREMOD not shown here), leading to an overall higher CO ratio for passenger cars.

In an effort to make the measured data comparable with the three points (LDV, mix, HDV) of TREMOD and TNO, I calculated three mean ratio points by orthogonal weighted total least squares regression, as described in Section 2.4.

---

[16] The emission ratios are calculated from emissions of the single 1 km × 1 km cell that contains the sampling site. Calculating the emission ratios for all German highways does not change the values significantly, meaning the traffic on this highway is very close to the average traffic on any German highway.

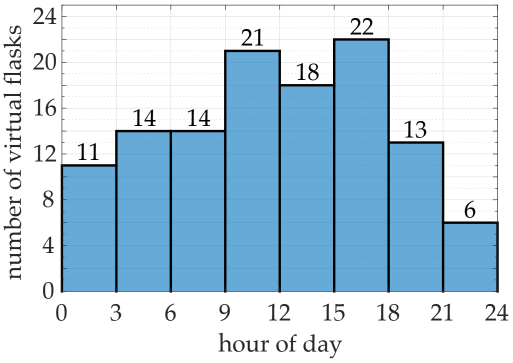

Fig. 3.7 Sample distribution over the hour of day for all virtual flasks. Day hours (between 06:00 h and 18:00 h) are over-represented, making up 63 % of all samples (75 of 119).

The calculated ratio points have two error bars, because the uncertainty of the slope of the orthogonal weighted total least squares regression visibly underestimates the real uncertainty. I want the error bars to represent the possible spread of ratios (in the chosen vehicle class category), so as the second error bar I use the standard deviation of the selected ratios. The dark blue right-pointing grey-bordered triangle shows the mean ratio of points that have a $f_{\mathrm{HDV}}^{\mathrm{emis}} > 80\,\%$. The light blue left-pointing triangle shows the mean ratio of points that have a $f_{\mathrm{HDV}}^{\mathrm{emis}} < 20\,\%$, i.e. 80 % or more LDV emission fraction. The upward pointing triangle accounts for points with $39.5\,\% \leq$ HDV emission fraction $\leq 48.5\,\%$, because the mix point for TNO is at $f_{\mathrm{HDV}}^{\mathrm{emis}} = 48.5\,\%$ and the TREMOD point is at $f_{\mathrm{HDV}}^{\mathrm{emis}} = 39.5\,\%$. Choosing the range of $f_{\mathrm{HDV}}^{\mathrm{emis}}$ to determine a measured mix ratio is challenging, since it is not clear what that mix is exactly. From the inventory perspective, it is clear: take all highway traffic emissions and divide CO by ffCO_2. Since the measurements do not capture all emissions and a mean over all virtual and sampled flasks would be biased towards daytime hours as Fig. 3.7 shows, this simple approach does not work for the measured emissions.

Choosing the range of $f_{\mathrm{HDV}}^{\mathrm{emis}}$ between 39.5 % and 48.5 % conceptually means that I consider every measurement within the range a reasonable example of the average traffic situation on the highway. One way to look at $f_{\mathrm{HDV}}^{\mathrm{emis}}$ is to imagine a point on each dashed line: $f_{\mathrm{HDV}}^{\mathrm{emis}}$ dictates where on the line the point is. A $f_{\mathrm{HDV}}^{\mathrm{emis}} = 0\,\%$ is equal to the LDV/pass. cars point for TNO and TREMOD, respectively. $f_{\mathrm{HDV}}^{\mathrm{emis}} = 100\,\%$ is equal to the HDV/trucks point for TNO and TREMOD, respectively. Spanning the range from 39.5 % and 48.5 % on the dashed lines then provides the range of expected ratios that must be compared to the mix mean point of the measurements.

3.3 Discussion

In order to interpret the dependence of the ratios on $f_{\mathrm{HDV}}^{\mathrm{emis}}$, note that the underlying BASt traffic density data originate from a counting station to the south. As shown in Fig. 3.1, there is a highway intersection between the counting station and the campaign site. Consequently, $f_{\mathrm{HDV}}^{\mathrm{emis}}$ shown in Fig. 3.6 has an unknown uncertainty attached to it. This is not a problem as long as $f_{\mathrm{HDV}}^{\mathrm{emis}}$ is used for qualitative analysis only (e.g. visualising the difference between truck-heavy traffic and car-heavy traffic). The only time the $f_{\mathrm{HDV}}^{\mathrm{emis}}$ is used in a certain quantitative way is for the selection of virtual flasks to calculate the average measured ratios for trucks, passenger cars, and the mix. Since here, $f_{\mathrm{HDV}}^{\mathrm{emis}}$ only dictates what points are considered for each mean and slightly changing the selection has little effect on the mean, I argue that using $f_{\mathrm{HDV}}^{\mathrm{emis}}$ in this way is reasonable. To support this, I compared daily traffic counts found on the BASt website (Automatic traffic counts by Bundesanstalt für Straßenwesen, 2022) for the counting station south of the intersection and a counting station north of our campaign site (I only have detailed data for the southern counting station). The data show a difference of 11 % in average daily HDV traffic between the northern (8980 counts per day) and the southern (7980 counts per day) counting station in 2020 and a difference in average daily LDV traffic of 3 % between the two stations. A 10 % change in truck count shifts $f_{\mathrm{HDV}}^{\mathrm{emis}}$ by roughly 2 %. Changing the threshold $f_{\mathrm{HDV}}^{\mathrm{emis}}$ for any of the ratios by 2 % does not change the results significantly, consequently the calculated means are well estimated, even if the real traffic differs from the counts of the southern counting station.

As $f_{\mathrm{HDV}}^{\mathrm{emis}}$ in Fig. 3.6 increases (darker colors), the emission ratios decrease, because gasoline cars emit more $\mathrm{CO}/\mathrm{ffCO_2}$ than trucks and diesel cars emit more $\mathrm{NO_x}/\mathrm{ffCO_2}$ than trucks. At a general level, this finding agrees with TNO inventory data (in black) and TREMOD results, which both show HDV (or, respectively, trucks) at low $\mathrm{CO}/\mathrm{ffCO_2}$ ratios and LDV (or, respectively, passenger cars) at high(er) $\mathrm{CO}/\mathrm{ffCO_2}$ and $\mathrm{NO_x}/\mathrm{ffCO_2}$ ratios. For a comparison of the subcategory ratios and the mix ratios, consult Table 3.3 in addition to Fig. 3.6. Both TNO and TREMOD generally overestimate $\mathrm{NO_x}/\mathrm{ffCO_2}$ ratios, even if we consider a potential 10 % bias in $\Delta\mathrm{NO_x}$ (Appendix B.3). In particular, trucks seem to emit far less $\mathrm{NO_x}$ than either TNO (46 %) or TREMOD (70 %) predict.

To improve comparability between measured emission ratios (where up to 20 % of emissions come from the other vehicle category) and TNO/TREMOD emission ratios (where 100 % of emissions are from the right vehicle category), I calculate 'inferred' emission ratios. To this end, I assume that any measured ratio is a linear combination of the 'true' truck and the 'true' car emission ratio, weighted with $f_{\mathrm{HDV}}^{\mathrm{emis}}$ and $(1 - f_{\mathrm{HDV}}^{\mathrm{emis}})$, respectively.

Table 3.3
Ratios from Fig. 3.6. Uncertainties for TREMOD are educated guesses from Stefan Hausberger (personal communication October 14, 2021), uncertainties for TNO provided by Super et al. (2020). Selection of (virtual) flasks for subcategories is described in the text. 'Ideal' values in parenthesis calculated according to Eq. (3.2) for LDV, Eq. (3.3) for HDV and Eq. (3.4) for the mix.

	mix		LDV, pass. cars		HDV, trucks	
Sources (ppb/ppm)	$\frac{\Delta CO}{\Delta ffCO_2}$	$\frac{\Delta NO_x}{\Delta ffCO_2}$	$\frac{\Delta CO}{\Delta ffCO_2}$	$\frac{\Delta NO_x}{\Delta ffCO_2}$	$\frac{\Delta CO}{\Delta ffCO_2}$	$\frac{\Delta NO_x}{\Delta ffCO_2}$
TNO	3.16 ± 0.31	2.23 ± 0.06	5.03 ± 0.49	2.55 ± 0.06	1.10 ± 0.11	1.90 ± 0.05
TREMOD	11.84 ± 2.37	3.61 ± 0.72	18.97 ± 3.79	4.10 ± 0.82	0.31 ± 0.06	2.21 ± 0.44
Measured	5.62 ± 1.02	2.35 ± 0.28	12.50 ± 2.74	2.92 ± 0.14	2.98 ± 1.11	1.30 ± 0.32
Inferred	8.26 ± 1.77	2.20 ± 0.48	13.62 ± 3.07	3.10 ± 0.81	1.45 ± 1.01	1.04 ± 0.38

The mean $f_{\mathrm{HDV}}^{\mathrm{emis}}$ of the points that make up the passenger-car-mix mean is 9.18 %. For the truck-mix mean, the mean is $f_{\mathrm{HDV}}^{\mathrm{emis}} = 87.43\,\%$. The inferred mean ratios are calculated from

$$R_{\mathrm{cars}}^{\mathrm{measured}} = R_{\mathrm{cars}}^{\mathrm{inferred}} \cdot 90.82\,\% + R_{\mathrm{trucks}}^{\mathrm{inferred}} \cdot 9.18\,\% \tag{3.2}$$

$$R_{\mathrm{trucks}}^{\mathrm{measured}} = R_{\mathrm{cars}}^{\mathrm{inferred}} \cdot 12.57\,\% + R_{\mathrm{trucks}}^{\mathrm{inferred}} \cdot 87.43\,\% \tag{3.3}$$

where R can be either the CO emission ratio or the NO_x emission ratio. With the results from Eq. (3.2) and Eq. (3.3), the inferred mix ratio follows using the $f_{\mathrm{HDV}}^{\mathrm{emis}} = 44\,\%$ (center of the previously discussed mix range), i.e.

$$R_{\mathrm{mix}}^{\mathrm{inferred}} = R_{\mathrm{cars}}^{\mathrm{inferred}} \cdot 56\,\% + R_{\mathrm{trucks}}^{\mathrm{inferred}} \cdot 44\,\%. \tag{3.4}$$

The results are shown in the row 'inferred' in table 3.3. The uncertainties are the uncertainties of the measured ratios propagated with Gaussian error propagation. Graphically, these results would be a line through the measured mean truck point and the measured mean passenger car point. The 'true' car and truck ratios would slightly extend this line beyond the measured points. The 'true' mix point would lie close to the middle of the line (on the point that splits the line 44:56, i.e. skewed towards the inferred car ratio).

TNO underestimates the inferred CO emission ratio for LDV by a factor of 2.7, while ratios for HDV agree within error margins. TREMOD, on the other hand, overestimates the CO emission ratio for passenger cars by almost 40 % and underestimates truck CO emissions. The stark differences between measurements and inventories call for an investigation of this problem by inventory experts. For NO_x, the inventories consistently overestimate truck NO_x emissions. Note that TNO data are based on the year 2017, whereas TREMOD data are based on the year 2019. Every year, more and more old trucks are replaced by newer models, following the

EU regulations of the EURO-IV norm. Hence, we expect truck NO_x to decrease over the years. TNO compensates for the lack of recent data by extrapolating trends in vehicle fleet development. Still, I would expect TREMOD with its more recent data to fit the measured data better than TNO, but both overestimate truck NO_x emissions by a factor of ≈ 2. If a unusually large fraction of trucks on this highway are EURO-IV conform (compared to the average German highway), this could lead to smaller-than-expected NO_x emissions, but no data are available (or even exist) that could support this hypothesis. For the traffic mix and LDV, TNO estimates the NO_x emissions quite well, while TREMOD again overestimates both.

In terms of our measurements, it is striking that the calculated inferred mix CO emission ratio is much larger than the measured. The largest accumulation of points is not scattered around a line through the truck-mix mean and passenger-car-mix mean points in Fig. 3.6, but rather shifted to the top and/or left. While the assumptions for the inferred ratios oversimplify the real situation, it is unclear how any of the assumptions would lead to such a medium-sized overestimation of CO emissions or a medium-sized underestimation of NO_x emissions. I can only hypothesise that, similar to the mix point of TREMOD, the non-ideal measured mix point deviates from the inferred mix point due to influence of vehicles not captured by the truck mix point or the passenger car mix point. TREMOD data suggest that (travel) buses emit more CO and NO_x than trucks. Assuming buses only drive during the day, their emissions would not be captured in the truck mix point. However, it is rather unlikely that buses have such a large impact, since they only contribute 1 % of CO_2 emissions according to TREMOD. While I cannot offer a convincing explanation of the slight shift, I do not deem the shift significant for the general observation of the mismatch between inventories and measurements.

In conclusion, using the *same air-mass approach* and an estimation formula for the $\Delta ffCO_2$ ($\Delta ffCO_2 = 0.9\Delta CO_2$), the set of valid data points increased by 112. Because of this and the available traffic count data, I was able to show that the vehicle mix has a large impact on emission ratios. The average traffic TNO $NO_x/ffCO_2$ emission ratios agree reasonably well with the measurements, although NO_x emissions of trucks are likely overestimated. TNO CO emissions, especially of passenger cars and of the mix, are much lower than what we measured and disagree with TREMOD results, too. This has to be investigated by emission inventory experts.

3.4 Perspectives

For future highway campaigns, the ideal sampling site would have a traffic counting station nearby (without any exits or intersections between the sampling site and the counting station). A small distance of the downwind mobile laboratory to the highway (just as it was here) is desirable. If possible, the connection line between the laboratories should be parallel to the main wind direction.

City traffic may be a interesting source to investigate for the next traffic campaign. Ideally, the campaign would take place in summer to minimize the influence of heating emissions. In such a setting, it may even be possible (depending on the traffic density on the chosen road) to identify individual car emission ratios. To measure a mean urban traffic ratio, possibly, sampling air at a height of 30 m (such as at the Institute of Environmental Physics) with a stationary laboratory is more feasible. A short test run may already show how much we can or cannot learn with 10 m of sampling height next to a busy street during rush hour.

The workload associated with a traffic campaign could be significantly reduced by establishing the $ffCO_2$ fraction early and relying on virtual flasks for the rest of the campaign. In general, running two mobile laboratories at the same time is time consuming. Instruments should be as low-maintenance as possible.

Planning for the campaign should also include at least one side-by-side comparison, maybe even two (one before, one after). For side-by-side comparison, flask measurements are mandatory. One should also perform a line test (i.e. releasing gas at the inlet on top of the mast) to gauge the delay between the MLs.

Chapter 4

Heating campaigns

I conducted measurement campaigns in two residential areas not far from Heidelberg. In late March 2020, I conducted the first-ever campaign with the main mobile laboratory (ML1). The second residential heating campaign took place mid-March 2021 in Gaiberg. I find that the emission ratios strongly depend on the contributions from bio-fuelled heating systems. The agreement between TNO inventory emission ratios and measured effective atmospheric emission ratios hinges on the inventory proxy used to distribute bio-fuelled heating emissions. For Gaiberg, the agreement is good, but for Leimen the influence of bio-fuelled heating systems is strongly underestimated by the TNO inventory.

The two heating campaigns will be reviewed one after the other. Results will also be presented separately at first and jointly in the comparison Section 4.4.

Parts of this chapter are taken (sometimes verbatim) from Deliverable 2.8 of the VERIFY Project[17]. Section 4.3 was written after the submission of Deliverable 2.8.

4.1 Preliminary considerations

Heating emissions cannot be isolated spatially from traffic emissions. For the temporal isolation, the diurnal profiles of the sectors are analysed.

Residential heating emissions have seasonally changing diurnal patterns depending on ambient temperature and human behaviour (Gadd and Werner, 2013). Especially during shoulder seasons, when the campaigns took place, the nocturnal heat demand is relatively constant and at its diurnal minimum, but the heating systems still operate at base-load conditions. The heat demand increases 4 to 6-fold in the early morning hours between 04:00 h and 06:00 h local time. This peak in heat demand is due to the consumption of hot water and the heating of living areas at the beginning of the daily human routine (Heitkoetter et al., 2019),

---

[17] I authored Deliverable 2.8 in collaboration with Samuel Hammer. Please refer to the online documentation Rosendahl et al. (2021). All Deliverable contributions written by KIT members Carlos Alberti and Frank Hase (remote sensing approach) are not in this thesis.

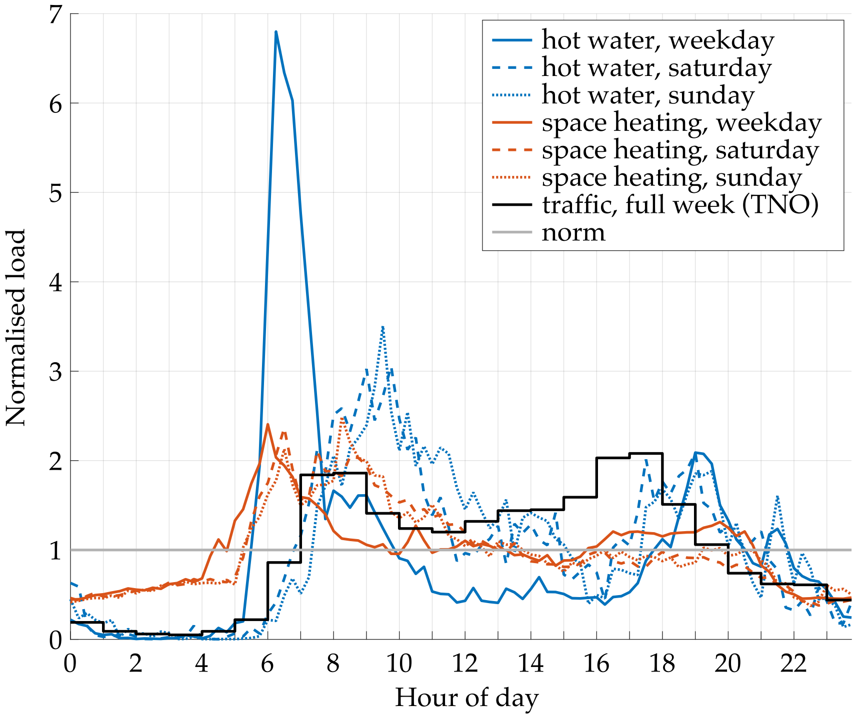

Fig. 4.1 Time profile of normalised traffic, domestic hot water, and space heating loads. For traffic, the TNO time profile is used. For space heating and domestic hot water, supplementary material from Heitkoetter et al. (2019, cf. Figs. 14 and 15 in the manuscript) is used. Note that for the heating data from Heitkoetter, load refers to area specific heat demand (without declaring how the demand is met i.e. by which heating system), while the TNO traffic load refers to emissions directly.

see Fig. 4.1. Depending on the type of heating systems, ambient temperatures and individual human behaviour, the heating demand during the day is 1 to 3-fold the nocturnal demand. In the evening hours between 17:00 h and 22:00 h, the second smaller and much broader heating demand peak occurs with about 2 to 4 times the nocturnal demand (Heitkoetter et al., 2019). Hence, the diurnal cycle of the ffCO$_2$ emissions from the residential heating sector is different from the one of traffic or industry. As shown in Fig. 4.1, traffic emissions are directly linked to human movement and thus minimal during night, even lower than residential emissions operating in base-load conditions[18]. Traffic emissions typically start at 05:00 h and strongly peak between 07:00 h and 09:00 h local time. High traffic emission persists throughout the day with a smaller and broader peak in the evenings between 16:00 h and 19:00 h. After that, the traffic emissions decrease towards their nocturnal minimum.

---

[18] The traffic and residential heating sector contribute 19 % and 16 % of the ffCO$_2$ emissions in Germany, therefore the displayed normalised *relative* difference translates very well into an *absolute* difference as well

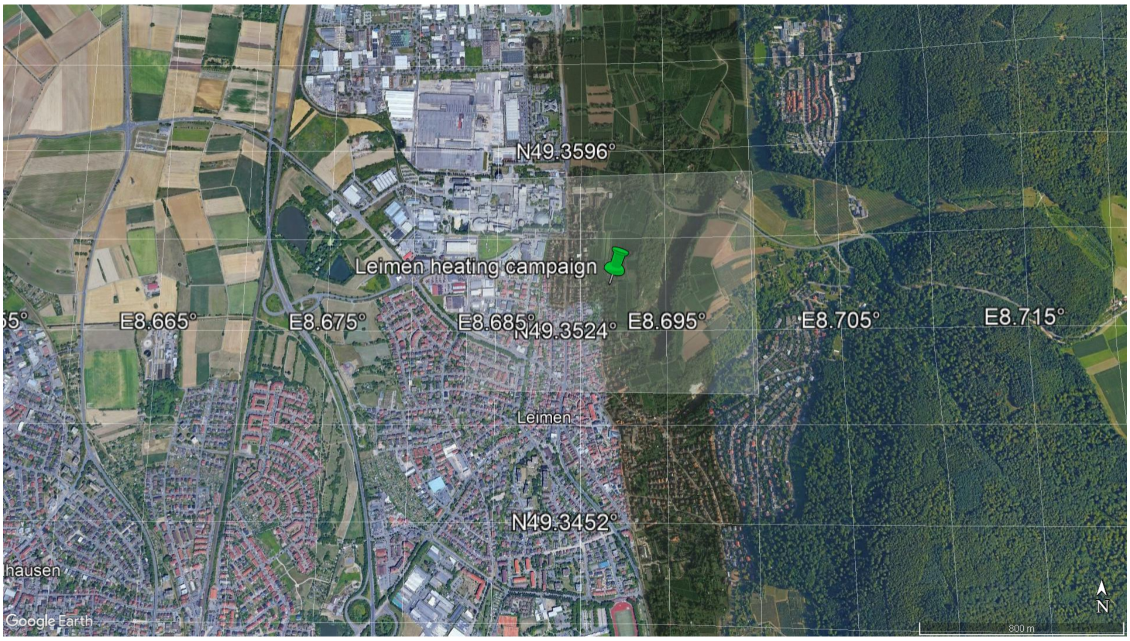

Fig. 4.2 Overview of the Leimen heating campaign site (Google Earth). The lightly shaded rectangle indicates the TNO emission inventory cell used for comparison.

To maximise the influence of the residential heating sector when applying the single-station approach, we focus on the observations during the nocturnal build-up before the strong traffic emissions in the morning start. According to the diurnal cycles of traffic and residential heating, the strongest heating imprint can be expected between 4:00 h and 5:00 h when the heating systems started, but the traffic is still very limited.

4.2 Leimen campaign, 2020

We applied the single-station approach in a semi-urban residential area, sampling between late evening and early morning to target residential heating emissions specifically.

Campaign setup and site description. We conducted the residential heating campaign in Leimen, Germany (lat. 49.352° N, long. 8.691° E, alt. 138 m asl) from March 27 to April 2, 2020. Leimen is located on the east edge of the Upper Rhine Valley, partially elevated by the offshoots of Odenwald, a mountain ridge confining the Upper Rhine Valley to the east. Figure 4.2 shows an aerial image (Google Earth) of the measurement site, located at the end of a dead-end road to avoid emissions from transit traffic. The closest, more significant road is located

Table 4.1
Instruments used in Mobile Laboratory 1 for the residential heating sector campaign. Reproducibilities are based on target cylinder measurements: the offset (measurement minus assign cylinder value) to the calibrated value and the standard deviation of the measurements are given. Entry for ICAD and weather station based on precision described in instrument manual.

Use period	Instrument	Function	Reproducibility	Temporal resolution
Mar 17 to Apr 2, 2020	Picarro G2301	CO_2 recordings	CO_2: −0.03 ± 0.51 ppm	1 s, averaged to minutes
Mar 17 to Apr 2, 2020	AEROLASER L5001	CO recordings	CO: −1.01 ± 8.49 ppb	1 s, averaged to minutes
Mar 17 to Apr 2, 2020	ICAD05	NO_2 and NO_x recordings	NO_x: 0.15 ppb or 2 % NO_2: 0.15 ppb or 2 %	60 s
Mar 17 to Apr 2, 2020	Flask sampler	collects 1 h-accumulated air samples	–	–
Mar 17 to Apr 2, 2020	Heidelberg Radon Monitor	^{214}Po recording, ^{222}Rn estimation	–	30 min
Mar 17 to Apr 2, 2020	Thies weather station	wind speed, wind direction	speed: ±0.3 m/s direction: ±2°	1 s, averaged to minutes

in a westerly direction at a distance 150 m. The houses in the immediate vicinity comprise different heating systems using different fuels. The nearest five houses use oil-fuelled heating systems. Further to the south, oil- and gas-fuelled heating systems are supported by wood-fuelled tiled and fireplace stoves. To the best of our knowledge, no coal-fired heating systems exist in Leimen.

Although the timing of the campaign was quite late in the seasonal heating period, the average temperature was 5.4 °C with typical night time (18:00 h to 6:00 h) temperatures of 0 °C to 5 °C (mean 3.1 °C) and daytime (06:00 h to 18:00 h) temperatures of up to 12.5 °C (mean 7.6 °C). The actual temperatures measured during the campaign are given in Fig. 4.3 in the lowest panel.

Table 4.1 shows the instruments used for the heating campaign, including reproducibilities and temporal resolutions. While the performance of the Picarro G2301 was stable, the AEROLASER L5001 showed stability issues. Throughout the whole campaign, the sensitivity fell off by 12.5 % and the instrument temperature was unstable. However, this is of no strong concern for the evaluation, since in this campaign the continuous data were used for quality checks only. As a consequence of the unstable AEROLASER instrument, CO was not used as a quality check between continuous in-situ measurements and flask measurements. Quality

Table 4.2
Background samples and averaged background concentrations of the heating campaign in Leimen. The NO_x instrument failed during the first measurement, so no average NO_x concentration is available. For $\Delta^{14}CO_2$, the uncertainty of the mean is a combination of the standard deviation and the measurement uncertainty of the three measurements.

Date	CO_2 (ppm)	CO (ppb)	NO_x (ppb)	Rn (Bq/m^3)	$\Delta^{14}C$ (‰)	$\Delta^{13}C$ (‰)
Mar 30 7:00 h	421.35 ± 0.04	143.90 ± 5.17	–	0.62	−7.52 ± 2.24	−9.15 ± 0.03
Mar 31 9:30 h	421.88 ± 0.04	153.13 ± 1.01	2.12 ± 0.09	1.97	−8.58 ± 2.24	−9.24 ± 0.02
Apr 1 1:30 h	422.57 ± 0.04	150.74 ± 0.47	1.42 ± 0.02	1.91	−9.06 ± 2.27	−9.44 ± 0.01
Mean ± SD	421.93 ± 0.61	149.26 ± 4.79	1.77 ± 0.49	1.50	−8.38 ± 3.04	−9.28 ± 0.15

checks with the Picarro data were still possible. The agreement between flasks and in-situ concentrations was better than 1 ppm for CO_2.

Results and discussion. Twenty flasks were sampled during the Leimen heating campaign. The first two flasks were discarded because no suitable background sample was available. The remaining 18 flasks were analysed for $\Delta^{14}CO_2$ to derive $\Delta ffCO_2$ estimates using Eq. (2.6). We use this equation because we expect biospheric activity at the start of spring. Figure 4.3 gives an overview of the continuous in-situ measurements from March 30, 2020 6:00 h to April 2, 2020 4:00 h.[19] The first four panels show CO_2, CO, NO_x (NO_x in red, NO_2 in blue), and ^{222}Rn concentrations. The lower three panels show the meteorological parameters wind speed, wind direction, and temperature. Vertically shaded bars depict flask sampling times. Each flask sample is numbered in the order of appearance. We screened the three-day observation period for background conditions applying two criteria low ^{222}Rn concentrations and moderate wind speeds. Samples #3, #8 and #9 fulfil these criteria.

Table 4.2 summarises the concentrations and the isotopic composition for those three background flasks. Although the flasks were taken on different days and at different times of the day, they all show a remarkable agreement between their concentrations. We conclude that this is a representative estimate of the background concentrations that occur when the locally polluted air is removed and replaced by fresh air. Thus, for the remaining evaluation, the average of these three events is used as background concentration for the individual species.

The first three panels of Fig. 4.4 show the continuously measured local trace gas enhancements ΔCO_2, ΔCO, and ΔNO_x with respect to average background concentrations. The red stars show enhancements for the flask sampling time

---

[19] Measurements stopped abruptly due to electrical failure of the instrument drying the air for the other instruments.

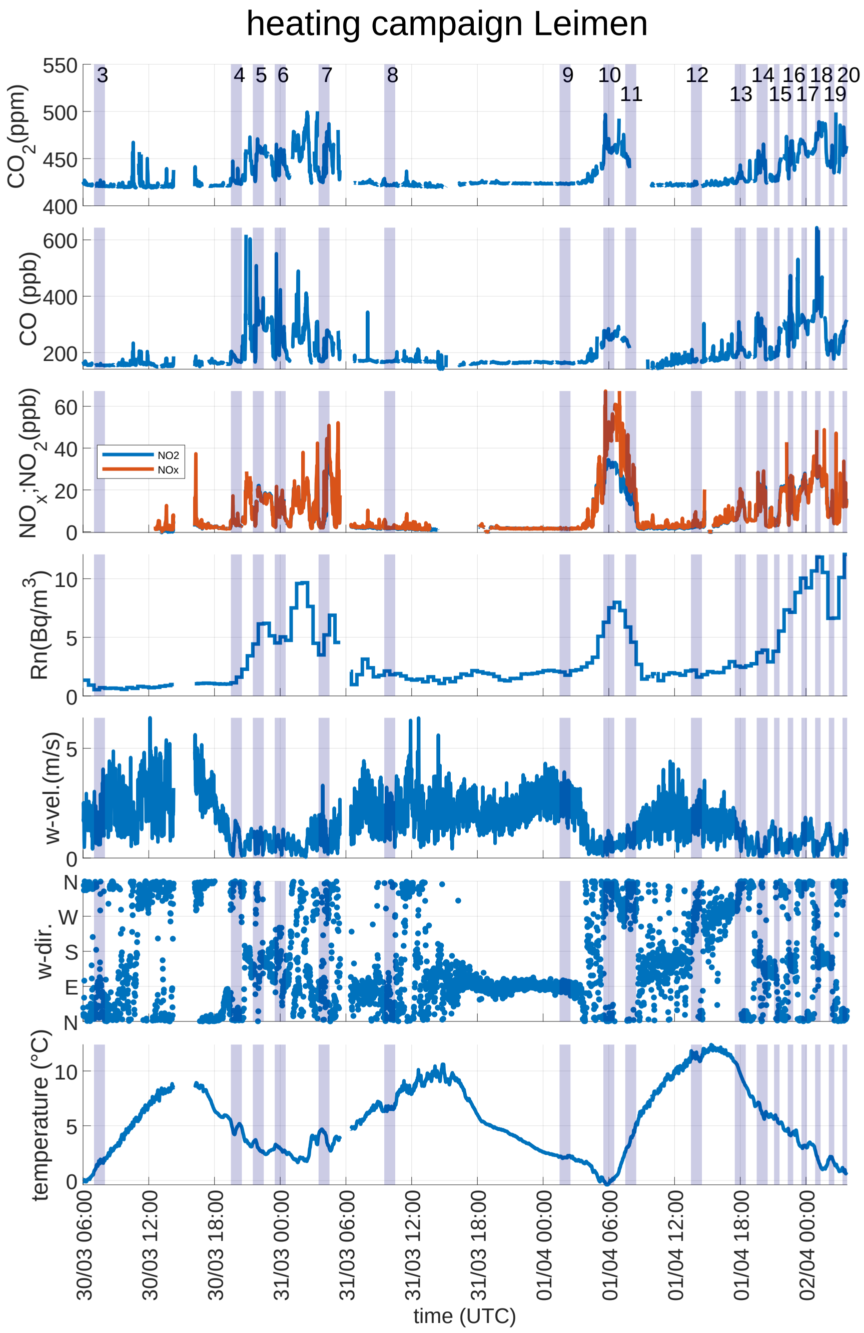

Fig. 4.3 Overview of the continuous in-situ measurements for the Leimen heating campaign. The first four panels show CO_2, CO, NO_x (NO_x in red, NO_2 in blue), and ^{222}Rn concentrations. The lower three panels show the meteorological parameters wind speed, wind direction, and temperature. Vertically shaded bars depict flask sampling times. The flask numbers referred to in the text are displayed at the very top of the CO_2 panel.

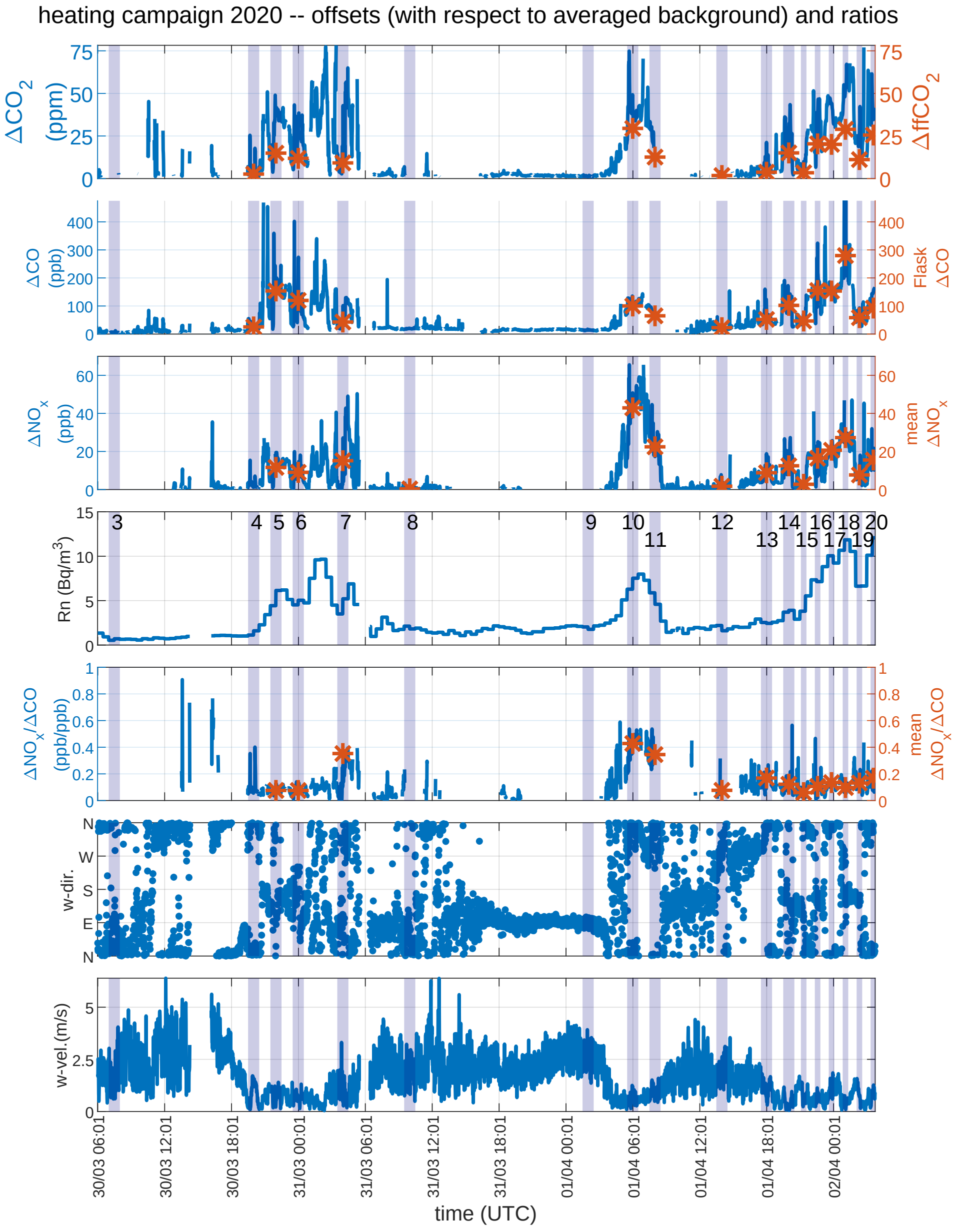

Fig. 4.4 Concentration enhancements during the Leimen heating campaign, 2020. This graph is akin to Fig. 4.3, only that the average background (defined by samples #3, #8, and #9) has been subtracted from the continuously measured concentrations. Flask numbers are shown in the Radon panel (central panel). The red stars indicate flask values ($\Delta ffCO_2$, ΔCO in the top two panels) and mean concentrations (ΔNO_x in panel 3). For the red stars in panel 5, ΔNO_x is divided by ΔCO from the flask measurements to calculate the $\Delta NO_x/\Delta CO$ ratio.

according to the right axis. In the ΔCO_2 panel, the $^{14}CO_2$-based $\Delta ffCO_2$ estimates are shown. In the ΔCO panel, the red stars are derived from the flask measurements providing independent quality checks for the in-situ measurements, while in the ΔNO_x panel, the red stars give the averaged ΔNO_x value for the flask sampling period. The fourth panel shows the $\Delta NO_x/\Delta CO$ ratio of the in-situ NO_x data and the CO flask data. The atmospheric transport-related variability observed in the individual enhancements cancels out in the ratio as both tracers are subject to the same atmospheric transport (assuming no demixing). The last three panels show ^{222}Rn, wind speed, and wind direction, similar to Fig. 4.3, to indicate atmospheric conditions.

Looking at the ^{222}Rn concentrations in Fig. 4.3, we can identify three events with reduced atmospheric mixing:

- Event I from March 30, 18:00 UTC to March 31, 6:00 UTC
- Event II from April 1, 3:00 UTC to April 1, 9:00 UTC
- Event III from April 1, 18:00 UTC to April 2, 4:00 UTC

Low wind speeds and accumulating trace gas concentrations characterise all three events. The temporal variations of ΔCO_2, ΔCO, and ΔNO_x, are strongly correlated throughout the entire period.

During event I (March 30, 18:00 UTC to March 31, 6:00 UTC), the CO_2, CO, and NO_x enhancements fluctuated strongly and almost down to background levels. Joint interpretation of wind conditions and CO_2 enhancements (Fig. 4.5a) showed that enhanced wind speeds and northerly directions are correlated with lower ΔCO_2, while high ΔCO_2 was dominant at low wind speeds. Also, the ^{222}Rn build-up is interrupted before samples #6 and #7. We interpret this as flushes of 'fresh' air. As the individual concentration build-ups occur during low wind speeds, we conclude that we measured local source emissions during this event. Sample #7 was collected at the end of the event at 4:00 UTC (6:00 h local time), and the $\Delta NO_x/\Delta CO$ ratio of #7 is three times higher compared to the earlier samples. Based on the timing, a mix between heating and traffic emissions can be expected and, hence, sample #7 will be excluded.

Event II (April 1, 3:00 UTC to April 1, 9:00 UTC) is different from event I. Figure 4.3 shows only for event II a split between NO_x and NO_2. That is, the NO_x signal contains NO. In Fig. 4.4 it is shown that the $\Delta NO_x/\Delta CO$ ratio changes significantly during this event and is three to four times the ratio observed during event I. The build-up of event II started around 4:00 UTC (6:00 h local time). The first flask was sampled between 6:00 and 7:00 UTC. Similar to sample #7, samples #10 and #11 are excluded when determining the average heating emission ratios.

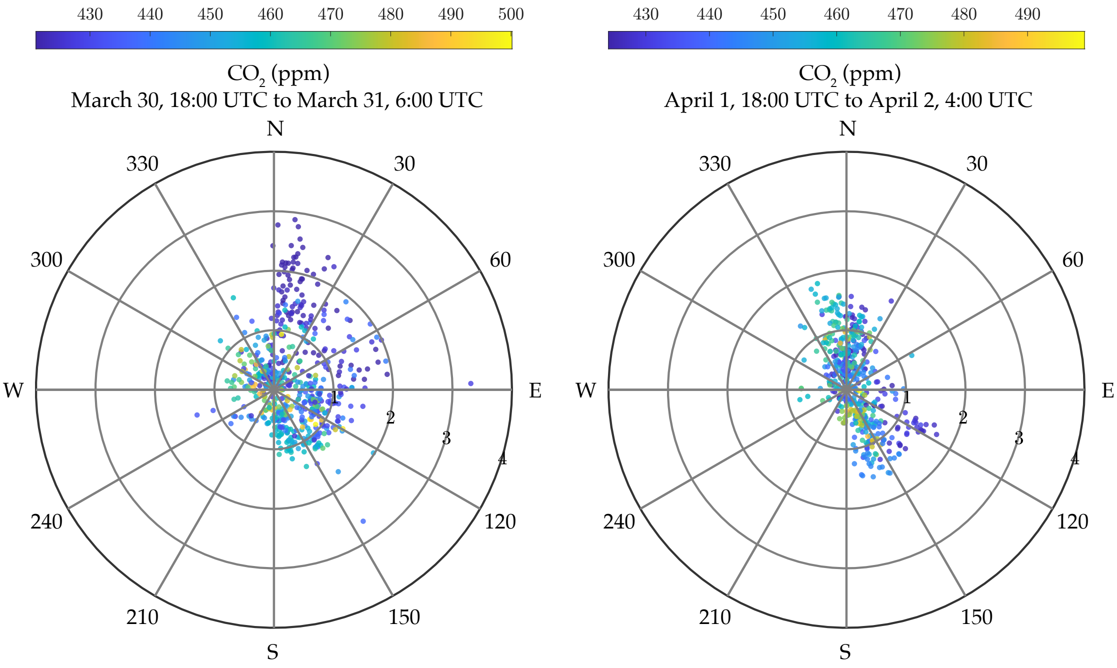

(a) Event I **(b)** Event III

Fig. 4.5 Correlation between CO_2 concentration and wind direction for two events during the Leimen heating campaign. The radial axes describe wind velocity (one ring corresponds to 1 m/s).

Event III (April 1, 18:00 UTC to April 2, 4:00 UTC) shows similarities to event I. In the beginning, we see a gentle ^{222}Rn build-up, which is accelerating after 22:00 h local time. Around 4:00 h local time, the decrease in ^{222}Rn indicates a contribution of 'fresh' air. Combining wind and ΔCO_2 data confirms the earlier finding that larger ΔCO_2 go along with lower wind speeds (Fig. 4.5a for event I and Fig. 4.5b for event III). Apart from sample #13 taken at 18:00 UTC (20:00 h local time), which still may contain traffic emission contribution, the remaining samples #14 to #20 have been sampled during conditions where the residential heating emissions dominate.

Apart from the flasks sampled during background conditions (#3, #8, and #9), only flask #12 was not sampled during one of three events. Flask #12 was taken at 8:00 UTC (10:00 h local time) and is, hence, not suited for determining the heating ratios. From the remaining flasks, #6 and #14 are excluded, too. Flask #6 shows considerably higher CO_2 concentrations than the mean of the continuous measurements over the hour ($\Delta CO_2 = 2.7$ ppm), marking a situation where atmospheric conditions were too unstable and consequently, due to slight asynchronicity or the imperfect weighing function of the flask sampling, lead to a discrepancy of the means. Flask #14 was contaminated with $^{14}CO_2$ from nuclear facilities (according to WRF-STILT modelling of Fabian Maier) and was

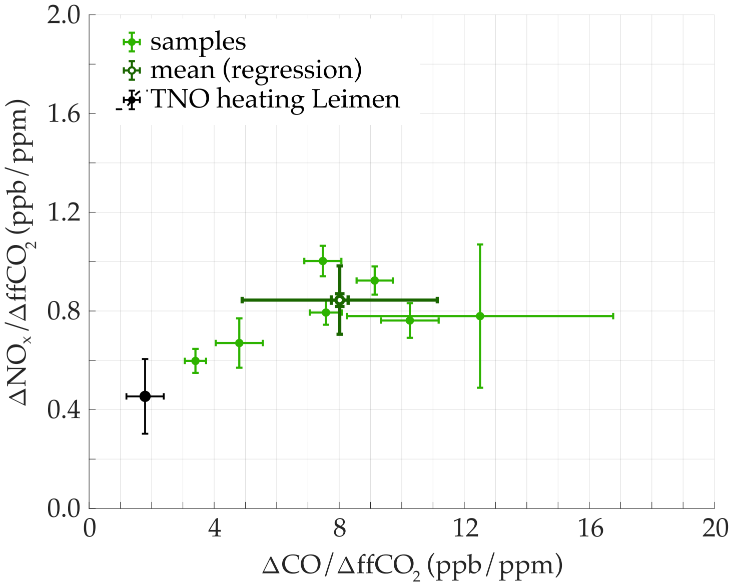

Fig. 4.6 Δproxy/ΔffCO_2 ratios for the heating campaign in Leimen. For reference, heating emission ratios from the TNO cell containing the campaign site are shown in black. Light-green points are individual measurements, the dark green point gives an estimate of the average ratios, obtained by regression of Δproxy versus ΔffCO_2 with a forced intercept of 0. See Section 2.4 for details on the regression-mean. The regression lines are plotted in Fig. 4.7. The small error bars of the mean show the uncertainty of the regression slope, the large error bars show the standard deviation of the individual ratios.

thus excluded. We use the remaining seven signal flasks to determine heating proxy emission ratios.

Figure 4.6 shows Δproxy/ΔffCO_2 ratios in a double ratio plot to compare our measured effective atmospheric heating-dominated emission ratios to TNO inventory emission ratios for the cell containing the campaign site. The ratios for individual flask samples are plotted in light green, whereas the mean (determined via weighted total least squares regression, see Appendix D) is dark green. The mean heating ratio has two error bars. The smaller error is the uncertainty of the fit parameter of the linear regression, when the origin is a fixed point. The regressions for CO and NO_x are displayed in Fig. 4.7.

The uncertainty of the slope fit parameter of the linear regression underestimates the variability of the mean ratio. Therefore, the second, larger error bar is the standard deviation of the individual proxy emission ratios. Estimating the uncertainty of the mean proxy emission ratios by taking the standard deviation is reasonable, because, conceptually, we do not measure one specific heating emission ratio, but rather multiple variations, i.e. every sample experiences a different fuel-mix and consequently a different heating ratio. The mean heating

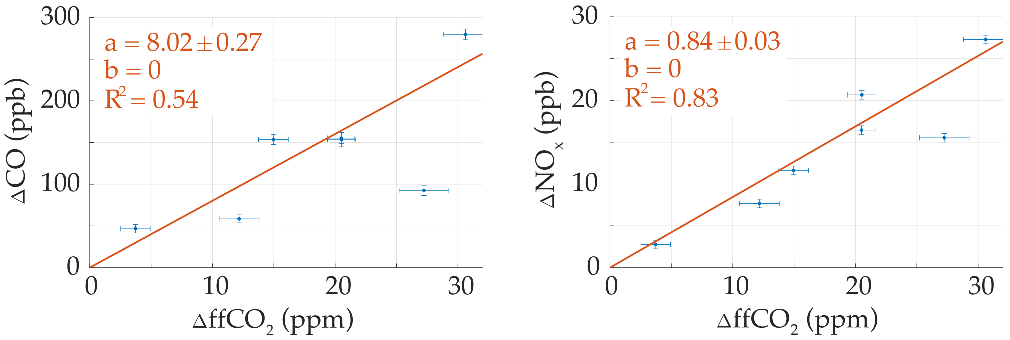

Fig. 4.7 Weighted total least square regressions for the mean in Fig. 4.6. The origin is fixed for the regression ($b = 0$). Uncertainties are calculated from measurement uncertainties by Gaussian error propagation. The uncertainty of the slope parameter a underestimates the real uncertainty of the mean heating emission ratio.

emission ratio and its uncertainty just give us an idea about how the possible heating ratios are distributed.

The average heating emission ratios estimated from our measurements are $\Delta CO/\Delta ffCO_2 = 8.02 \pm 3.12$ ppb/ppm and $\Delta NO_x/\Delta ffCO_2 = 0.84 \pm 0.14$ ppb/ppm. Both ratios exceed the prediction of TNO ($\Delta CO/\Delta ffCO_2 = 1.79$ ppb/ppm and $\Delta NO_x/\Delta ffCO_2 = 0.45$ ppb/ppm). An explanation for this will be presented in the discussion of Fig. 4.14.

4.3 Gaiberg campaign, 2021

The single-station approach was applied in a rural residential area where no gas network exists. Consequently, a different ratio distribution than in Leimen is expected.

Campaign setup and site description. We conducted the residential heating campaign in Gaiberg, Germany (long. 49.364° N, lat. 8.754° E, alt. 290 m asl) from March 17 to March 28, 2021. Gaiberg is located on a plateau at the south west end of the Odenwald, east of the Upper Rhine Valley, approximately 5 km to the east of Leimen. Gaiberg is a roughly star-shaped town, where the main road (roughly from west to east) slopes downward. ML1 was parked on an even-levelled road at an elevation of 290 m asl[20] in the south eastern residential area, which is elevated between 280 m asl and 295 m asl. The main road is located in northerly direction at a distance just short of 150 m at an elevation of 280 m asl. Oil-fuelled heating

---

[20] Placement of the mobile laboratory was restricted to proximity of the house of Jochen Wallwein, who graciously provided the electricity.

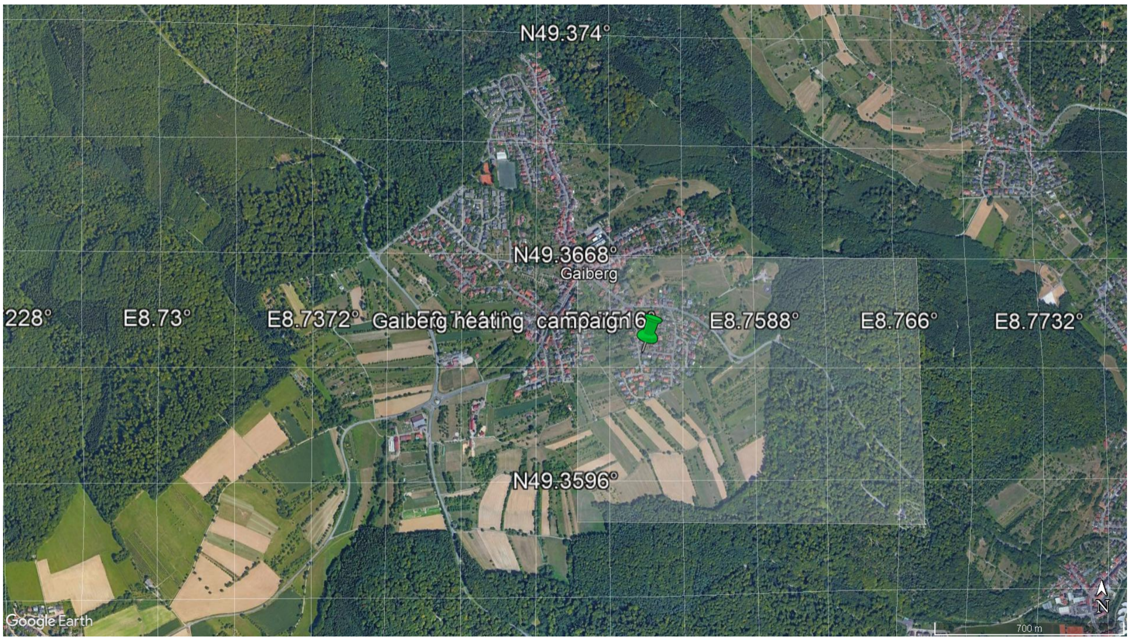

Fig. 4.8 Overview of the Gaiberg heating campaign site. The lightly shaded rectangle indicates the TNO emission inventory cell used for comparison.

systems are the most prevalent in the neighbourhood, only one house in westerly direction uses gas from a subterranean tank. Figure 4.8 shows an aerial image (Google Earth) of the measurement site. Gaiberg is more isolated than Leimen, separated from other towns by ridges of the Odenwald.

This campaign started slightly earlier in March than the Leimen campaign. Temperatures during sampling were between 4 °C and 5 °C for four of the five signal samples. The last sample was taken during a rather warm night with a temperature of circa 11 °C. I judge the heating campaigns similar enough in both season-wise timing and temperatures to be comparable, i.e. even though the campaigns were not conducted back-to-back, I expect heating behaviour to be similar between the two.

The instruments used in this campaign are listed in Table 4.3 with their reproducibilities. Reproducibilities of the G2401 Picarro decreased between the traffic campaign and the Gaiberg heating campaign. For ratio calculations, only flask data were used. That is, the results are unaffected. Quality checks with the Picarro data were still possible and agreement between flasks and in-situ concentrations was better than 1 ppm for CO_2 and better than 10 ppb for CO.

Results and discussion. Eight flasks were sampled during this heating campaign and subsequently analysed for $^{14}CO_2$. Equation (2.6) was used to calculate

Table 4.3
Instruments used in Mobile Laboratory 1 for the residential heating sector campaign in Gaiberg. Reproducibilities are based on target cylinder measurements: the offset to the calibrated value and the standard deviation of the measurements are given. Entry for ICAD and weather station based on precision described in instrument manual.

Use period	Instrument	Function	Reproducibility	Temporal resolution
Mar 17 to Mar 28, 2021	Picarro G2401	CO_2, CO recordings	CO_2: 0.22 ± 0.25 ppm CO: −5.44 ± 1.27 ppb	1 s, averaged to minutes
Whole campaign	ICAD05	NO_2 and NO_x recordings	NO_x: 0.15 ppb or 2 % NO_2: 0.15 ppb or 2 %	60 s
Mar 17 to Mar 28, 2021	Flask sampler	collects air samples	–	–
Mar 17 to Mar 28, 2021	Heidelberg Radon Monitor	^{214}Po recording, ^{222}Rn estimation	–	30 min
Mar 17 to Mar 28, 2021	Thies weather station	wind speed, wind direction	speed: ±0.3 m/s direction: ±2°	1 s, averaged to minutes

$\Delta ffCO_2$ (nuclear source influence was negligible, but biospheric influence was not). Figure 4.9 shows the continuous in-situ measurements. Samples were collected during three day-night periods between March 22 and March 27, 2021. For each period, one flask was sampled in the afternoon during well-mixed conditions to function as a background for the night-time samples. The offset between signal and background is shown in Fig. 4.10. Taking daily noon or afternoon samples as background is a different approach than the one applied in Leimen.

For Leimen, we found that all background flasks had very similar trace gas concentrations and isotopic compositions, see Table 4.2, indicating that all background flasks essentially sample the same background air-mass. This is not the case for Gaiberg. ^{222}Rn data in Fig. 4.9 suggest an air-mass change in the early hours of March 26, where the ^{222}Rn concentration abruptly increased with a change of wind direction and does not decrease when the wind speed increases. The first two background flasks on March 22 and 23 are more similar, as Table 4.4 shows. Comparing the standard deviation of the means in Tables 4.2 and 4.4 exemplifies this. For CO_2 the SDs differ by a factor of approximately 8, for CO by a factor of approximately 3, and for NO_x by a factor of 4. For the first two background flasks of Gaiberg, the difference in CO_2, NO_x, and ^{222}Rn is fairly low. They differ more in CO and $\Delta^{14}CO_2$ than all Leimen background flasks, even though the two Gaiberg flasks are less than 24 hours apart. I conclude that while for Leimen the assumption that all background flasks essentially sample the same background holds, this is not the case in Gaiberg. Therefore,

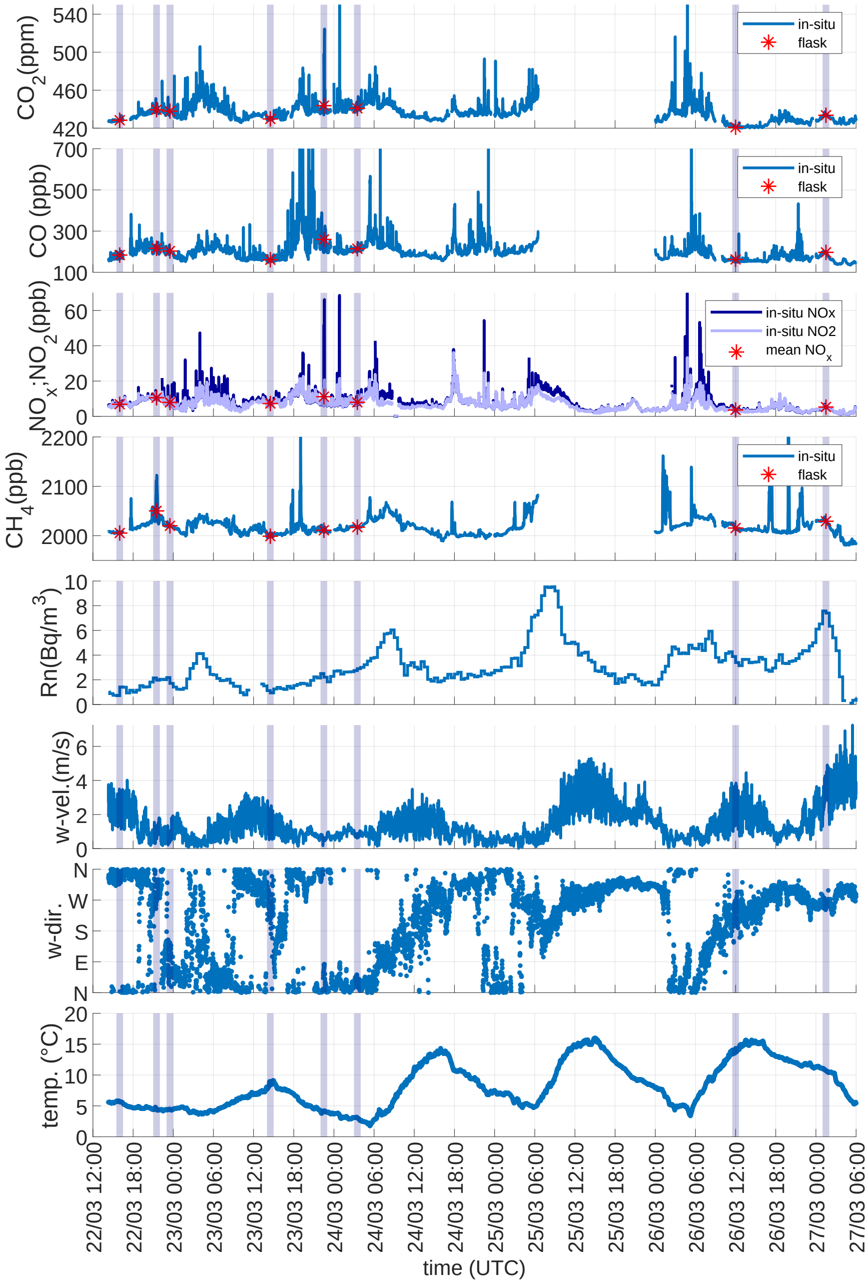

Fig. 4.9 Overview of the continuous in-situ measurements for the first sampling period of the Gaiberg heating campaign. The first four panels show CO_2, CO, NO_x (NO_x in dark blue, NO_2 in light blue), and ^{222}Rn concentrations. The lower three panels show the meteorological parameters wind speed, wind direction and temperature. Vertically shaded bars depict flask sampling times. Red stars are flask concentrations or, in the case of NO_x, the mean concentration during sampling.

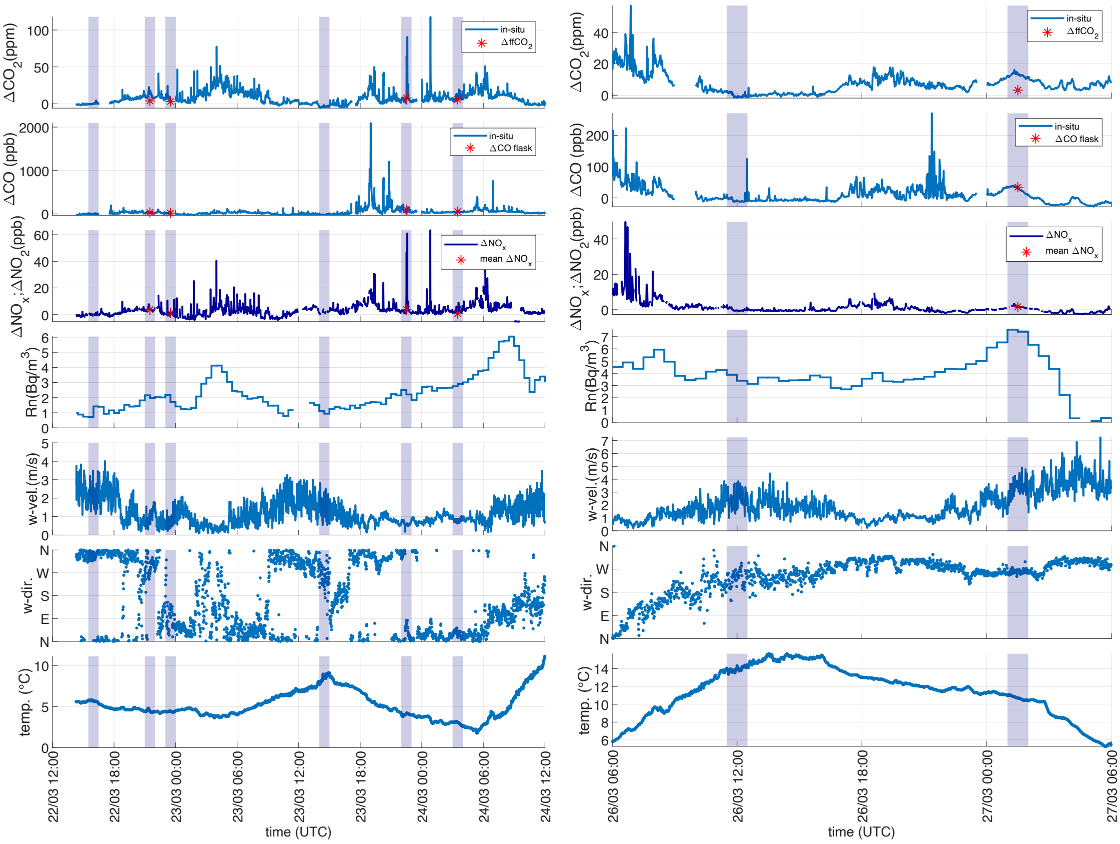

Fig. 4.10 Concentration enhancements during the sampling periods of the Gaiberg heating campaign. This graph is similar to Fig. 4.9, only that the background (defined by the corresponding afternoon sample, vertical blue bar without red star in the center) has been subtracted from the continuously measured concentrations. Red stars show (from top to bottom) $ffCO_2$, CO offset between signal and background flask, mean NO_x offset during sampling of signal and background flask, and CH_4 offset between signal and background flask.

the assumption for Gaiberg is that the nightly concentration build-up is on top of the midday 'clean air' concentration, which I call the day-by-day ansatz. The evaluation method employed during the Leimen campaign is preferable, because Peter (2020) found that midday flasks do not necessarily reflect the true (free troposphere) background, but contain residual anthropogenic emissions that pollute the background sample, leading to skewed proxy emission ratios.

The third Gaiberg background flask is of special interest, because its Rn concentration is much larger than for the two other background flasks, but its CO_2 concentration is almost 10 ppm lower. The sunny weather accompanied by warm temperatures on March 26 suggest that the biosphere was no longer dormant and the CO_2 draw-down effect by photosynthesis caused the low CO_2 concentration.

Table 4.4
Background samples and averaged background concentrations of the heating campaign in Gaiberg, 2021. The mean is not used for calculations and is displayed here only to signify the difference between the two heating campaigns.

Date	CO_2 (ppm)	CO (ppb)	NO_x (ppb)	Rn (Bq/m^3)	$\Delta^{14}C$ (‰)
Mar 22 15:00 h	428.36 ± 0.02	183.53 ± 0.14	6.85 ± 0.09	1.07	−23.61 ± 2.02
Mar 23 13:30 h	429.71 ± 0.04	160.79 ± 0.48	7.28 ± 0.15	1.04	−26.64 ± 1.77
Mar 26 11:00 h	420.95 ± 0.04	162.45 ± 0.30	3.60 ± 0.10	3.63	−10.24 ± 1.72
Mean ± SD	426.34 ± 4.72	168.92 ± 12.67	5.91 ± 2.01	1.91	−20.16 ± 8.73

In any case, all the background flasks differ markedly in at least two tracer concentrations. Hence, I cannot determine one true background and I am forced to use the day-by-day ansatz.[21]

The Gaiberg campaign can be separated into three periods:

- Period I from March 22, 12:00 UTC to March 23, 0:00 UTC
- Period II from March 23, 12:00 UTC to March 24, 6:00 UTC
- Period III from March 26, 18:00 UTC to March 27, 6:00 UTC

each with their own midday background sample and one (period III) or two (periods I and II) signal samples (Fig. 4.9). Periods I and II are similar in many ways. Both show a build-up in ^{222}Rn over the day, starting from roughly 1 Bq/m^3 to 2 to 3 Bq/m^3 in the night. Night temperatures are similar (5 °C or less) and the wind pattern is favourable – high wind speeds during the day and low wind speeds during the night – matching the concept of clean air background samples and locally influenced signal samples (Fig. 4.11a).

After period II, the daily temperature maximum increased from 5 to 10 °C to 15 °C, indicating a weather change that affected period III, displayed in the bottom panel in Fig. 4.10. While ^{222}Rn also increased between the background sample and the signal sample in period III, the background sample already contained 4 Bq/m^3. Together with the temperature profile, the ^{222}Rn profile can be interpreted in the following way. A large air-mass from the south-west/west brought warm continental air passing over Gaiberg. Over night, an inversion started and increased the ^{222}Rn load until it reached a maximum of 7 Bq/m^3. Shortly after, at around 3:00 h UTC in the morning, strong winds brought fresh, slightly colder air-masses from the west, visible through the rapid drop in ^{222}Rn accompanied by a decline in temperature. The adverse wind conditions are also visible in Fig. 4.11b.

---

[21] Note that for a long time, this was the go-to ansatz in our group, until Peter (2020) revealed its shortcomings. While this ansatz is inferior it is by no means inapplicable.

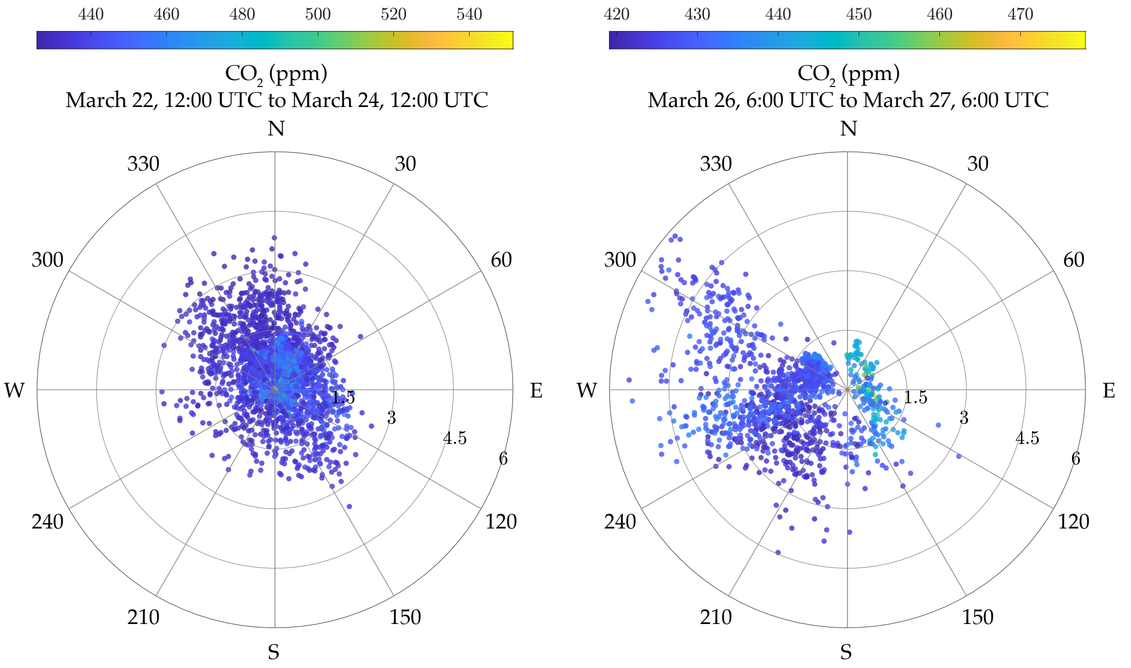

(a) Periods I and II

(b) Period III

Fig. 4.11 Dependence of CO_2 concentration on wind direction during the Gaiberg heating campaign. The radial axes describe wind velocity (each ring is 1.5 m/s). Periods I and II are shown together, since they are also shown together in Figs. 4.9 and 4.10 and are very similar with regard to their meteorological conditions.

When, at the start of the depicted period (March 26, 6:00 UTC), the wind turned from North over East to South, wind speeds were low and concentrations high – an optimal sampling situation but unfortunately not sampled. As the wind turned west and we moved into the night, the anti-correlation between wind speed and CO_2 concentration was no longer valid, i.e. high-speed winds brought an increase in CO_2 and ^{222}Rn. The only nighttime sources of $ffCO_2$ to the west are another Gaiberg residential area 150 to 350 m away, and much further to the west (approximately 3.5 km) Emmertsgrund, another residential area.

Even though the picture is much more complicated for period III, there is no reason to exclude the sample from the evaluation, since the sample is dominated by residential heating emissions, even though they may not come only from Gaiberg. In addition, exclusion would not change the mean ratio (i.e. the regression in Fig. 4.12 would not change; the period III flask is the point closest to the regression for both CO and NO_x).

Similar to the Leimen heating campaign, the Δproxy/$\Delta ffCO_2$ ratios for Gaiberg are shown in a double ratio plot in Fig. 4.13. Uncertainties of individual ratios are dominated by the uncertainty in $\Delta ffCO_2$, which is roughly 1 to 1.2 ppm for all

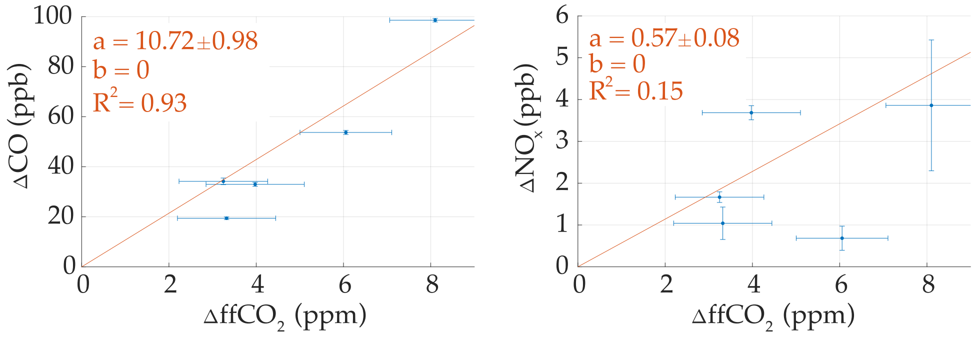

Fig. 4.12 Weighted total least square regressions for the mean in Fig. 4.13. The origin is a fixed for the regression ($b = 0$). Uncertainties are calculated from measurement uncertainties by Gaussian error propagation. The uncertainty of the slope parameter a underestimates the real uncertainty of the mean heating emission ratio. R^2 is very low for NO_x, this does not necessarily indicate no correlation. The sample size is too small for R^2 to be a good measure for correlation.

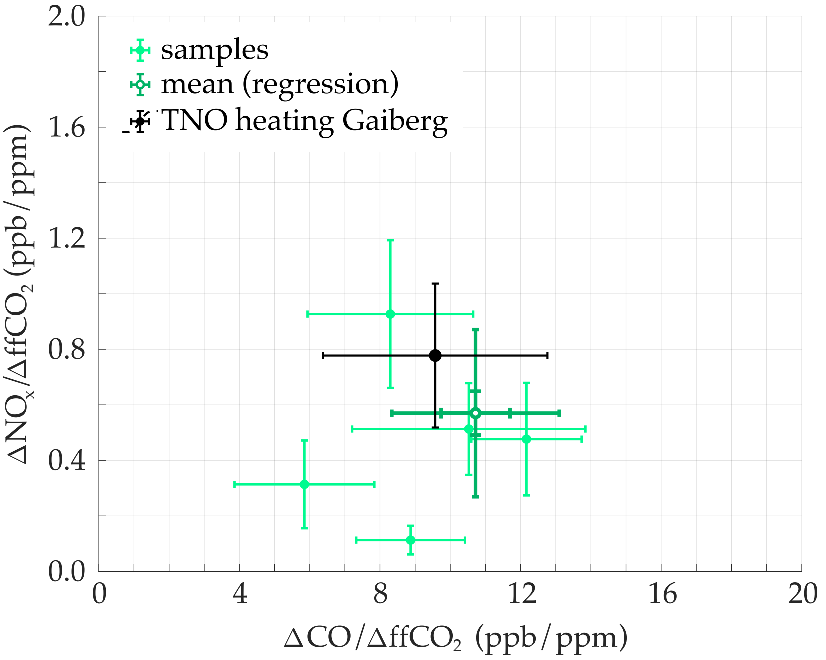

Fig. 4.13 Δproxy/ΔffCO$_2$ ratios for the heating campaign in Gaiberg. For reference, heating emission ratios from the TNO cell containing the campaign site are shown in black. Light-green points are individual measurements, the dark green point gives an estimate of the average ratios, obtained by regression of Δproxy versus ΔffCO$_2$ with a forced intercept of 0. See Section 2.4 for details on the regression-mean. Figure 4.12 shows the regression lines. The small error bars of the mean show the uncertainty of the regression slope, the large error bar show the standard deviation of the individual ratios.

samples. Concentration enhancements for Gaiberg were low compared to Leimen (3.2 to 8 ppm in Gaiberg compared to 11 to 28 ppm – with one exception at 3 ppm – in Leimen), resulting in relative errors of up to 33 %. In analogy to Fig. 4.6, the mean in Fig. 4.13 has two error bars. The smaller error bars show the uncertainty of the slope fit parameter of the linear regression, which once again underestimates of the variability of the mean ratio. Therefore the second, larger error bar is the standard deviation of the individual proxy emission ratios. The estimated average heating emission ratios are $\Delta CO/\Delta ffCO_2 = 10.72 \pm 2.38$ ppb/ppm and $\Delta NO_x/\Delta ffCO_2 = 0.57 \pm 0.30$ ppb/ppm. Both ratios match the prediction of TNO (9.5 ppb/ppm for CO and 0.78 ppb/ppm for NO_x) quite well. A detailed explanation for this will be presented in the discussion of Fig. 4.14.

4.4 Campaign comparison

Although the heating campaigns were conducted one year apart, the conditions (temperatures between 0 and 10 °C, season was end of winter, beginning of spring) were sufficiently similar to allow for a comparison of both campaigns.

The spatial disaggregation of heating emissions by the TNO model is key to understand Fig. 4.14, where agreement between proxy emission ratios of TNO and measurements is analysed. While total population density is used to distribute gaseous and liquid fuels[22], the proxy for biomass (e.g. wood) burning, is more intricate, taking into account not only rurality (rural means <250 inhabitants per km^2), but proximity to forested areas, too[23]. This way of assigning emissions puts Gaiberg in the rural category and Leimen in the urban category (the corresponding points in Fig. 4.14 are labelled accordingly). From Samuel Hammer, resident providing the power, we know that Leimen has a certain amount of heating by biomass burning, which puts the town closer to the 'rural' TNO ratios. The TNO spatial proxy does not have this level of detail and thus cannot (re)produce the emission ratios for Leimen correctly. TNO emissions suggest 7 % bio-fuel CO_2 for Leimen and 34 % for Gaiberg, supporting the hypothesis that the assignment of bio-fuel burning is too low for Leimen.

By definition, biomass burning never contributes to $ffCO_2$, while it does contribute to CO and NO_x, increasing the proxy emission ratios measured. Consequently, the rural TNO emission ratios are higher than their urban counterparts. This could also explain the difference in $\Delta CO/\Delta ffCO_2$ between Gaiberg and Leimen. The measured $bioCO_2$ enhancement in Gaiberg was, on average, 14 % higher

---

[22] Solid non-biomass fuels are distributed to rural populations (<250 inhabitants per km^2), but are negligible since barely any are burned in Germany

[23] personal communication with Stijn Dellaert on January 31, 2022

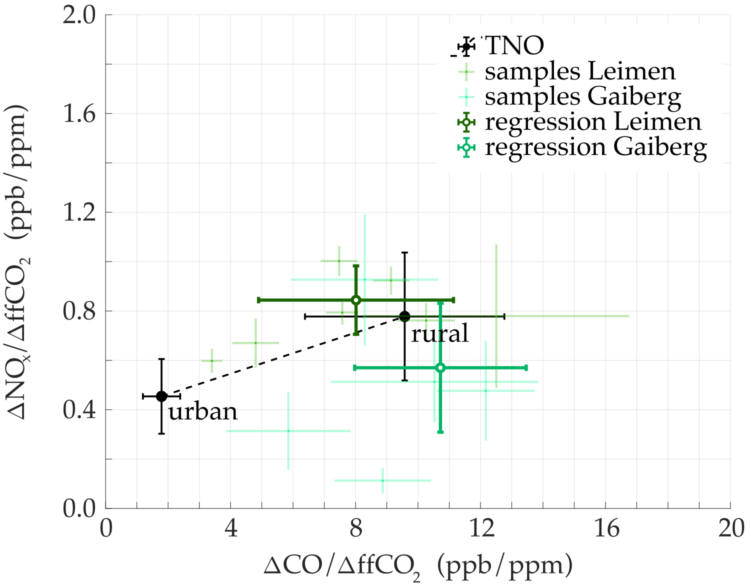

Fig. 4.14 Proxy ratios (CO, NO$_x$) plotted against each other. Estimated average ratios shown in dark and light green, for Leimen and Gaiberg, respectively, samples in the same color but faded. Error bars are standard deviations of individual ratios. Black points connected by a dashed line are TNO heating ratios for Leimen (labelled urban) and Gaiberg (labelled rural).

than in Leimen, which aligns with explanation given above (more bioCO$_2$, higher emission ratio). Biomass burning cannot explain why $\Delta NO_x/\Delta ffCO_2$ is higher in Leimen than in Gaiberg, even though the emission ratios agree within their uncertainties. The $\Delta NO_x/\Delta ffCO_2$ emission ratio strongly depends on the type of heating system, and can range from 0.10 ppb/ppm to 1.30 ppb/ppm (McDonald, 2009). Therefore, differences in the prevalent heating systems in Leimen and Gaiberg are a reasonable explanation for the difference in $\Delta NO_x/\Delta ffCO_2$.

In conclusion, biomass burning has a significant impact on measured proxy emission ratios, since only proxy enhancements are increased and $\Delta ffCO_2$ is not. If our understanding of the emission ratios is correct, Gaiberg and Leimen both exhibit sizeable biomass burning contributions. The TNO proxy for biomass burning considers proximity to forested areas and reproduces the emission ratios for Gaiberg. Leimen's biomass burning is on par with Gaiberg's, but not captured in the TNO proxy. Consequently TNO underestimates proxy emission ratios for Leimen.

Perspectives. For future campaigns, location and length of the campaigns will be key. Since I was able to confirm that TNO captures rural emission ratios quite well (if the area is correctly identified by the proxy for biomass burning), following campaigns should focus on urban heating emissions. Urban residential heating is fuelled by oil and gas as well as district heating (which, of course, does not contribute to local emissions). Future campaigns would have to show if emissions from gas heating systems and oil heating systems are as 'clean' (i.e. low in proxy emissions) as TNO and other sources (e.g. measurements by chimney sweepers) suggest, after some time in the 'reaction chamber' of the boundary layer.

Since it is impossible to predict when atmospheric conditions will be beneficial for sampling, campaigns should span at least two weeks. However, based on my experiences, I suggest four weeks or longer. Our observations show that roughly 50 % to 60 % of all samples will be invalidated during data analysis. Hence, it may be advisable to run the campaign for as long as it takes to acquire a good number of valid samples (10 to 15).

The campaigns conducted for this thesis covered the transition between winter and spring, future campaigns should (also by necessity of length of the campaign) start earlier in the heating season. Synoptic scale weather systems may prevent sampling the true background for several days, which should be taken into account when planning the length of the campaign.

Chapter 5

Historical winter CO-ratio record of Heidelberg station

Using continuously recorded $\Delta^{14}CO_2$, I investigate the effective[24] atmospheric $\Delta CO/\Delta ffCO_2$ emission ratio in Heidelberg over the past 20 years and compare its development to modelled $CO/ffCO_2$ emission ratios based on the TNO inventory and the atmospheric transport model STILT. Comparing measured effective atmospheric $\Delta CO/\Delta ffCO_2$ ratios to modelled $CO/ffCO_2$ emission ratios provided by TNO provides insight into the long-term compatibility of measurements and inventories. In general, the $\Delta CO/\Delta ffCO_2$ emission ratio is expected to decrease over time owing to the development of more efficient combustion processes. Differences between measured and modelled ratios point to an underestimation of CO emissions. This result is in accordance with the previous chapters about the measurement campaigns for traffic and heating, which suggest that CO emissions may be underestimated for these two sectors.

Heidelberg station. Heidelberg is one of few non-background measurement sites, that has a $\Delta^{14}CO_2$ record that reaches back into the 1980s. The Institute of Environmental Physics Heidelberg houses the laboratory for continuous measurements (CO_2, CO, and more), the integrated sample collection station, and the low level counting laboratory. The air intake is located 30 m agl on the roof of the institute. The integrated samples are used to determine average $\Delta^{14}CO_2$ during the integration time.

Background station. When analysing emissions via atmospheric trace gas concentrations, a suitable reference point, i.e. a background, has to be established against which all offsets are calculated ($\Delta CO = CO_{meas} - CO_{bg}$, $\Delta ffCO_2$ via Eq. (2.4)). Comparing model results to measurements requires a similar assumption for background concentrations. STILT has all concentrations set to zero outside its domain (that extends from 15° W to 35° E and from 33° N to 73° N), making maritime stations prime candidates. Maritime stations are also preferable, because influences of regional local sources can be excluded by sampling only when the

---

[24] 'Effective' in this case means that some time has passed since the emission(s) and atmospheric mixing and chemical processes – e.g. catalytic reactions in car exhaust systems – affecting the CO concentration lead to emission ratios that differ from the emission ratio directly after combustion.

wind blows from the sea. The prime candidate for this thesis is Mace Head (MHD), a maritime background station on the west coast of Ireland. Ten-day-back trajectory analysis[25] for the year 2020 by Fabian Maier (unpublished) showed that most air masses reaching Heidelberg enter the European domain in close vicinity to Mace Head, see Fig. C.1 (77 % of trajectories end at the western edge of the domain), consolidating that Mace Head is the optimal choice. Conceptually, choosing Mace Head as the background station means committing to the idealised view of the atmosphere, that there is a global background that is well described by Mace Head measurements. In comparison with other background stations (i.e. calculating ratios with respect to a different background station), I found that differences in CO_2 and $\Delta^{14}CO_2$ had a negligible impact, i.e. the assumption that MHD is representative of the global background holds. This is not the case for differences in CO. When CO concentrations at Mace Head (53° N) and Izaña (28° N, on Tenerife, Canary Islands) are compared, a strong latitudinal gradient is present in winter. I try to account for this by using Fabian Maier's trajectory data for 2020 (unpublished) to estimate a representativeness uncertainty (see Appendix C.3). Still, this may not account for air masses of continental origin. at the end of the chapter, I will discuss mean winter $\Delta CO/\Delta ffCO_2$ emission ratios. For each winter, roughly six to 12 integrated samples contribute to the mean, meaning multiple different background situations are averaged for every winter. Averaging over multiple integrated samples ameliorates the agreement between reality and our idealised view, since – according to Fabian Maier's trajectory data (unpublished) – most air actually does originate near Mace Head.

In short, Mace Head is not in all cases the optimal background station and even though I try to account for this, for some integrated samples the effective atmospheric $\Delta CO/\Delta ffCO_2$ emission ratio will be skewed. An estimation of the magnitude of this problem will be addressed in Section 5.3.

To model emission ratios, the TNO emission inventory is combined with the atmospheric transport model STILT to estimate CO and $ffCO_2$ enhancements in Heidelberg. Since the STILT model covers the whole European domain and has background concentrations at the edges set to zero, conceptually, both measured and modelled concentration enhancements both originate from emissions on the European continent and can be compared (if the aforementioned caveats of choosing MHD as the background station are accounted for).

I only analyse average winter ratios for two reasons. Firstly, $ffCO_2$ concentrations in summer are much lower due to an increased mixing height, leading to relative uncertainties of 50 % or more because the measurement uncertainty is fixed at circa 1 ppm $ffCO_2$. For small $ffCO_2$ concentrations, deviations of 50 % can double the

---

[25] 100 trajectories per hour were calculated. For atmospheric transport modelling, STILT was used with ECMWF meteorological data on a 0.25° by 0.25° resolution.

ΔCO/ΔffCO$_2$ emission ratio[26]. Secondly, CO is less stable in summer. Its lifetime depends on the production of OH, which is linked to O$_3$ production that depends on solar radiation. This is just one example for light-dependent chemical reaction chains that affect CO more strongly during the summer (other examples would be the oxidation of CH$_4$ and other hydrocarbons). Consequently, CO is of lower quality as a tracer for fossil fuel burning in summer and atmospheric chemistry models are necessary to fully understand atmospheric CO concentrations. This goes beyond the scope of this thesis and, hence, I confine my analysis to winter months December, January, and February.

5.1 Measured emission ratio data acquisition

In the following paragraphs, I describe the data used to calculate the emission ratios in Heidelberg. Data on Δ^{14}CO$_2$ and weekly flasks for CO and CO$_2$ are necessary for Heidelberg and the background station, Mace Head. Minor corrections to Δ^{14}CO$_2$ are necessary to account for biospheric influence and emissions from nuclear facilities, the corresponding data are also introduced. Additional information is given in Appendix C.

Background data signal processing. CO and CO$_2$ data for Mace Head were provided through the ObsPack framework (Schuldt et al., 2021b,a). Δ^{14}CO$_2$ data were provided by Samuel Hammer and are part of the ICOS network (public access: `doi:10.18160/CE2R-CC91`, does not cover all the data I used). Data smoothing was necessary because the background data (two-week integrated samples for Δ^{14}CO$_2$ and weekly flasks for CO and CO$_2$), especially Δ^{14}CO$_2$ data, were too noisy. The noise is the result of sampling and measurement processes that introduce uncertainties. Using an interpolation instead of smoothing the data would lead to overfitting. The data smoothing is founded in the physical understanding of processes affecting concentrations (a detailed explanation can be found in Appendix C) and avoids overfitting. The Carbon Cycle Greenhouse gases Curve fitting routines (CCGCRV, Carbon Cycle Greenhouse gases Curve Fitting Methods, 2022) developed by the National Oceanic and Atmospheric Administration (NOAA) were applied to all background data. The CCGCRV fitting routines are designed specifically for time series analyses of background concentrations. In essence, the time series is fitted with combination of a polynomial and a harmonic oscillation. Then, the residuals are Fourier-transformed into frequency space, a

---

[26] This is illustrated by the following example. Assuming a real ffCO$_2$ enhancement of 2 ppm and a real CO enhancement of 15 ppb with a measurement precision is of ±1 ppm for ffCO$_2$, we obtain a variation of the measured ratio between 5 ppb/ppm and 15 ppb/ppm where the real ratio is 7.5 ppb/ppm.

low-pass filter is applied (to remove unwanted high-frequency signals that are not representative for the overall trend), and the data is transformed back into time space. To cover the first two months of 2021, where no data is available yet, the CO and $\Delta^{14}CO_2$ records of Mace Head were extrapolated using the CCGCRV fit (without the residual analysis, since this requires data). The smoothed curves are show in Figs. C.3 to C.5 in Appendix C.

Heidelberg data. The Heidelberg data record is based on Gas Chromatographic analysis system (GC) recordings and cavity ring-down spectroscope (CRDS, Picarro G2401) measurements. CRDS measurements were processed by the ICOS Atmospheric Thematic Centre (ATC, Hazan et al., 2016). GC data were used until the end of 2018. In 2019, the CO quality check measurements of the GC showed irregularities, also confirmed by the comparison between GC and FTIR (same instrument as used in the traffic campaign) that showed good agreement for earlier years. As a consequence, the GC was shut down on the December 18, 2019. Fortunately, the Picarro instrument began its measurements early in the year 2018. To ensure continuity, I shifted the Picarro data by the mean offset between GC and Picarro in the overlap period 2018 ($\Delta CO_2 = -1.1$ ppm, $\Delta CO = 2.1$ ppb). With this step I aim to create a consistent and continuous data record, where the change of instruments affects the results as little as possible, i.e. no sudden jump in concentrations. This comes at the cost of modifying a well-calibrated data set. However, considering the relevant scales (CO offsets between MHD and Heidelberg at the order of 100 to 200 ppb, CO_2 concentrations of more than 400 ppm[27]), I argue that this is acceptable.

$^{14}CO_2$ nuclear correction. A minor correction is applied to the measured $\Delta^{14}CO_2$ to account for $^{14}CO_2^{nuc}$ emissions from nuclear facilities. Estimates are based on the Radioactive Discharges Database (RADD, annual emissions available for EU members) inventory emissions combined with atmospheric transport models. For January 2018 to February 2021 I use corrections provided by Maier et al. (2021), calculated with WRF-STILT. For 2000 to 2017, I use calculations by Ida Storm (unpublished) and Kuderer et al. (2018) (using HYSPLIT) for far-field and near-field emissions, respectively.

The Carbon Portal (2022) provides $\Delta^{14}CO_2^{nuc}$ contamination in Heidelberg calculated by Ida Storm (unpublished) with STILT. In STILT, all nuclear $^{14}CO_2$ emissions are released from the ground (surface source influence ansatz) by ignoring the actual emission stack heights. As Maier et al. (2021) showed, the surface source influence ansatz provides good results if point sources are more than 50 km from

---

[27] Consult Eq. (2.6) confirming the importance absolute concentrations as opposed to the offset between MHD and Heidelberg.

Heidelberg, i.e. in the far field. For the near field (closer than 50 km), a different approach was necessary, as will be discussed below. The Carbon Portal data cover the years 2006 to 2020. For the earlier years 2000 to 2005, the data were extrapolated. The detailed calculation can be found in Appendix C. Far-field and near-field contamination was addressed separately for the years 2000 to 2017. In short, for the far-field, I calculated an average dilution factor (i.e. how much of the far-field emissions reached Heidelberg) and multiplied it with the available far-field RADD emissions for each year[28] to extrapolate the ${}^{14}\mathrm{CO}_2{}^{\mathrm{nuc}}$ influence. This is a rather rough estimate of the nuclear $\Delta^{14}\mathrm{CO}_2$ far-field influence. However, making the estimates more precise, does not change the results, because the far-field nuclear influence is very small (on average 1 ‰), smaller than the uncertainty of $\Delta^{14}\mathrm{CO}_2$ measurements (2 ‰). Consequently, a rough estimation of far-field influence is sufficient.

In the near-field of Heidelberg, there are five facilities (Biblis, Karlsruhe, Obrigheim, Neckarwestheim, Philippsburg) where the surface source influence ansatz is not recommendable. Treating nearby point sources (i.e. stacks with typical emission heights of >100 m for nuclear facilities) as surface sources can result in too large estimates for the nuclear contamination at low-altitude measurement sites like Heidelberg (intake height of 30 m agl), especially during stable atmospheric conditions. Since only nighttime samples are analysed, predominantly collected during stable conditions, a different model approach is required. Kuderer et al. (2018) calculated nuclear $\Delta^{14}\mathrm{CO}_2$ emissions for the five closest facilities around Heidelberg for the years 1986 to 2015 using HYSPLIT with a particle dispersion forward run, using the correct stack height for emissions. I extrapolated Kuderer et al. (2018) results for 2016 and 2017 similar to the extrapolation for the far-field. The average dilution factor this time was based on the years 2012 to 2015, because in 2011, the nuclear power plant Philippsburg Block-I was shut down. This is also a rough, but reasonable estimate. $\Delta^{14}\mathrm{CO}_2$ from near-field nuclear facilities occasionally surpasses the measurement uncertainty. When Philippsburg Block-I was still running, the $\Delta^{14}\mathrm{CO}_2$ occasionally reached >10 ‰, but since the shutdown, near-field nuclear influence mostly falls below 2 ‰. Consequently, a rough estimation of near-field influence in 2016 and 2017 is sufficient. In closing, note that since RADD emissions are only available on a yearly basis, all extrapolated corrections also are constant over the year.

Generally speaking, after the shutdown of Philippsburg Block-I, the *total* nuclear correction for $\Delta^{14}\mathrm{CO}_2$ is smaller than 4.5 ‰ across all models/data sets. This is on the scale of the uncertainty of the measurement, roughly equivalent to $2\,\sigma$. It is a necessary correction, since otherwise the measurements are biased, but a rough

---

[28] RADD only provides annual emissions, but in reality, emissions are not distributed homogeneously in time (Varga et al., 2021).

extrapolation of near and far-field contamination (in years without modelling of such) suffices.

Biospheric CO_2. For the calculation of ffCO_2, $\Delta^{14}CO_2$ measurements have to be corrected for influence from the biospheric emissions, e.g. plant and soil respiration. Biospheric $\Delta^{14}CO_2$ was modelled by Naegler and Levin (2009a) (the mean of $\Delta^{14}CO_2$ HI and LO was used for calculations in this thesis). Samuel Hammer extended the calculations from Naegler and Levin (2009a) to the current year (Levin et al., 2011). Following Levin et al. (2008), I use Eq. (2.5), i.e. I assume that only half of the biogenic CO_2 originates from the heterotrophic respiration for which Naegler and Levin (2009a) calculated $\Delta^{14}CO_2^{het,bio}$.

Average winter $\Delta CO/\Delta ffCO_2$ emission ratios. The average winter $\Delta CO/\Delta ffCO_2$ ratios were calculated with a weighted total least squares regression, as described in Section 2.4. To be consistent with our idealised view of a global background well represented by Mace Head measurements, I fixed the intercept of the fit at zero, ensuring that the resulting ratio describes emissions in reference to Mace Head. An intercept $\neq 0$ is conceptually the same as changing the (CO) background. The resulting ΔCO, $\Delta ffCO_2$, and $\Delta CO/\Delta ffCO_2$ for Heidelberg are shown in Fig. 5.1. The left plot shows winter averages, the right plot shows each individual integrated night-time sample. Winters with higher density of lines have one-week integrated samples. Note that the winter average ratio is calculated according to the weighted total least squares regression, not by dividing the average ΔCO by the average $\Delta ffCO_2$.

5.2 Emission ratio modelling

TNO provides a high resolution (6 km × 6 km) Europe-wide emission inventory with yearly emissions and time profiles to increase the temporal resolution (cf. Section 2.3). The inventory is based on National Inventory Reports (NIR), for CO_2, CH_4, and other greenhouse gases. For pollutants like CO, NO_x, particulate matter, the Informative Inventory Reports (IIR) provides data for the inventory. NIRs and IIRs are submitted to the UNFCCC and publicly available. Emissions from the reports are disaggregated to the 6 km × 6 km grid based on proxies, e.g. population density or traffic volume. The heating campaigns (Chapter 4 showed that TNO proxies do not always correctly assign emissions to individual cells. This does not necessarily indicate flaws that affect the large scale distribution. Consistency was a large concern for TNO. Hence, the inventory was constructed such that emission sums of (sub)regions always add up to the emissions of the larger region. For instance, the sum of all cells in Germany reproduce the total

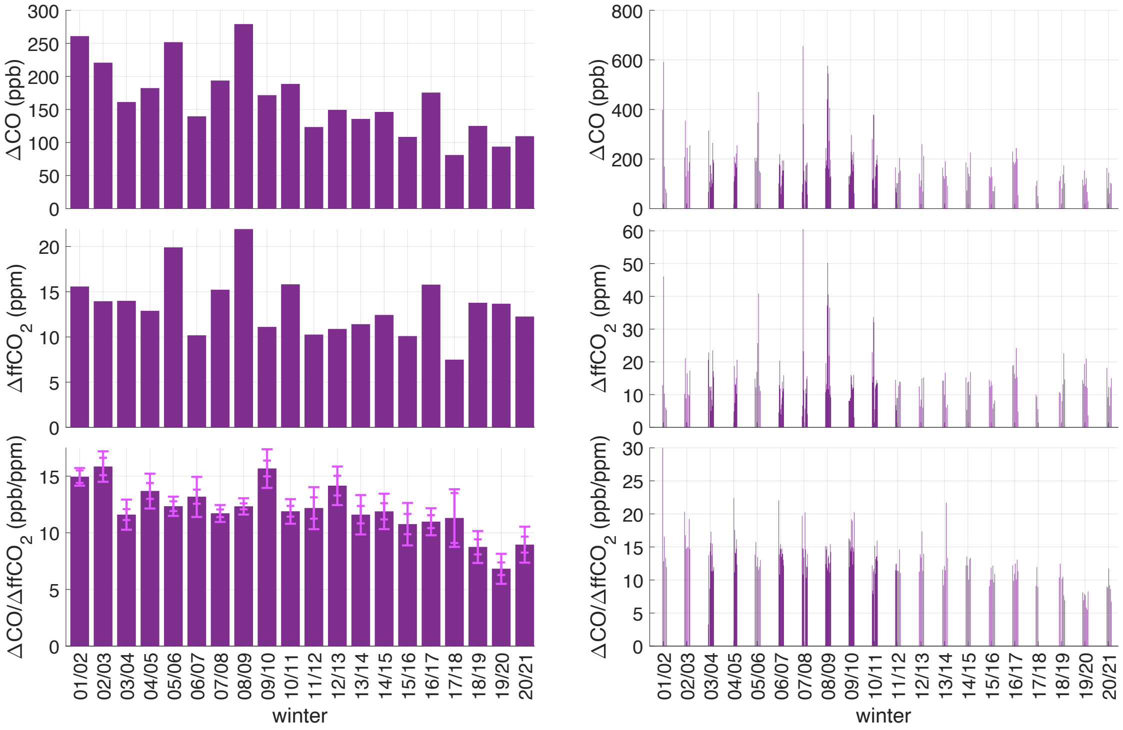

(a) Winter means.

(b) Integral night-time samples.

Fig. 5.1 ΔCO, $\Delta \mathrm{ffCO}_2$ and $\Delta \mathrm{CO}/\Delta \mathrm{ffCO}_2$ of the Heidelberg record with respect to MHD as background station. **(a)** Mean for every winter, **(b)** individual night-time samples. Note the different y-axis scales and that the ratio in the bottom panels is *not* the quotient of the two upper panels. Instead, it is calculated with the weighted total least squares regression method. Uncertainties are shown in pink. The smaller error bar corresponds to the regression fit parameter uncertainty, the larger error bar corresponds to the uncertainty in the CO background.

emissions for Germany. For the emission ratio modelling, The TNO inventory is folded with the surface flux influence maps (footprints) of STILT, weighting all emissions of continental Europe. Consequently, the correct large scale distribution is more important for the modelled total residential heating emissions than the local scale misassignment. The folding of the TNO inventory with the STILT footprints is flawed, as discussed before.

Recall the following two problems with calculations of modelled $\Delta \mathrm{CO}/\Delta \mathrm{ffCO}_2$ emission ratios. First, since I use two dimensional, monthly aggregated footprints provided by the Carbon Portal and fold them with the monthly emission maps of the TNO inventory (offline calculation), I am restricted to the surface source influence ansatz. Consequently, point source emissions in the near-field (50 km) around Heidelberg are overestimated. Second, due to the offline calculation, the sub-monthly variations in sources are misrepresented. In other words, there is no way to tell when the air passed which source – which may be important. For

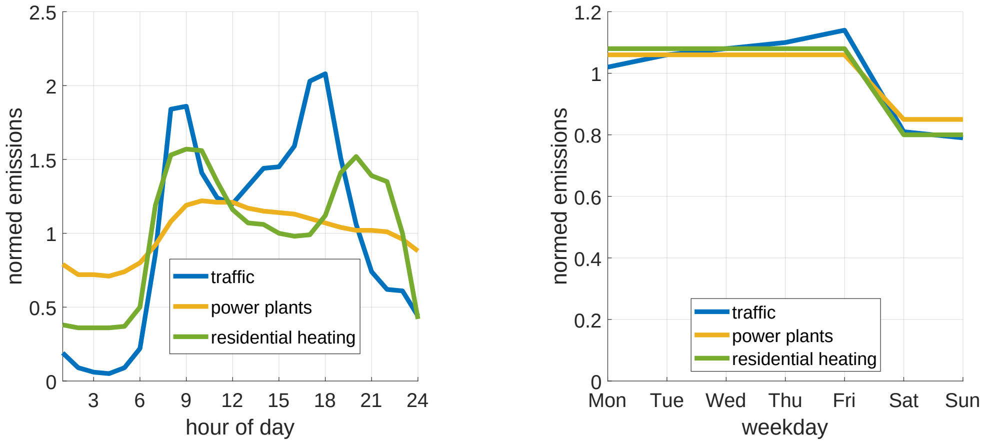

(a) Diurnal emission time profiles

(b) Weekly emission time profiles

Fig. 5.2 Sub-monthly time profiles for emissions in TNO. **(a)** Diurnal time profiles normalized to 24 hours, i.e. value of 1 is the average, **(b)** weekly time profiles normalized to seven days, i.e. value of 1 is the average.

instance, as explained for the heating campaign, the residential heating sector has its highest emissions in the evening and in the morning. So whether the air passed a residential area at 20:00 h or 1:00 h is crucial (Fig. 5.2a). The reduced emissions during the weekend do not affect the ratios as much, since all three major sectors show similar behaviours (Fig. 5.2b). Online calculations of concentrations that avoid these problems by folding emissions with 3-hourly footprints were beyond the scope of this thesis. Both problems will be addressed in the next section.

5.3 Results and discussion

As discussed above, there are three major points of contention when comparing measured and modelled emission ratios as shown in Fig. 5.3.

I. Offline folding of footprints and emission maps causes incorrect weighing of emissions because diurnal variations in source strength are ignored

II. Assumption of a global background that is well represented by measurements at MHD oversimplifies the background

III. Surface source influence ansatz overestimates near-field point source emissions

Fig. 5.3 shows winter (December, January, February) average ΔCO/ΔffCO$_2$ emission ratios and their trends. Modelled emission ratios, calculated from TNO inventory combined with STILT footprints, are shown in black and blue. The measured emission ratios are displayed in purple. Uncertainties for the modelled emission ratios are based on Super et al. (2019). In short, the total uncertainty of the modelled emission ratio for each winter is based on sector-specific relative uncertainties provided by Ingrid Super through personal communication, October 1, 2020. Detailed calculations can be found in Appendix C.4. Two uncertainty estimates for the measured ratios are shown in the plot. The smaller error bar indicates the uncertainty of the fit parameter of the weighted total least squares regression[29]. The larger error bars were determined by variation of the CO background (i.e. the intercept) by ±21 ppb corresponding to $3\,\sigma$ of the representativeness uncertainty (7 ppb, cf. Appendix C.3). The trend of the measured ΔCO/ΔffCO$_2$ emission ratios, shown as dashed and solid purple line, is practically the same, regardless of whether the winters before 2006/2007 are considered or not. The trend of the modelled ΔCO/ΔffCO$_2$ emission ratios is less negative than the trend of the measured emission ratios, no matter what corrections are applied. The corrections will be discussed shortly. In theory, it is straightforward to address point I through online folding of 3-hourly footprints with the emission inventory. However, practically, this goes beyond the scope of this thesis. Only data modelled by Maier et al. (2021) with WRF-STILT (surface source influence ansatz) for the winter 2018/2019, shown as a red × in Fig. 5.3, provides an indication of how large the difference in emission ratio is. I will come back to this below.

Point II is essentially addressed by the larger error bars of the measured data in Fig. 5.3. Using $3\,\sigma$ of the representativeness uncertainty corresponds to the range that almost certainly covers the misrepresentation of the CO background.

In order to address point III, I used data from a study of point source emissions by Maier et al. (2021) to calculate an average overestimation factor of 3.4 for the surface source influence ansatz compared to the volume source influence ansatz (Fig. C.6b). Reducing the point source emissions by a factor of 3.4 increases the modelled ΔCO/ΔffCO$_2$ emission ratio markedly, since point sources have low ΔCO/ΔffCO$_2$ emission ratios in general. This is visualised in Fig. 5.3: compare downward pointing triangles and upward pointing triangles. Note however, that this is a rather rough estimate, since assuming a constant factor of 3.4 is an oversimplification, both in space and time. Realistically, the factor depends on the distance from Heidelberg. The momentary planetary boundary layer (PBL) height also plays a major role in how much of the point source

---

[29] The regression plot for each winter can be found in Appendix D.

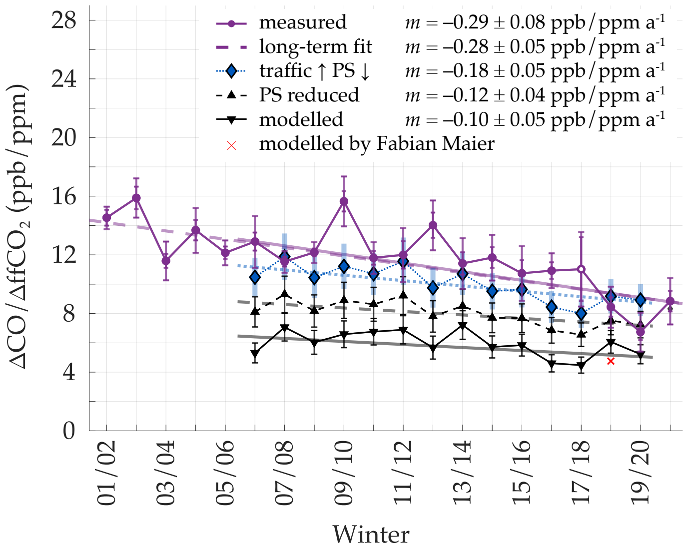

Fig. 5.3 Mean winter ΔCO/ΔffCO$_2$ ratios based on measurements (purple circles) and on inventory data (black triangles, blue diamonds). Three iterations of modelled ratios are shown. The ratios based on the unchanged TNO inventory are downward pointing triangles. The second iteration (upward pointing triangles) corresponds to reduced emissions from point sources in the surroundings of Heidelberg (8.0° to 9.4° E, 49.0° to 49.8° N) by a factor of 3.4 compensating for the shortcomings of the surface source influence ansatz of STILT. The third iteration (blue diamonds) has the same reduced point source emissions and, additionally, traffic emissions were increased according to the difference between inventory emission ratio and measured emission ratio for the highway traffic mix (80 % increase). Slopes of the linear trends are given in the figure legend. The measurement point for winter 2017/2018 is shown as an empty circle, because no integrated samples from January and February 2018 are available and, hence, the value is unreliable. Measured mean winter ratios have two error bars: the smaller one portraits the uncertainty of the weighted total least squares fit on which the mean is based, the larger one was determined by variation (±21 ppb) of the CO background. The trend of the measured ratios calculated based on two different time frames. The dashed purple line shows the trend for winters 2001/2001 until 2020/2021, while the solid purple line shows the trend for winters 2006/2007 and later.

emissions reach Heidelberg.[30] Hence, there is a time variation of the factor as well. Nevertheless, this still shows that the shortcomings of the surface source influence ansatz are partially responsible for the difference between measured and modelled ΔCO/ΔffCO$_2$ emission ratios. Since the traffic campaign (Chapter 3) showed that measured traffic ΔCO/ΔffCO$_2$ emission ratios were 80 % higher than modelled emission ratios, another iteration of modelled emission ratios is plotted in Fig. 5.3 as blue diamonds, where all traffic CO emissions (highway and all other road types) are increased by 80 %, and near-field point source emissions

---

[30] For instance if the nightly PBL height is close to or lower than the stack height of a point source, its emissions are not (fully) mixed into the PBL. STILT often overestimates the nightly PBL height, leading to a large overestimation of the night-time concentrations in Heidelberg.

were reduced in the same way as before. This closes the gap between measured and modelled $\Delta CO/\Delta ffCO_2$ emission ratios further. Note that CO emissions of the residential heating sector are not modified, in spite of the large discrepancy that the heating campaign in Leimen (Section 4.2) showed (factor 4.5). As I argue in Section 4.4, this discrepancy is the result of a sub-optimal proxy for heating emission disaggregation in TNO. This means the CO heating emissions cannot be corrected, since it is a challenging spatial distribution problem. However, for traffic, the case is different. TNO emission ratios for German highway traffic are nearly identical for the whole country. Small differences only arise for roads or highways that have a different traffic mix, e.g. more trucks. I therefore argue that the 80 % difference in $\Delta CO/\Delta ffCO_2$ emission ratio can be applied to all traffic (highway and all other road types) as an estimate for the required correction.

Even with the changes to near-field point source emissions and the traffic $\Delta CO/\Delta ffCO_2$ emission ratio, a small difference in trends between measurements and model remains. One possible explanation is that the traffic $\Delta CO/\Delta ffCO_2$ emission ratio has to be adjusted by a different factor each year. The traffic campaign showed an 80 % difference for the year 2021. It is possible that the difference was larger for earlier years. Modelled $\Delta CO/\Delta ffCO_2$ emission ratios depend on emission factors determined in test-bed environments and by portable emission measurement systems (PEMS). It is conceivable that with improvements in PEMS and other measurement techniques, emission factors get more realistic every year. The year-to-year changes (how the emission ratio of the previous compares to the emission ratio of the current year) are not the same when comparing modelled and measured emission ratios. The total emission ratios of TNO are steadily declining and only in combination with the footprints of STILT year-over-year ups and downs appear. Footprints differ from winter to winter. Hence, the source mix (i.e. how much each sector contributes) does, too, and with it the average $\Delta CO/\Delta ffCO_2$ emission ratio.

As point I states, there is a irreconcilable problem with using the monthly aggregated footprints, i.e. making offline calculations that essentially ignore source variations on time intervals smaller than a month. Consider the red × in Fig. 5.3. The WRF-STILT calculations that result in this point are based on the surface source influence ansatz. Hence, it must be compared to the downward pointing triangles on the solid line, showing the modelled ratios without any changes to the inventory. The online-calculated ratio is 22 % lower than the offline-calculated ratio. Using nightly footprints for the calculations (18:00 UTC to 6:00 UTC), may introduce a systematic bias between offline and online calculations, because for online calculations, the influence of the heating and the traffic sector are lower owing to the night-time low of emissions from both sectors. In order to quantify the extend of the problem, I calculated the night-time sector contributions and the total (i.e. emissions from all sectors combined) $\Delta CO/\Delta ffCO_2$ emission ratio. For power plants, industry, and residential heating, emissions are ≈ 80 % of the average whole-day emissions during night (18:00 UTC to 06:00 UTC). For traffic, the value is ≈ 50 % since evening hours still have large traffic contributions. These reductions are only applied to the surroundings of Heidelberg (8.0° to 9.4° E, 49.0° to 49.8° N). Conceptually this is equivalent to assuming that only near-field emissions are biased towards nightly emissions, while for the rest of the domain, there is no bias. That is, it is equivalent to assuming it is random whether a source adds its emission load to the air parcel during the night or the day and, consequently, ignoring the diurnal cycle and assuming a daily average is reasonable. The difference between full-day $\Delta CO/\Delta ffCO_2$ emission ratios and night-time $\Delta CO/\Delta ffCO_2$ emission ratios varies from 4 % to 9 %, decreasing almost monotonously over the years.

How can the decrease of the difference from year to year be explained? The diurnal profile of the total emissions is dominated by the traffic sector, because it has the largest variations over the day: close to zero emissions during the night and peaking emissions during rush hour. The difference between full-day and night-time $\Delta CO/\Delta ffCO_2$ emission ratios decreases, because, while the relative difference is ≈ 50 %, the absolute difference between night-time average and full-day average traffic CO emissions decreases as the $\Delta CO/\Delta ffCO_2$ emission ratio decreases. Fig. 2.6 shows this decrease in emission ratios.

In 2019, where the difference between the online calculations of Maier et al. (2021) and my offline calculations is 22 %, the difference according to my diurnal-profile calculations is only 5 %. In other words, while the diurnal-profile calculations suggest an average bias of less than 10 % between online and offline calculations (online < offline), the true magnitude of the bias is not calculated easily. Online calculations for all years are necessary to eliminate the problem. For the interpretation of Fig. 5.3, this means that all modelled emission ratios are overestimated and that, hence, the applied corrections are potentially insufficient to bring forth agreement between modelled and measured emission ratios.

5.4 Conclusion and perspectives

In summary, I studied the record of measured $\Delta CO/\Delta ffCO_2$ emission ratios for Heidelberg from winter 2001/2002 until winter 2020/2021 and compared this to modelled $CO/ffCO_2$ emission ratios (TNO inventory emissions combined STILT atmospheric transport) for the winters from 2006/2007 until 2019/2020.

Modelled and measured emission ratios agree within error margins for most years when the model is corrected for (1) overestimation of near-field point source emissions and (2) erroneously low CO emissions from traffic. However, modelled emission ratios have a positive bias of unknown magnitude because diurnal time profiles are disregarded by the offline folding of inventory and footprints. Hence, the true agreement is slightly worse than it appears in Fig. 5.3. Measured emission ratios show a faster year-over-year decline (-0.29 ± 0.08 (ppb/ppm)/year) than modelled emission ratios (-0.18 ± 0.05 (ppb/ppm)/year). The corrections applied to the modelled emission ratios are estimates. Refining them may already ameliorate the agreement between trends. The aforementioned bias can vary from year to year and, thus, affect the trend of the modelled emission ratios, too. Traffic CO emission corrections, necessary for a better agreement between measurements and model, calls for an investigation of the problem on the side of inventory and traffic-emission-model specialists. This is the main result of this thesis: using the results from the highway traffic campaign, I am able to explain the difference between model and measurement in the long-term record. This leads to a more precise CO emission ratio for the traffic sector. While finding discrepancies between measured and modelled emission ratios is the accomplished goal of this thesis, the results consequentially also lead to better traffic emission ratios and more precise $ffCO_2$ estimates for the traffic sector.

Chapter 6

Conclusions and perspectives

Three measurement campaigns were conducted for this thesis, investigating highway traffic and residential heating emissions. I used two mobile laboratories equipped with ten meter tall masts to get as close as possible to the emitters while still maintaining enough distance to get a mix from different sources of the same sector, not just one.

The thus determined sector-dominated effective atmospheric emission ratios were compared to modelled emission ratios based on the TNO inventory. For heating, the two different campaigns compared very differently to the corresponding TNO emission ratios. For Leimen, CO emissions from residential heating was underestimated by TNO, while for Gaiberg, the agreement was good. The most likely explanation is, that the TNO proxy used for bio-fuel burning in the residential heating sector mischaracterises Leimen as a rather urban residential area, when its heating systems are using nearly as much bio-fuel as the rural Gaiberg residential area.

Using mobile laboratories is a new method to determine emission ratios. No similar approach to measure residential heating emissions is found in the literature. The results shed light on the problem of spatial disaggregation of bio-fuelled heating emissions. It is challenging to solve this problem using mobile laboratories, because that requires measurement campaigns in virtually every city or town. With the technology described in this thesis, this is an insurmountable task. If instruments were available that could run without intermediate calibrations at sufficient precision and if $\Delta\mathrm{ffCO_2}$ (or $\Delta^{14}\mathrm{CO_2}$) could be determined in a simpler way, the task would no longer be insurmountable, but still inefficient. Instead using the presented method this way, one could target specific towns close to points-of-interest (e.g. measurement stations) that may be affected by emissions from residential heating and improve model estimates that way.

The traffic campaign revealed that TNO underestimates the average traffic CO emissions, i.e. the $\Delta\mathrm{CO}/\Delta\mathrm{ffCO_2}$ emission ratio of the traffic mix is 80 % too low. Traffic emission ratios have been measured in many ways, every method with its advantages and disadvantages. E.g., the method described here was difficult to set up (in part due to the required power supply), but is still less confined than tunnel studies and could be applied to virtually any road type. In the literature, fleet composition is at best mentioned as metadata. I was able to incorporate the fleet composition into my results, showing that it is of utmost importance, e.g. to compare measured emission ratios between studies. Models can benefit from this, if the diurnal time profile for the traffic sector accounts for differences in fleet composition.

I evaluated the long-term trend of the measured $\Delta CO/\Delta ffCO_2$ emission ratio in Heidelberg and compared this to the modelled CO emission ratio (based on TNO and STILT). Modelled and measured ratios only agree if (1) the overestimation of point source emissions close to Heidelberg due to shortcomings in the atmospheric transport model is compensated and (2) CO emissions are increased in accordance with the results of the highway traffic campaign. Even with the two corrections, the measurements still show a faster decline of the CO emission ratio.

The goal of this thesis is to better our understanding of proxy/$ffCO_2$ emission ratios. The focus lay on CO as a proxy, because NOx is not as widely used and has no decade-long record that can be studied. Both the highway traffic campaign results themselves and also these campaign results in conjunction with the long-term trend point towards an underestimation of CO emissions from the traffic sector in Germany. This warrants further study. The experimental data is convincing, so it falls to experts in traffic modelling to investigate the discrepancy and, if necessary, adjust models.

Appendix A

Instrument specifications

The following sections describe basic working principles, calibration schemes, and accompanying literature for all instruments used for the present thesis. In particular, it covers trace gas measurements and flask processing.

A.1 Trace gas measurements

To reach the required accuracy for the trace gas measurements, we use up to three gas cylinders for calibration and at least one gas cylinder as an independent quality control, also denoted target.

A.1.1 Main mobile laboratory

The main mobile laboratory (ML1) first used a Picarro G2301 cavity ring down spectrometer (CDRS) for CO_2, CH_4 measurements, in conjunction with an AEROLASER CO-analyser for CO measurements. Later, a Picarro G2401 instrument was installed, replacing the Picarro G2301 and the AEROLASER. For NO_x measurements, a Iterative Cavity Enhanced Differential Optical Absorption Spectrometer (ICAD) manufactured by airyx is used. Additionally, ML1 uses a Rn-monitor to detect ^{222}Rn indirectly.

Picarro G2301 and G2401. Two cavity ring down spectrometers (CDRS) were used in the campaigns. A Picarro G2301, provided by Environment and Climate Change Canada[31], capable of measuring CO_2 and CH_4 (in conjunction with an AEROLASER L5001 for CO). The G2301 seized services during the campaigns and was by a Picarro G2401, provided by the Laboratoire des sciences du climat et de l'environnement, LSCE[32]. Cavity ring down spectroscopy (Cavity Ring-Down Spectroscopy, 2022) uses a cavity with near-perfectly reflecting mirrors (99.999 %

---

[31] Special thanks to Lauriant Giroux, Doug Worthy, Senen Racki, and Felix Vogel.

[32] Special thanks to Olivier Laurent.

Table A.1
Calibration cylinders for all instruments (Picarro, Aerolaser) in ML1. Gas concentrations for UHEI tanks provided by ICOS FCL. Concentrations for PIC4_3 provided through measurements by Picarro instrument in our laboratory.

Tank	FSN	UCN	Function	CO_2 (ppm)	CO (ppb)	CH_4 (ppb)	N_2O (ppb)
UHEI30	i20200193	D810583	standard low	400.31	95.89	2008.41	320.82
UHEI32	i20200194	D810585	target	553.18	560.82	2403.75	334.04
UHEI34	i20200196	D810587	standard medium	499.61	369.20	2206.73	326.22
UHEI36	i20200195	D810589	standard high	714.47	976.67	2815.85	342.24
PIC4_3	–	–	Aerolaser calibration	490.12	450.85	2203.02	–

according to Picarro). A laser operates until a threshold of intensity is reached. It is then shut off and a photo detector measures the decrease of intensity over time (‘ring down’) that is caused by the imperfect reflection of the mirrors. If an absorbing gas is present, the ring down time is shorter, since light intensity is now additionally absorbed by the gas. For additional details, the interested reader can refer to Busch and Busch (1999).

Aerolaser L5001. Since the Picarro G2301 cannot measure CO, we additionally employed an Aerolaser L5001 for this purpose. The Aerolaser L5001 measurements rely on resonance fluorescence. That is, atmospheric CO is excited by optically filtered radiation from a CO resonance lamp (Gerbig et al., 1996). To ameliorate precision, Gerbig et al. (1996) flushed the optical filter with N_2 to reduce the influence of O_2, which absorbs in the same spectral region as CO, and operated the resonance lamp with a mixture of 99.75 % Ar and 0.25 % CO_2, which yields the optimum sensitivity. Further details can be found in Gerbig et al. (1996). We used an old version of the instrument that is no longer produced and ultimately failed during the traffic campaign. It was replaced by the aforementioned Picarro G2401, that is capable of measuring CO_2, CH_4, and CO.

Table A.1 shows the gas concentrations for the cylinder used in ML1. Note that the CO concentration of PIC4_3 was initially erroneously assigned as 447.79 ppb. This only became clear after all campaigns, when the cylinder was once again measured at the Picarro G2401 instrument in our laboratory. The value in the table was reconstructed by re-evaluating measurements from before the campaigns with help of Amara Abbaris of the Atmospheric Thematic Centre (ATC). Because I did not solely rely on the internal calibration, which was done with CO = 447.79 ppb, but also corrected the Aerolaser L5001 data with the measurements of the calibration tanks, the effect of this erroneous assignment was minimal.

Rn-monitor. ^{222}Rn is a tracer for atmospheric transport due to its rather constant, homogeneous exhalation rate from the soil (Dorr and Munnich, 1990). The Rn-monitor used in the main mobile laboratory (ML1) was provided by Ingeborg Levin, its functionality is described in Levin et al. (2002). Instead of measuring ^{222}Rn directly, the Rn-monitor exploits its daughter elements ^{218}Po and ^{214}Po that attach to aerosols. The aerosols are caught on a filter and their α-decay is measured by an α-detector. Assuming ^{222}Rn and its daughter elements are close to radioactive equilibrium, ^{222}Rn concentrations can be inferred from ^{218}Po and ^{214}Po if the disequilibrium factor (^{214}Po/^{222}Rn) is known (Levin et al., 2002).

Iterative Cavity Enhanced Differential Optical Absorption Spectrometer. For NO_x measurements, an Iterative Cavity Enhanced Differential Optical Absorption Spectrometer (ICAD) was installed in the main mobile laboratory (ML1). The measurement technique is described by Horbanski et al. (2019) and is based on differential optical absorption spectroscopy (Platt et al., 1979, 2009). The following description is based on Platt et al. (1979, 2009); Horbanski et al. (2019) as well as Juchem (2021). I simplified the equations to refer to a single absorbing gas, because this paragraph is only meant to instruct the reader in the basic principles behind the ICAD instruments.

Absorption spectroscopy is based on Lambert–Beer's Law:

$$I = I_0 \exp\left(-\epsilon L\right), \tag{A.1}$$

were I is the reduced intensity of light after passing a medium of length L with an extinction coefficient ϵ. I_0 is the original light intensity. In general, I_0, I, and ϵ are wavelength dependent. The concentration c of an absorbing gas relates to ϵ via the cross section σ:

$$c = \frac{\epsilon}{\sigma}. \tag{A.2}$$

Defining the optical density D as

$$D := \ln\left(\frac{I_0}{I}\right), \tag{A.3}$$

Lambert–Beer's Law can be written as

$$c = \frac{D}{\sigma L}. \tag{A.4}$$

Determining I_0 precisely is challenging because light source intensity, temperature, and pressure variations. Differential optical absorption spectroscopy (DOAS) circumvents the problem of knowing I_0 by (1) using reference spectra ($I_0 = I_{\mathrm{ref}}$) and (2) splitting the cross section σ into a broad-band part (σ_{b}) and a narrow-band part (σ_n), i.e. $\sigma = \sigma_\mathrm{b} + \sigma_\mathrm{n}$. With this and Lambert–Beer's Law, we can write the optical density as

$$D = \ln\left(\frac{I_\mathrm{ref}}{I}\right) = cL\sigma_\mathrm{b} + cL\sigma_\mathrm{n} + \sum_k \beta_k \lambda^k. \qquad \text{(A.5)}$$

$\sum_k \beta_k \lambda^k$ is a polynomial that includes Rayleigh and Mie scattering, light (source) variability, and light attenuation. The broad-band features of a spectrum can be included in the polynomial. The optical density (for one absorbing gas) can then be written as

$$D = \sigma_\mathrm{n} a + \sum_k \beta_k \lambda^k, \qquad \text{(A.6)}$$

where a is the fit parameter of the narrow-band. By doing so, any changes in the broad-band structure (due to changes in temperature, pressure, light source intensity) are 'absorbed' in the polynomial. Since the polynomial does not depend on σ, the concentration reads

$$c = \frac{D}{\sigma_\mathrm{n} L} = \frac{a}{L}. \qquad \text{(A.7)}$$

Further details can be found in Horbanski et al. (2019), but go beyond the scope of this thesis. Broadly speaking, some correction factors are necessary, e.g. an effective path length L_eff is introduced to account for the reduction of the real path length L due to absorption in the optical resonator. The Iterative CAvity enhanced DOAS (ICAD) instruments used for NO_x measurements in this thesis employ an iterative algorithm to optimise the L_eff. ICAD instruments do not require periodic calibration with gases of known concentration like other in-situ instruments, thanks to the DOAS method with its already calibrated reference spectra.

A.1.2 Background mobile laboratory

The background mobile laboratory (ML2), too, uses an ICAD instrument as described above for NO_x measurements. Furthermore it uses a Fourier-transform infrared spectrometer (FTIR) to measure CO_2, CO, CH_4 and other gases and isotopes that are irrelevant for this thesis.

Fourier-transform infrared spectrometer. The Fourier-transform infrared spectrometer (FTIR) used in ML2 was manufactured by the University of Wollongong[33] and is described in Hammer et al. (2013). The following information is an excerpt of Hammer et al. (2013):

---

[33] Contact person for the software is David Griffith (`griffith@uow.edu.au`).

> The instrument consists of an interferometer and a 3.5 l cell in a temperature-controlled box, permanently flushed with N_2 (5.0). The interferometer has a moving mirror which allows for scanning through a broad spectrum of wavelengths. The resulting interferogram is then Fourier-transformed (hence the name), yielding an absorption spectrum. The main advantage of an FTIR spectrometer is the broadness of the scanned spectrum. Most spectrometers are tuned for a narrow light frequency (laser) and few gas species of interest. An FTIR spectrometer measures all gas species at once and can even discriminated isotopologues like $\Delta^{13}CO_2$. The temporal resolution is 3 min, with 2.5 min of spectra collection and 0.5 min of online analysis. At flow rates of 1 l/min, 3 min is also roughly enough time to completely exchange the gas in the measurement cell. (Hammer et al. (2013))

For calibration purposes, the three gas cylinders described in Table A.2 (calibrated by the ICOS FCL in Jena) are connected to the FTIR and measured once a week. A MATLAB-based GUI is used to flag the data and to apply the calibration provided by the three standard cylinders. An independent quality check is provided by measuring target cylinders (Table A.3), one at a time. Because the FTIR requires more gas due to its large measurement cell, I had to use multiple target cylinders.

Heidelberg station laboratory. In the laboratory of our group at the Institute for Environmental Physics in Heidelberg, currently the aforementioned FTIR instrument and a CRDS instrument (Picarro G2401) are used to measure trace gases like CO_2, CO and CH_4 continuously. Previously, until December 2019, an additional gas chromatographic system (GC) was running in the laboratory. I performed the data quality checks and calibrations for the FTIR instrument. For the CRDS instrument, Julian Della Coletta of our group performed quality checks, while the rest of the data processing is handled by the ICOS Atmosphere Thematic Centre, ATC (Hazan et al., 2016). Recent, fully processed data from the Picarro G2401 can be found here: Heidelberg ATC panel (2022). Before its shutdown, the GC provided quasi-continuous measurements for more than 20 years. A detailed description of the instrument is given by Hammer et al. (2008). The system is

Table A.2
Calibration cylinders for FTIR in ML2. Gas concentrations provided by ICOS FCL.

Tank	FSN	UCN	Function	CO_2 (ppm)	CO (ppb)	CH_4 (ppb)	N_2O (ppb)
UHEI31	i20200197	D810584	standard low	401.32	96.77	2008.68	320.96
UHEI33	i20200198	D810586	standard medium	553.61	559.52	2388.01	334.10
UHEI35	i20200199	D810588	standard high	715.42	963.91	2835.30	342.43

Table A.3
Target cylinders for FTIR in ML2. Gas concentrations for UHEI37 provided by ICOS FCL and for N146 and PIC4_3 by CRDS instrument in IUP laboratory.

Use time	Tank	FSN	UCN	CO_2 (ppm)	CO (ppb)	CH_4 (ppb)	N_2O (ppb)
Sep 21 to Nov 3, 2020	N146_6	–	–	423.23	185.02	2028.74	–
Nov 3 to Dec 11, 2020	UHEI37	i20200200	D810590	499.74	370.30	2212.51	326.44
Dec 30, 2020 to Feb 2, 2021	N146_7	–	–	436.56	261.87	2060.63	–
Feb 26 to Mar 5, 2021	PIC4_3	–	–	490.12	450.85	2203.02	–

equipped with three detectors: (1) a Flame Ionisation Detector (FID) for CO_2 and CH_4, (2) an Electron Capture Detector (ECD) for N_2O and SF_6, and (3) a Reduction Gas (HgO) Detector for the measurement of CO and H_2.

A.2 Flask processing

Air samples for $\Delta^{14}CO_2$ measurements are collected in so-called flasks. Flasks are glass cylinders with a volume of 3 l and two ports. The collection with so-called flask samplers is fully automated. Measurements of CO_2, CO, CH_4, and other trace gases (but not NO_x) in flask samples are conducted in the ICOS Flask and Calibration Laboratory (FCL) in Jena in order to standardise the procedure. Then, $\Delta^{14}CO_2$ measurements are conducted in the ICOS Central Radiocarbon Laboratory (CRL) in Heidelberg, also following a standardised procedure. Measurements in Jena always come first, since all available CO_2 has to be extracted for $\Delta^{14}CO_2$ measurements.

A.2.1 Flask samplers

The ICOS FCL in Jena developed and provides flask samplers for ICOS stations. One such ICOS flask sampler was used in the main mobile laboratory (ML1). The CRL in Heidelberg developed its own independent flask sampler for a two-station approach measurement campaign (Freinsheim–Heidelberg) within the 'Research Infrastructures: Needs, Gaps and Overlaps' Project (RINGO, 2022; Rieß, 2019; Kneuer, 2020). After this campaign, the sampler was installed in the background mobile laboratory (ML2).

ICOS flask sampler. A manual for the ICOS flask sampler is available here: ICOS Flask Sampler (2022). The manual for the accompanying air dryer can be found here: air dryer (2022). The functionality of the sampler is described in Levin et al. (2020) and the rest of the paragraph follows this manuscript. Different sampling methods were tested by Maier (2018) but are not discussed here.

The sampler version used for the campaigns can hold up to 12 flasks at a time. The air passes through the ICOS air dryer before collection. The ICOS air dryer consists of two cryogenic water traps. Air flows through glass structures that are submerged in a silicon oil cooled to −40 °C. Water in the air freezes on the glass walls. To ensure seamless operation, a second water trap of the same kind is used when the first either freezes shut or after 12 hours (mode can be chosen by user). After the switch from one trap to another, the silicon oil in the 'full' trap is heated, melting the ice and ejecting the water through a dedicated outlet. This back-and-forth can go on for 20 days (or 500 working hours) or more before the oil has to be purged of water originating from condensation of laboratory air or seeping through tiny crevices. The then-dry air is filled into the flasks (one at a time) according to the 1/t filling approach. This requires permanent flushing of the flask and continuously decreasing the flow-rate by 1/t to capture the 'real' average hourly ambient air concentrations. In theory, the starting flow rate would have to be quasi infinite, in reality the maximum flow rate is 2 L/min. To compensate, the flask is flushed for 30 min prior to sampling, so that initial concentrations in the flask are already at the level of ambient air. However, this only works if concentrations are stable. Hence, for large ambient air concentration variations, the agreement between flasks and in-situ means deteriorates.

Heidelberg flask sampler. The setup of the Heidelberg flask sampler is described in Rieß (2019). It can hold up to 12 flasks at a time. Air is dried by a combination of a Nafion (counter flow drying) and a $Mg(ClO_4)_2$-filled cylinder (chemical drying). Sampling times can be dictated in the LabView interface. 55 min before the indicated time, the flask is evacuated for 25 min, then flushed with air for 10 min, then evacuated again for 20 min. This way, contamination by previous fillings is minimised. At the indicated time and the following 60 min, the flask is filled at a constant flow of 95 ml/min up to a pressure of 1.9 bar. Filling at a constant flow means concentrations at each point in time are weighted the same. That is, agreement between mean hourly ambient air concentrations and the flasks should be excellent.

A.2.2 Flask measurements

The ICOS Central Analytical Laboratories (CAL) are the institutions responsible for flask measurements. In Jena, the Flask and Calibration Laboratory (FCL) measures many trace gases including but not limited to CO_2, CO, CH_4, and N_2O. The Central Radiocarbon Laboratory (CRL) in Heidelberg specialises in $^{14}CO_2$ and $^{13}CO_2$ measurements.

ICOS Flask and Calibration Laboratory Jena. The ICOS FCL is responsible for calibration reference gases and flask measurements. Consequently, excellent the precision is required. The most recent quality control report can be found here: Jordan and Schumacher (2022). Flask samples are measured with a gas chromatographic analysis system (GC) equipped with three different detectors to detect CO_2 and CH_4 (both flame ionisation detector), CO (reduction gas detector), and N_2O (electron capture detector). The working principle can be found in the literature, e.g. Grob and Barry (2004) and is described briefly by Helmenstine (2021). In essence, gas chromatography relies on the interaction of the gas in question with a liquid phase. The main element of a GC is the column: a heated, long tube coated with a thin layer of a liquid, the so-called stationary phase. Air is injected into the column alongside an inert carrier gas. As the gaseous mix (mobile phase) moves along the column, different gas species interact with the stationary phase, the strength of the interaction depends on physical and chemical properties of the gas species (e.g. polarity of the molecule). The weaker the interaction, the faster the gas species moves through the column. Ideally, all gas species are completely separated. The chromatogram of the detector(s) then shows multiple separate peaks. Peak positions depend on the gas species (i.e. how fast it reached the detector) while peak areas depends on the concentration of the gas species. To calibrate, one measures chromatograms of calibration cylinders (where gas concentrations are known) to identify peaks and correlate peak area to concentration.

ICOS Central Radiocarbon Laboratory. The ICOS CRL is best described here: ICOS CRL (2022). The description there is as follows:

> The Central Radiocarbon Laboratory (CRL) is one of the Central Analytical Laboratories of ICOS Research Infrastructure. It is affiliated to the Institute of Environmental Physics of Heidelberg University.
>
> The ICOS-CRL builds upon the former Heidelberg Radiocarbon (^{14}C) laboratory, which was operated for more than 50 years by the Heidelberg Academy of Sciences and the Institute of Environmental Physics of Heidelberg University. The Heidelberg Radiocarbon laboratory gained international recognition in many scientific fields exploiting radiocarbon, such as groundwater dating, oceanography, tree ring analysis as well as atmospheric and carbon cycle research. The main

> task of the ICOS CRL is high precision analysis of CO_2 samples from the ICOS atmospheric station network.
>
> The analytical technique of the Heidelberg ^{14}C-laboratory was originally based on high precision proportional gas counting. The ICOS-CRL will continue using this conventional counting technique to allow for a smooth transition to state-of-the-art Accelerator Mass Spectrometry (AMS) radiocarbon analysis and provide a solid link to the historic data sets. ICOS-CRL operates up to 19 proportional gas counters, which are located in an underground laboratory, specially shielded against cosmic radiation. The analytical capacity of these counters is 500 unknown samples per year at precision of 2 ‰ or better. The majority of the atmospheric air samples from the ICOS RI atmospheric station network will however be analyzed by AMS. For both analytical techniques we developed optimized CO_2 extraction and processing methods and built the respective semi-automated processing lines in house. The AMS ^{14}C analyses are currently performed at the CEZA laboratory in Mannheim. One important aim is to maintain a long-term compatibility of both analytical techniques of better than 1 ‰.
>
> Apart from the analytical challenge of making accurate and precise atmospheric $^{14}CO_2$ measurements, the ICOS-CRL operates an urban atmospheric measurement station in order to test and implement new methods for atmospheric fossil fuel CO_2 ($ffCO_2$) quantification. New surrogate tracers or sampling strategies are tested here before they are implemented in the ICOS RI atmospheric station network. (ICOS CRL (2022))

A detailed description of the extraction and graphitisation line is described in Lux (2018). The functionality of AMS is described in Beta Analytic Inc. (2014). The low level counting method is described in Kromer and Münnich (1992). A comparison between low-level counting and AMS measurements is described in Hammer et al. (2017).

Appendix B

Traffic campaign quality control

As discussed in Chapter 3, continuous data were used to calculate emission ratios for the traffic campaign. This requires special care when it comes to data validity and quality. In the following bias and uncertainty estimates are elaborated.

Based on target cylinder measurements, I apply a H_2O correction to the FTIR CO_2 measurements and discuss their inadequacy for bias and uncertainty estimation, although normally used for this purpose. Using a side-by-side comparison of the two mobile laboratories, a second possibility for the estimation of bias and uncertainty is discussed, including its shortcomings. Finally, I show that comparisons between in-situ measurements and flasks are most suited to estimate the bias and uncertainty in the present case.

Tables B.1 and B.2 provide an overview of the biases and uncertainties that will be addressed in this section. The calculation of values displayed in the bottom of Table B.2 will be explained throughout the following sections and are linked to (1) Figs. B.10 and B.11 for column in-situ/flask, (2) Figs. B.5 and B.6 for column in-situ/in-situ, and (3) Figs. B.7 and B.8 for column flask/flask.

Table B.1
Instrument uncertainties associated with measurements of target cylinders of known gas compositions. The instruments are a CRDS Picarro G2401 instrument (ML1) and a FTIR (ML2). Multiple target cylinders were measured at the FTIR with varying offsets, thus only a rough range of deviations is given.

	Value (targets)	
	δCO_2 (ppm)	δCO (ppb)
ML1	0.00±0.03	1.23 ± 0.41
ML2	±0.20	±2

Table B.2
Uncertainty sources during traffic campaign. Cells with yes/no refer to whether the uncertainty is relevant to measurement type named at the top of the column. For each ML the internal quality control is the comparison between in-situ measurements and flasks. For the side-by-side comparison (Appendix B.2), in-situ measurements of both laboratories (column in-situ/in-situ, ML1 minus ML2) are compared, as well as flasks of both laboratories (column flask/flask, ML1 minus ML2).

Uncertainty source		In-situ/flask	Side-by-side	
			In-situ/in-situ	Flask/flask
Instrument uncertainty	ML1	yes	yes	no
	ML2			
Air-mass inhomogeneity	ML1	no	yes	yes
	ML2			
Asynchronicity	ML1	no	yes	yes
	ML2			
Different flask sampling methods	ML1	no	no	yes
	ML2			
δCO_2 (ppm)	ML1	−0.04 ± 0.48	0.47 ± 0.52	0.65 ± 0.56
	ML2	−0.15 ± 0.51		
δCO (ppb)	ML1	−2.96 ± 5.11	−2.78 ± 2.00	1.55 ± 2.20
	ML2	−2.11 ± 2.85		

B.1 Targets and FTIR H_2O correction

This section first considers the Picarro G2401 target cylinder measurements, then H_2O for the FTIR and the FTIR target cylinder measurements.

Picarro G2401. All cylinders attached to the Picarro G2401 are listed in table A.1. The measurements of the target cylinder are shown in Fig. B.1. The discrepancy in CO_2 and CO is very small at −0.03 ± 0.01 ppm and −0.46 ± 0.44 ppb, respectively. Taking the mean over the period of the side-by-side comparison does not change the CO_2 value, while the CO value worsens to −1.23 ± 0.21 ppb. As discussed above, target cylinder measurements will not be used for the final bias estimation, but they give a frame of reference.

FTIR. The four target cylinders used for the FTIR are shown in Fig. B.2. Meta data show that an increase in H_2O caused the jump in the CO_2 concentration of cylinder N146_7 (yellow), see Fig. B.3. This raised concerns for data measured starting December 2020, where H_2O concentrations increased above the limit of 8 ppm

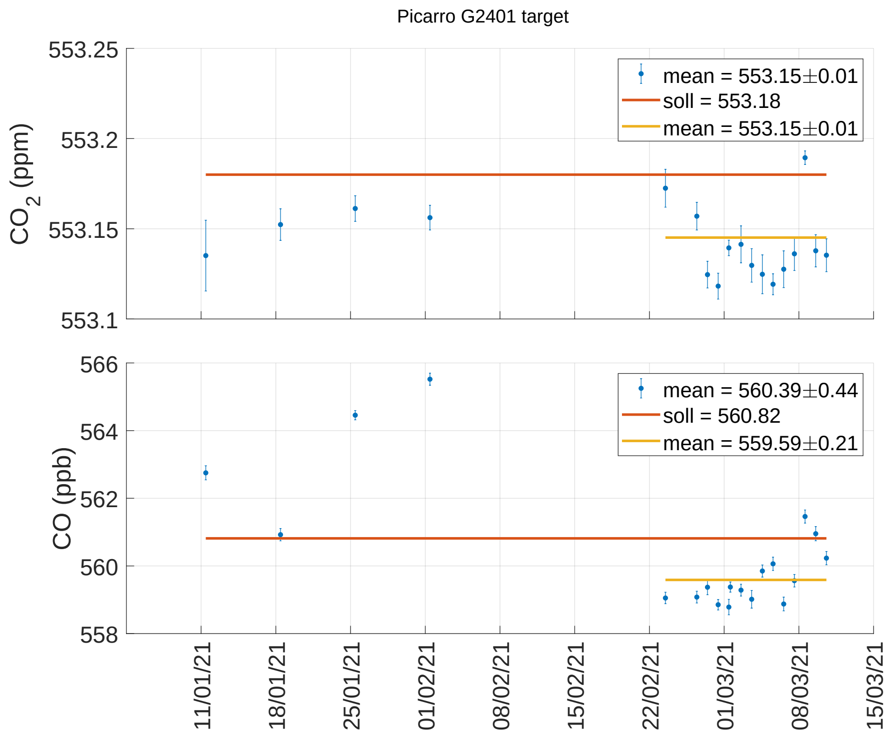

Fig. B.1 Target cylinder measurements of Picarro G2401. Reference values (labelled 'soll') are plotted as red horizontal lines. During the side-by-side comparison (shown as an orange horizontal line), the frequency of target measurements were increased. Generally speaking, the measurements fit the theoretical values well.

set by Hammer et al. (2013). Figure B.3 indicates that H_2O concentrations above 10 ppm change the CO_2 concentration markedly (even leading to a continuous offset after one large jump, indicating a hysteresis effect). At levels of more than 12.5 ppm H_2O, CO concentrations are affected as well. Consequently, I discard all FTIR data with H_2O concentrations above 10 ppm. Any CO_2 FTIR data above 5 ppm H_2O and before January 15, 2021 (i.e. before the jump in H_2O and CO_2 concentration) will be assigned an additional uncertainty of ±0.25 ppm. 0.25 ppm this is roughly the increase of the CO_2 concentration of cylinder N146_7 during the two-week long period after the jump in H_2O. Because we can track the changes in CO_2 concentrations after January 15, 2021 with the target cylinder N146_7 and because an increase in H_2O can only increase CO_2 concentrations, for that period a bias correction of −0.22 ppm is applied and the additional uncertainty of ±0.25 ppm is also assigned.

For the side-by-side comparison, no H_2O correction is applied. Between the end of the traffic campaign and the side-by-side comparison, the set-up was turned

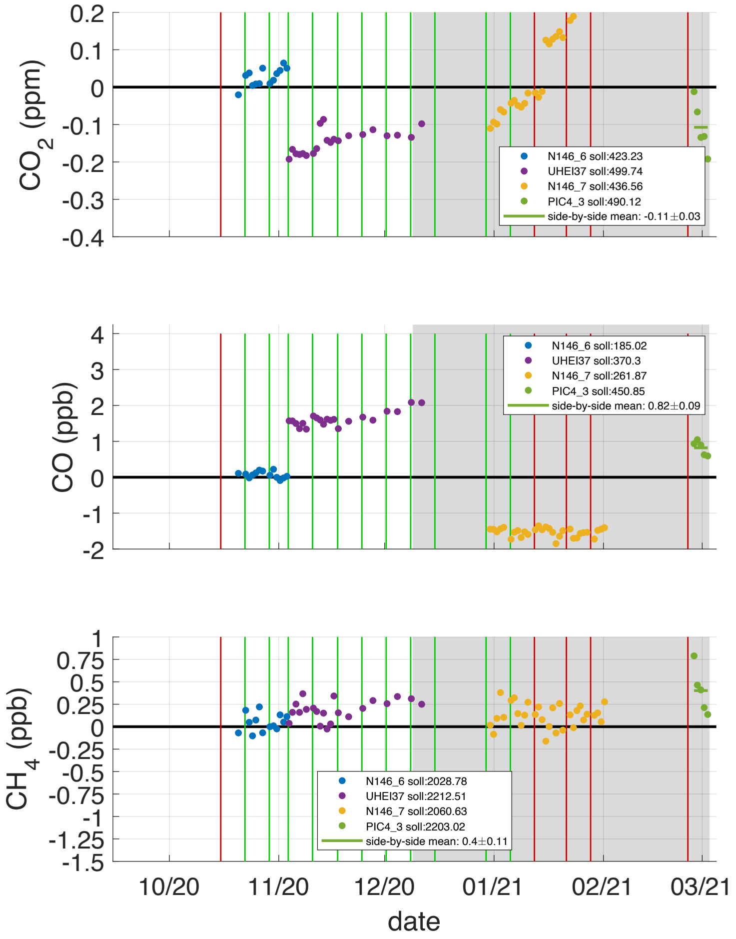

Fig. B.2 FTIR quality control target tanks for the traffic campaign. The vertical lines represent calibration measurements. A green vertical line means the calibration was successful (i.e. I observed no unusually large variations in calibration gas concentrations during manual quality control), while a red line means the calibration was unsuccessful (in such a case the previous calibration is kept). The grey shaded area is the relevant period, where virtual flask episodes occur. Due to the large volume of the measurement cell (3.5 liters) the small gas cylinders did not last for the whole campaign. Thus, four different cylinders functioned as targets for the traffic campaign. N146_6, N146_7 and PIC4_3 were filled and measured at the Institute for Environmental Physics in Heidelberg, whereas UHEI37 was filled and measured at the ICOS FCL in Jena.

off, transported and turned on again. While turned off, the casing is not flushed with N_2 and water vapour can enter the casing. At the new location, the casing is flushed again to purge away the water vapour. This whole process can reset the hysteresis effect seen in Fig. B.3 after the jump in H_2O concentration. It is possible also that the flushing N_2 flow slightly changed when the FTIR was moved. Consequently, conditions relating to H_2O are not necessarily the same for the end of the traffic campaign and the side-by-side comparison. Also, the H_2O concentrations remained stable (Fig. B.4). Therefore, I do not apply the bias

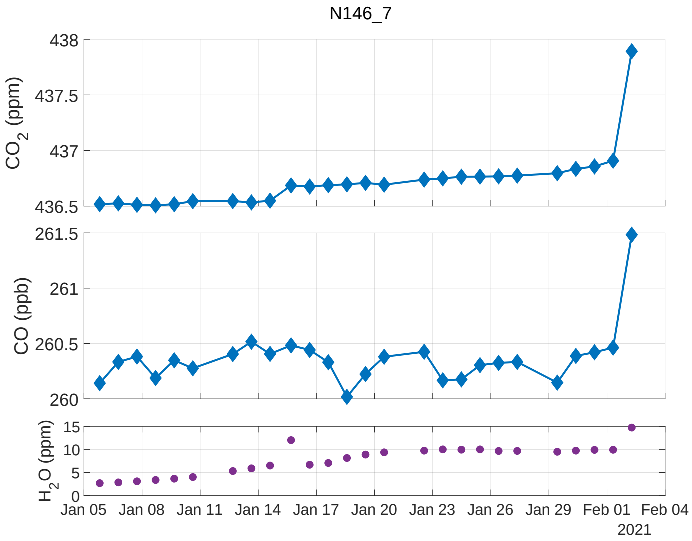

Fig. B.3 Target cylinder N146_7 measurements. First panel shows CO_2, second is CO, and third is H_2O. With the jump in H_2O on January 15, the CO_2 concentrations increased on average by 0.22 ppm. The difference in mean CO over the same periods is less than 0.05 ppb and thus negligible. The last point illustrates the effect of an H_2O increase above 10 ppm, but is not shown in Fig. B.2.

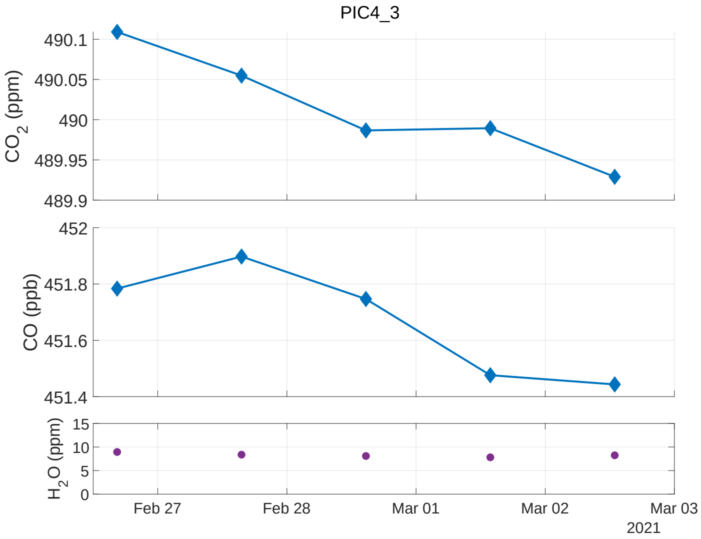

Fig. B.4 Target cylinder PIC4_3 measurements. First panel shows CO_2, second is CO and third is H_2O. This target was attached during the side-by-side comparison and shows roughly constant H_2O concentrations. Variations in CO_2 and CO concentrations do not correlate with changes in H_2O concentrations.

correction to the data of the side-by-side comparison, but do apply the additional uncertainty of ±0.25 ppm to FTIR CO_2 data.

Revisiting Fig. B.2, I find that the target cylinder measurements are not a good tool to estimate the bias of the FTIR. For CO_2, the difference ranges roughly from −0.2 to 0 ppm, for CO from −2 to 2 ppb. This is the reason I cannot base my final bias and uncertainty on the target cylinder measurements. Still, these measurements give us a frame of reference: The uncertainty cannot be smaller than ±0.2 ppm for CO_2 and ±2 ppb for CO.

B.2 Laboratory side-by-side comparison

After the traffic campaign, we brought ML2 next to ML1 to run a side-by-side comparison of the mobile laboratories as a quality check and to estimate the bias between the two MLs. The distance between the in-take lines was <3 m. The experiment ran for six days from February 26 to March 3, 2021. Flasks were taken every second hour during the last afternoon, evening, or night of the experiment. The wind mainly varied between north and west, bringing highway traffic emissions to the mobile laboratories. But February 26 was a Friday, consequently the first three days had relatively small CO_2 and CO concentrations (Fig. B.5). On Monday, March 1, the morning rush hour is captured by the mobile laboratories, bringing CO_2 concentrations up to 510 to 520 ppm and CO concentrations up to 450 ppb. Wind speed was low in the evening/night from the March 2 to 3, leading to accumulation of trace gases during the period when the flasks were sampled.

Initially, the side-by-side comparison was thought to directly supply the bias between ML1 and ML2 for CO_2, CO and NO_x. But concentration differences between the MLs during the side-by-side comparison were unexpectedly high. At closer inspection, several uncertainty sources (listed in the first column of Table B.2) affected the side-by-side comparison, rendering its results inadequate to be used for bias estimation between the MLs. As a consequence, I chose results from flask measurements to estimate the bias for CO and CO_2. Unfortunately, the lifetime of NO_x is too short to be measured in flasks. I therefore cannot determine a bias in NO_x. I can only use the side-by-side comparison results to get an idea how large the maximum bias for hourly differences may be – we will come back to this in Appendix B.3 and only deal with CO_2 and CO until then.

Throughout this section, I will show why the side-by-side comparison was ineffective in reaching the original goal of bias determination. Consider the uncertainty sources (beyond simple measurement uncertainty) listed in Table B.2. First, the two MLs do not measure exactly the same air, even though we brought

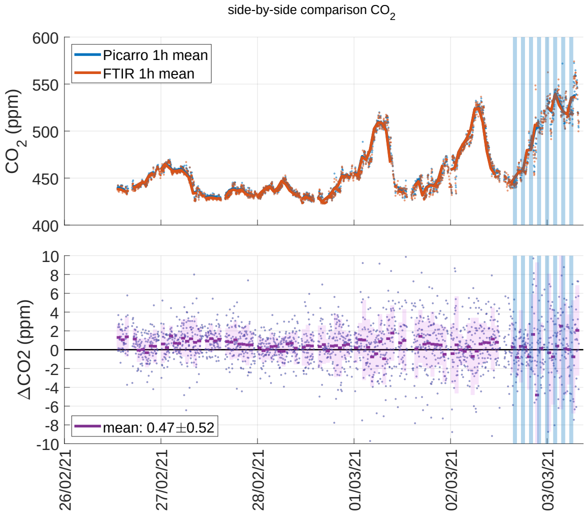

Fig. B.5 Side-by-side comparison for CO_2. The top panel shows atmospheric concentrations and hourly means. The bottom panel shows the minute-by-minute difference (ML1 – ML2), as well as hourly means (horizontal bars) with their standard deviation (pink shaded area). Blue shaded areas are flask sampling times. For the mean hourly difference of 0.47 ± 0.52 ppm, only hourly differences with standard deviations (of the minutely differences) smaller 2 ppm were considered to avoid the air inhomogeneity effect as much as possible.

the MLs as close together as possible. Measuring so close to the highway means that the emission plumes have not mixed completely, thus the concentration field downwind is not homogeneous. I will call this the air inhomogeneity problem. Second, air sucked in simultaneously at both intakes does not reach the instruments at the same time, due to differences in the setup (e.g. flow velocity, in-line resistances). I call this the delay or asynchronicity problem. Third, the flask sampling methods are not the same. While the FCL-built (ML1) flask sampler uses the $1/t$ method, where the flask is flushed with a flow rate decreasing by 1/time, described, e.g. by Levin et al. (2020), the IUP-built (ML2) flask sampler fills the flask from 0 to 2 bar at a constant flow rate. In theory, both methods lead to a constant weighting factor at any given time, i.e. a real average trace gas concentration. In practise, the $1/t$ method requires extremely large flow rates in the beginning to result in a constant weighting factor. Consequently, the first minutes are weighted less than the rest, and the concentrations at the end of the flushing time (30 min before sampling) have a small impact as well. Also, there is a slight delay depending on what port of the flask sampler the flask was collected (physically greater distance). Since no corrections were applied for both effects, small differences between the two flask samplers are expected. All three problems scale with the variation of the atmospheric trace gas concentrations in some shape or form, i.e. possible differences between ML1 and ML2 caused

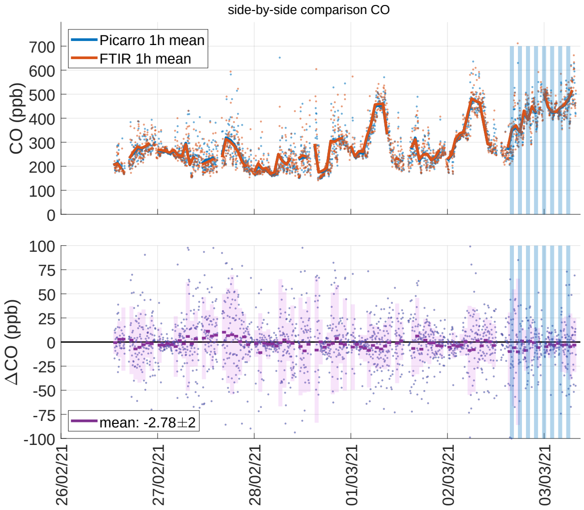

Fig. B.6 Side-by-side comparison for CO. The top panel shows atmospheric concentrations and hourly means. The bottom panel shows the minute-by-minute difference, as well as hourly means (horizontal bars) with their standard deviation (pink shaded area). Blue shaded areas are flask sampling times. For the mean hourly difference of −2.78 ± 2.00 ppb, only hourly differences with standard deviations (of the minutely differences) smaller 15 ppb were considered to avoid the air inhomogeneity effect as much as possible.

by the three problems will increase with increasing concentration fluctuation. Since both laboratories where downwind of the highway for the side-by-side comparison, variations of atmospheric trace gas concentrations were larger than 3.5 ppm.

Figure B.5 shows the side-by-side comparison of continuous CO_2 measurements. The mean difference over the course of the experiment is 0.47 ± 0.52 ppm CO_2, i.e. the Picarro G2401 in ML1 measures slightly higher CO_2 concentrations than the FTIR in ML2. Similarly, Fig. B.6 shows the side-by-side comparison of continuous CO measurements. The mean difference over the course of the experiment is −2.78 ± 2.00 ppb CO, i.e. the Picarro G2401 in ML1 measures slightly lower CO concentrations than the FTIR in ML2. Strong, fast variations in concentration lead to the largest differences between the mobile laboratories, just as hypothesised above. This is evident in the standard deviation for hourly means of CO_2, shown as pink-shaded area in the lower panel of Fig. B.5, which indicates how much the 3-minutely concentration differences vary during that hour. During the rush-hour, the standard deviation can easily double, compared to the days without rush-hour.

The observed average difference between ML1-flasks and ML2-flasks is 0.65 ± 0.56 ppm for CO_2. For CO, the observed mean difference between ML1-flasks

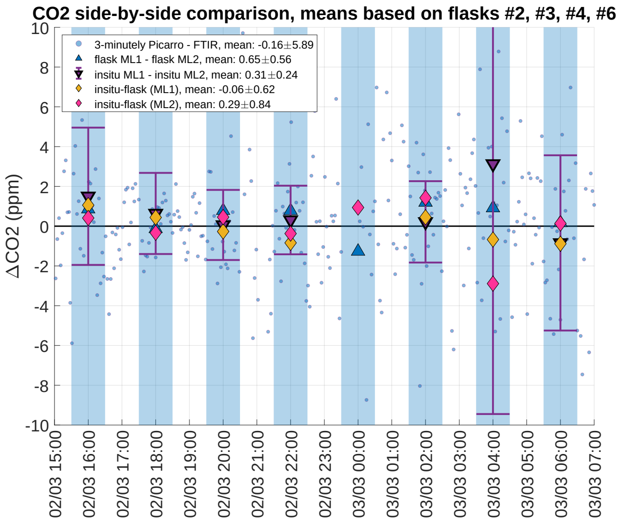

Fig. B.7 Side-by-side comparison for CO_2 in flasks. For March 2, 2021 18:00 h, the in-situ measurements in ML1 contain a large gap, so the mean had to be discarded. Consequently, no flask minus in-situ value and no in-situ minus in-situ value exists.

and ML2-flasks is 1.55 ± 2.20 ppb. Note that these values are based on the flasks sampled in periods when the standard deviation of the concentration difference between ML1 and ML2 was below 2 ppm CO_2 or 15 ppb CO, respectively. I will use the observed mean differences later to check whether my bias correction is reasonable.

For the side-by-side campaign, Figs. B.7 and B.8 show a four-way comparison of differences in CO_2 and CO, respectively. The four differences are in-situ measurements ML1 minus in-situ measurements ML2 (purple triangles), flask measurements ML1 minus flask measurements ML2 (blue triangles), in-situ measurements ML1 minus flask measurements ML1 (yellow diamonds) and in-situ measurements ML2 minus flask measurements ML2 (pink diamonds). During an ideal side-by-side comparison, all the differences would be zero, indicating perfect agreement between in-situ and flask measurements, as well as between mobile laboratories. The differences in some cases agree reasonably well, while in other cases they are driven apart by the variability of atmospheric concentration differences between the MLs (indicated by purple error bars). The mean differences shown in the legend of the figures are based on periods when the standard deviation of the concentration difference between ML1 and ML2 was below 2 ppm CO_2 or 15 ppb CO, respectively. For the FTIR bias calculation, only the thus selected samples will be considered. The numbers of the selected flasks/periods is also written in the headline of the figures.

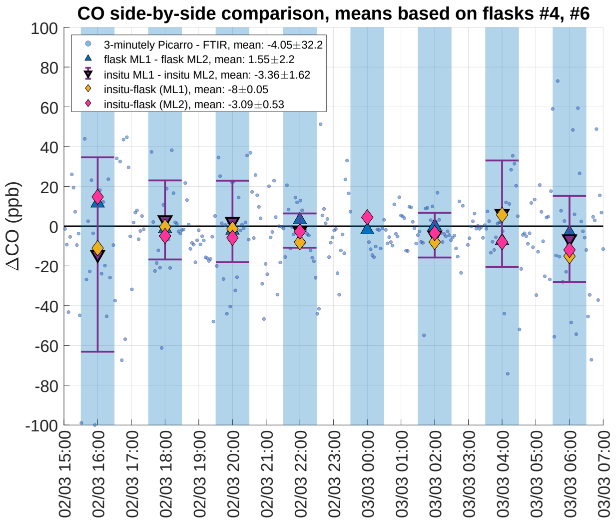

Fig. B.8 Side-by-side comparison for CO in flasks. For March 2, 2021 18:00 h, the in-situ measurements in ML1 contain a large gap, so the mean had to be discarded. Consequently, no flask minus in-situ value and no in-situ minus in-situ value exists.

Air inhomogeneity. We suspect that some of the difference between ML1 and ML2 found during the side-by-side comparison comes from air inhomogeneity. The small distance from the source, i.e. the highway, means that emissions are not well mixed yet when they reach the downwind laboratory. Consequently, the position of the MLs changes the measured concentrations. Does it change the measured ratios, too? Theoretically, if we measure concentration enhancements, the answer is no. No matter which part of the plume we measure (i.e. no matter the dilution), the emission ratio is baked into the plume and does not change with transport. Consequently, even if concentration fluctuations are large, ratio fluctuations ought to be small, because any change in CO_2 is accompanied by a proportional change in CO and vice versa. Formulated as a question: does the measured $\Delta CO/\Delta CO_2$ ratio change significantly with the position of the downwind ML due to air inhomogeneity? If that is not the case, then it is reasonable to assume that air inhomogeneity is at least partly responsible for the concentration difference between ML1 and ML2. It also follows that air inhomogeneity does not affect the results (i.e. effective atmospheric highway emission ratios) of the traffic campaign.

Answering this question requires calculations of $\Delta CO/\Delta CO_2$ for each ML. Beforehand, we have to reduce the mismatch between FTIR and Picarro, since I want to isolate the air inhomogeneity effect. First, I reduced the bias by subtracting the mean difference in CO and CO_2 concentration from the Picarro data. Then, I calculate the enhancements ΔCO and ΔCO_2 by subtracting the lowest value

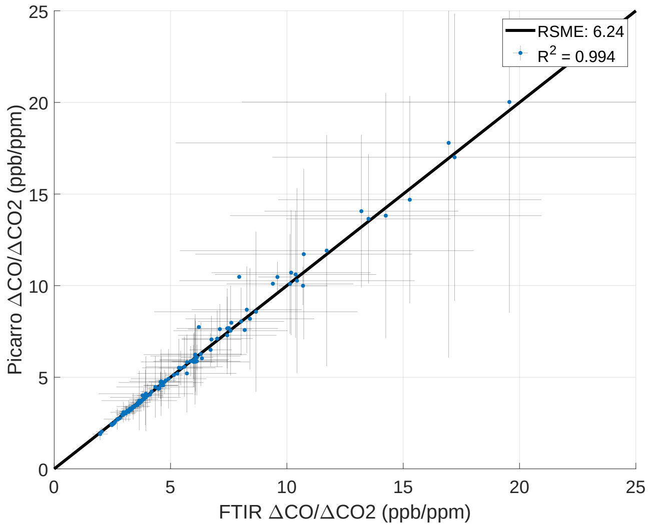

Fig. B.9 Hourly emission ratios $\Delta CO/\Delta CO_2$ measured by Picarro and FTIR in comparison. The underlying black line shows where FTIR ratio = Picarro ratio. Error bars are based on atmospheric CO and CO_2 variability. A weighted total least squares regression yields a slope of 1.02 ± 0.05 with an intercept of -0.081 ± 0.146, i.e. ratios from both instruments agree within error margins.

measured by the FTIR during the side-by-side comparison (one could choose the Picarro just as well). The exact value of the CO and CO_2 background is inconsequential, since I am not interested in determining correct $\Delta CO/\Delta CO_2$ emission ratios. Rather, this step ensures that the relative differences of CO_2 and CO are both comparable to the changes that would affect the true measured ratios in the normal campaign setup.

To reduce the influence of the delay effect, I averaged ΔCO and ΔCO_2 for each instrument over an hour and calculated $\Delta CO/\Delta CO_2$ from these means. Note, that the alternative, calculating the mean of all $\Delta CO/\Delta CO_2$ in one hour would result in an average that is not weighted according to CO_2 enhancements (i.e. if one minute we detect 15 ppb ΔCO and 1 ppm ΔCO_2 and the next minute 50 ppb ΔCO and 10 ppm ΔCO_2, the unweighted mean would be (15 ppb/ppm + 5 ppb/ppm)/2 = 10 ppb/ppm, the weighted mean would be 32.5/5.5 ppb/ppm = 5.9 ppb/ppm) and results in erroneous means. The thus calculated ratios for each instrument are plotted against each other in Fig. B.9. The hourly ratios agree within error margins, indicating that air inhomogeneity does not cause a change in ratio.

In short, when I calculate ratios for both MLs during the side-by-side comparison in the same way I do for virtual flasks during the campaign, the ratios are unaffected by air inhomogeneity. At the same time, air inhomogeneity does (at least partly) explain the difference in CO_2 and CO concentration between the two MLs. Consequently, the side-by-side comparison cannot be used to estimate the true bias.

B.3 Bias correction

FTIR and Picarro G2401 data have to be corrected to remove the systematic bias between the two. Usually, target measurements suffice, but as shown in Fig. B.2 it is not clear how to correct the instrument measurements, because the FTIR shows a different offset for each target (and trace gas). To overcome this issue, I take advantage of the sampled flasks, that were measured at ICOS FCL, Jena. ICOS FCL delivers reliable concentration values measured under excellent laboratory conditions with tightly controlled and checked calibration cylinders as well as target cylinders. The same instrument is used for flasks from both ML1 and ML2. In other words, the flask measurements are an independent reference on which the bias correction is based. Using flask measurements to estimate the bias has another advantage. In contrast to target cylinders, which – by design – only show the difference between measurements and expected values for one specific concentration of a trace gas, the deviations between flasks and in-situ measurements cover a broader range of concentrations for all trace gases. Consequently, I argue that the standard deviations of the mean difference between in-situ instrument and flask measurement is an excellent measure for the accuracy of our measurements.

One obstacle when using the comparison between in-situ measurements and flasks to estimate the bias is that the achievable agreement between the two depends on atmospheric concentration variability. Levin et al. (2020) showed that in Heidelberg, for the flask and in-situ measurements to agree within roughly ±0.1 ppm CO_2, the atmospheric CO_2 concentration may not vary more than 1 ppm (the standard deviation of the hour in question is defined as the CO_2 variation). The left plots in Figs. B.10 and B.11 show the difference between in-situ measurements and flasks plotted against the atmospheric concentration variability for both FTIR/ML2 (orange and red triangles) and Picarro (dark and light blue x and +), for CO_2 and CO, respectively. Darker colours indicate flasks sampled during the campaign, lighter colours indicate flasks sampled during the side-by-side comparison. These figures are similar to Figs. 3 and Fig. 4 by Levin et al. (2020).

Following Levin et al. (2020), to estimate the FTIR CO_2 bias (versus flask measurements) I only consider flask samplings during which the atmospheric CO_2 variability is smaller than 2 ppm. For the CO bias, I only consider flask samplings

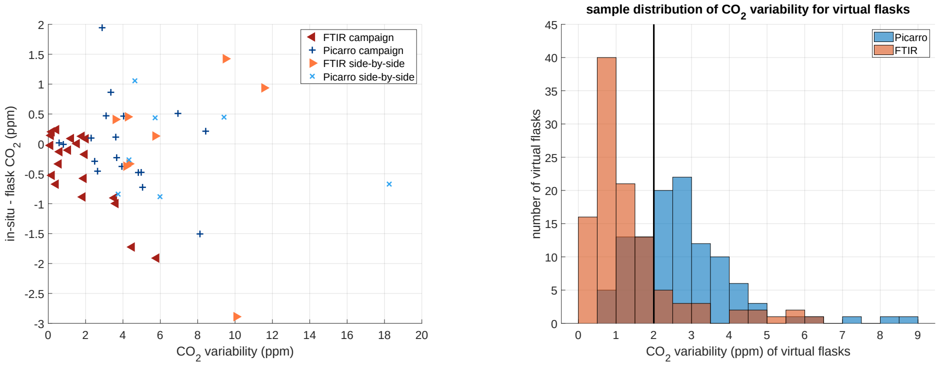

Fig. B.10 Left: CO_2 difference in-situ minus flask plotted over CO_2 variability (standard deviation of atmospheric concentration over the hour). Right: Sample distribution of CO_2 variability for virtual flasks.

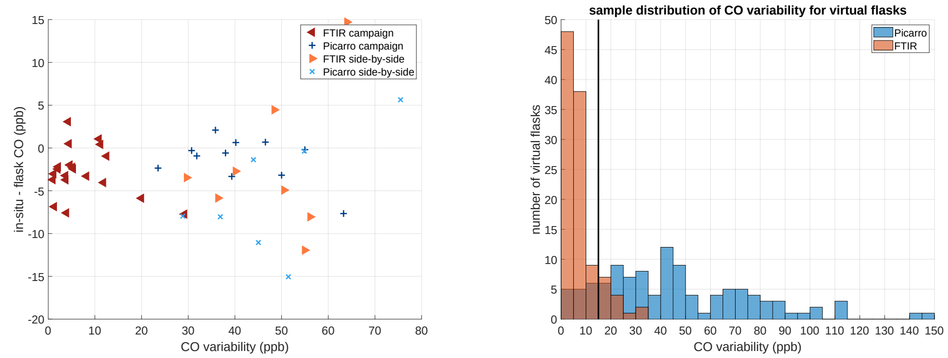

Fig. B.11 Left: CO difference in-situ minus flask plotted over CO variability (standard deviation of atmospheric concentration over the hour). Right: Sample distribution of CO variability for virtual flasks.

during which the atmospheric CO variability is smaller than 15 ppb (Fig. B.11, left). The CO_2 threshold I choose is more lenient than by Levin et al. (2020): 2 ppm instead of 1 ppm. I do not require the level of precision or accuracy described in the paper. From Fig. B.10 (left) I surmise that no outliers between 1 ppm and 2 ppm CO_2 variability exist, which are much further from zero than the outliers between 0 ppm and 1 ppm CO_2 variability. The threshold for CO is an educated guess from Fig. B.11 (left). I took a value that would divide the plot similarly as 2 ppm divides the plot in Fig. B.10 (left) and that – applied to virtual flasks – would contain most upwind (FTIR) samples in Fig. B.11 (right). Most virtual flasks exhibit such favourable low variability conditions at the upwind mobile laboratory (ML2), as shown in the right plot of Figs. B.10 and B.11. The thick black vertical line indicates the threshold. As most virtual flasks fall below the thresholds, the FTIR biases calculated from these sub-samples are good estimates to correct all virtual flasks.

For the bias (versus flask measurements) of the Picarro G2401 instrument, consider that the proximity to the highway results in high CO_2 and CO variabilities for all flasks (excluding two, for which the CO_2 variability was <1 ppm). I decided to take all campaign flasks into consideration, as well as side-by-side comparison flasks for which the variation of the difference between ML1 and ML2 was <2 ppm. Otherwise, no bias correction with in-situ versus flask measurements would be possible for the Picarro. I support the decision to consider all flasks with the following argument. In case ML1 always encounters high CO_2 and CO variability during flask sampling, uncertainty and bias should reflect this. As Figs. B.10 and B.11 show, this is indeed the case. All but two ML1 flasks (in blue) show CO_2 variabilities larger than 2 ppm and all ML1 flasks show CO variabilities larger than 20 ppb.

The FTIR is biased by -0.15 ± 0.51 ppm CO_2 and -2.11 ± 2.85 ppb CO. The Picarro is biased by -0.02 ± 0.72 ppm CO_2 and -2.96 ± 5.11 ppb CO. The total biases of ΔCO_2 and ΔCO are

$$b_{\Delta CO_2} = -0.13 \pm 0.88\,\text{ppm}, \tag{B.1}$$

$$b_{\Delta CO} = -0.85 \pm 5.85\,\text{ppb}. \tag{B.2}$$

During the side-by-side comparison, I found the difference between Picarro and FTIR to be $\Delta CO_2 = 0.47 \pm 0.52$ ppm and $\Delta CO = -2.78 \pm 2.00$ ppb (calculated based on hourly means of the difference, see Figs. B.5 and B.6). With the bias correction, the values are closer to zero and are less than $1\,\sigma$ away from zero. The results of the target measurements (±0.2 ppm CO_2, ±2 ppb CO) are also well within the uncertainty margins of the bias. Therefore, I conclude that the calculated bias and uncertainty is adequate both for CO_2 and CO.

The offsets ΔCO_2 and ΔCO from which the emission ratios for the virtual flasks are calculated, will have their biases corrected according to Eq. (B.1) (displayed values are subtracted, i.e. the CO offset increases, the CO_2 offset decreases and thus the ratio increases).

Finally, coming back to NO_x, it should be clear by now that the methods applied to determine CO_2 and CO bias and uncertainty cannot be applied to NO_x. Apart from the above mentioned problems, the main problem with the NO_x measurements is that the instruments, in order to measure NO_2 as well as NO_x, switch between normal sample air (for NO_2) and O_3-enriched sample air (for NO_x). Consequently, there is some switch-over period during which data have to be discarded. These data gaps affect the minutely mean, especially when concentrations change fast. This, in conjunction with the air inhomogeneity effect, leads to the bias seen

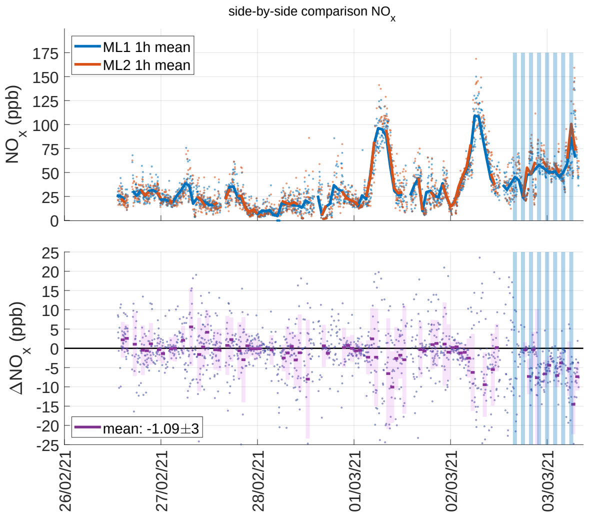

Fig. B.12 Side-by-side comparison for NO_x. The top panel shows atmospheric concentrations and hourly means. The bottom panel shows the minute-by-minute difference (ML1 - ML2), as well as hourly means (horizontal bars) with their standard deviation (pink shaded area). Blue shaded areas are flask sampling times. For the mean hourly difference of -1.09 ± 3.00 ppb, only hourly differences with standard deviations (of the minutely differences) smaller 8 ppb were considered to avoid the air inhomogeneity effect as much as possible.

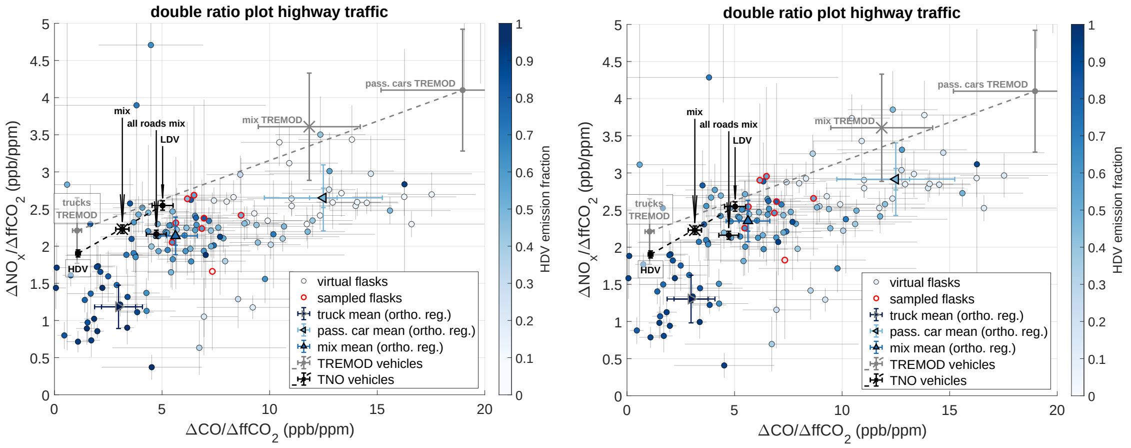

(a) Original.

(b) ΔNO_x increased by 10%.

Fig. B.13 Proxy ratios of traffic campaign flasks plotted against each other. Black points show TNO traffic sector ratios. The traffic fuel mix lies on the dashed line between diesel and gasoline. Traffic ratios for highways are shown separately. Points in shades of blue represent virtual flasks: the darker the color, the higher the fraction of trucks on the highway. Flask samples are marked with a red border. TREMOD ratios for pure truck traffic (bottom left) and pure car traffic (top right) are shown in grey and connected by a dashed line of the same color.

in Fig. B.12. For high NO_x concentrations around 100ppb, the absolute hourly difference reaches up to 10 ppb, in one case even 15 ppb, or 10 % to 15 %. Since the difference at high NO_x concentrations are always negative (ML − ML2 < 0), NO_x emission ratios could be underestimated by up to 10 % to 15 %, but likely less, since the air inhomogeneity effect does increase the difference during the side-by-side comparison, but leaves emission ratios unaffected (cf. paragraph 'Air inhomogeneity' above). To gauge what difference a 10 % increase in ΔNO_x makes, I show a version of Fig. 3.6 with a 10 % increase in ΔNO_x in Fig. B.13b side by side with the original (Fig. B.13a). Overall, the distance to the TNO and TREMOD points decreases with increasing ΔNO_x. The $\Delta NO_x/\Delta ffCO_2$ mix mean value is centered between TNO's 'all roads mix' value and LDV value, instead of being on the same level in $\Delta NO_x/\Delta ffCO_2$ like the 'all roads mix' point. While in the original plot TNO seems to underestimate CO emissions, with the increased NO_x it looks like NO_x is also underestimated slightly for the 'mix' and 'LDV' point. As discussed above, Fig. B.13b most likely shows overestimated $\Delta NO_x/\Delta ffCO_2$, since a 10 % increase is the upper limit of possible bias. Even a 10 % increase in $NO_x/\Delta ffCO_2$ does not ameliorate the difference between measured truck $NO_x/\Delta ffCO_2$ and inventory $NO_x/\Delta ffCO_2$. I therefore argue that this is a real discrepancy that may have to be addressed by the responsible emission inventory experts.

Figures B.14 and B.15 investigate prevalent wind direction and hour of day when 'sampling' starts, respectively by showing the same data as Fig. 3.6 but using different color bars. Figure B.14, where $f_{\mathrm{HDV}}^{\mathrm{emis}}$ color bar was replaced by wind direction (from 250° to 345°), shows no clear correlation between color and ratios. This is additional evidence in favour of the *same air-mass approach*. A strong dependence on wind direction would suggest influence by other sources from a specific wind direction. In Fig. B.15, where the hour of day is color-coded, virtual flasks 'sampled' during nightly hours (between 22:00 h and 4:00 h) are in the bottom left, while mid-day points are in the top right, similar to the distribution of $f_{\mathrm{HDV}}^{\mathrm{emis}}$. This correlation between hour of day and $f_{\mathrm{HDV}}^{\mathrm{emis}}$ is expected. Passenger cars are primarily used for work-related travel (commuting, crafts-persons visiting customers) during day, while truck driving is a work also carried out during the night. Thus, nightly emissions are always dominated by trucks whereas daytime emissions are dominated by passenger cars.

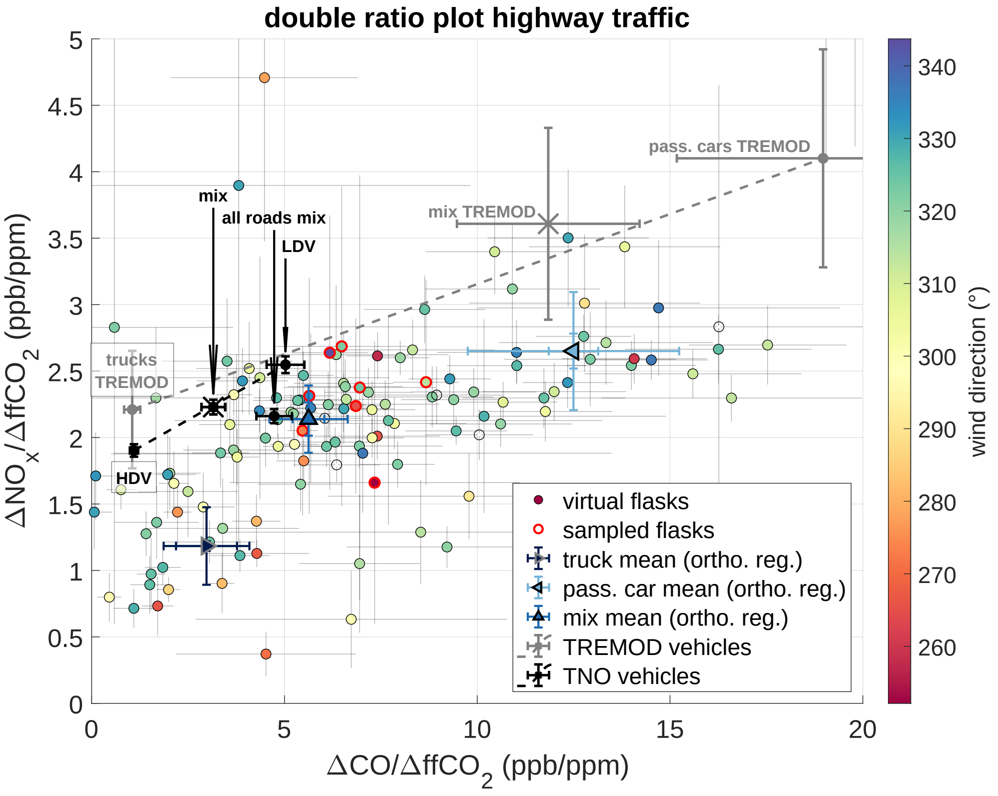

Fig. B.14 Proxy ratios of traffic campaign flasks plotted against each other. Rainbow colored points represent virtual flasks where the color codes the prevalent wind direction. Real flask samples are marked with a red border. Black points show TNO emission ratios for three traffic vehicle categories: light duty vehicles (LDV), heavy duty vehicles (HDV), and mix (LDV & HDV). Similarly, TREMOD emission ratios for truck-only traffic (bottom left) and car-only traffic (top right) are shown in grey and connected by a dashed line of the same color.

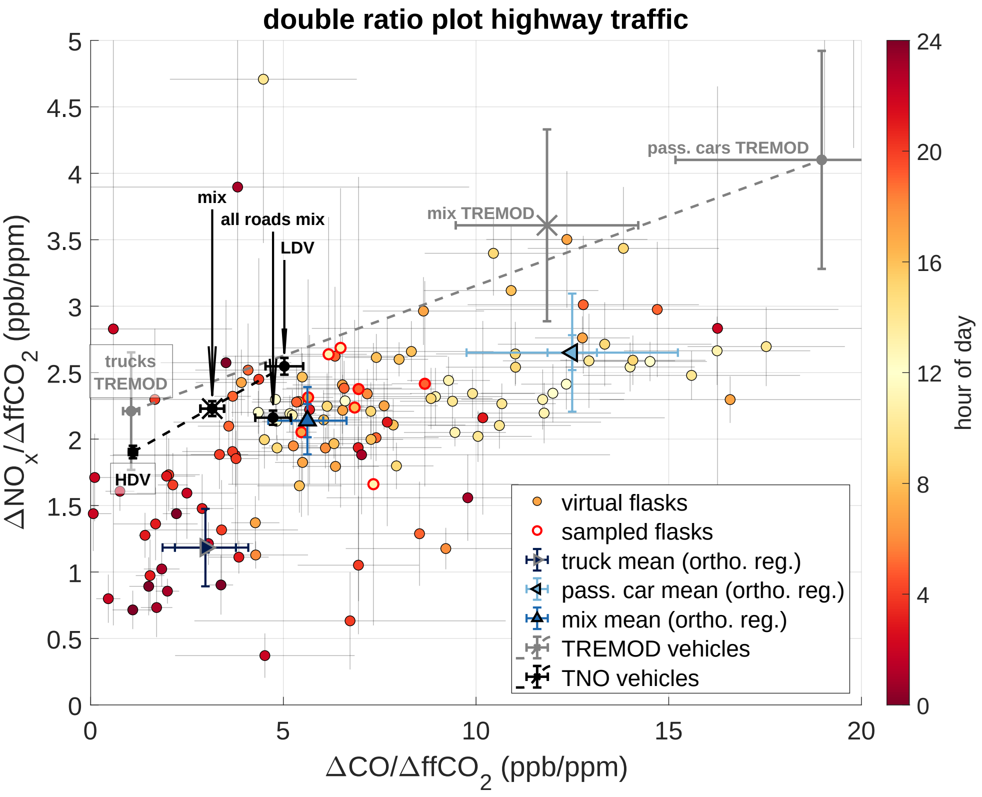

Fig. B.15 Proxy ratios of traffic campaign flasks plotted against each other. Points in shades of yellow-orange-red represent virtual flasks where the color codes the hour of the day when 'sampling' starts. Real flask samples are marked with a red border. Black points show TNO emission ratios for three traffic vehicle categories: light duty vehicles (LDV), heavy duty vehicles (HDV), and mix (LDV & HDV). Similarly, TREMOD emission ratios for truck-only traffic (bottom left) and car-only traffic (top right) are shown in grey and connected by a dashed line of the same color.

Appendix C

Data for long-term record

This appendix provides an overview of the data processing for the long-term record in Heidelberg. Starting with the data sources, it then discuss the fitting routine, uncertainties, and lastly the averaging. The data sets in question are: $^{14}CO_2$, CO_2 and CO for MHD and Heidelberg, as well as nuclear $\Delta^{14}CO_2$ and biospheric $\Delta^{14}CO_2$ for Heidelberg.

C.1 Data sources

Mace Head CO_2 and CO data were provided through OBSPACK (Schuldt et al., 2021a,b). Both data sets were acquired in February 2022 and covered the range from 2000 until 2020. For the two remaining winter months January and February 2021, data were extrapolated with the fitting routine described later in this chapter. For CO and CO_2, the data were weekly surface flasks[34], flagged for background and non-background situations (we only used background situations). The Heidelberg CO_2 and CO record are data measured by GC until 2018. 2019 CO data show large deviations between GC and two other instruments, therefore from January 2019 until February 2021 the record is covered by the Picarro instrument instead. To avoid a jump in concentrations, Picarro data were shifted by the mean offset between GC and Picarro for integrated samples during the overlapping period in 2018 ($\Delta CO_2 = -1.1\,\text{ppm}$, $\Delta CO = 2.1\,\text{ppb}$). The $\Delta^{14}CO_2$ data for both Heidelberg and MHD were provided by our own ICOS RCL in Heidelberg, where the samples were measured.

$\Delta^{14}CO_2$ nuclear correction. Nuclear facilities emit $^{14}CO_2^{\text{nuc}}$. A minor correction is applied to the measured $\Delta^{14}CO_2$ to account for $^{14}CO_2^{\text{nuc}}$ emissions. In the following, three models are discussed: STILT (used by Ida Storm (unpublished) on the Carbon Portal), WRF-STILT (Maier et al., 2021) and HYSPLIT (Kuderer et al., 2018). Details on the HYSPLIT parameters are given by Kuderer et al. (2018)

---

[34] For CO_2, an in-situ record is also available. Maksym Gachkivskyi (unpublished) found no difference between the smoothed curves based on weekly samples and hourly data.

in their Table 2. STILT (as used on the Carbon Portal) uses ECMWF (European Centre for Medium-range Weather Forecasts) meteorology at a resolution of 0.25° × 0.25°. Emissions are mapped onto a 0.125° × 0.083° grid (longitude × latitude) and emitted at the surface (surface source influence ansatz). WRF-STILT uses ECMWF ERA5 meteorology at a resolution of 0.25° × 0.25°, brought to a resolution of 2 km in the Rhine Valley and 2 km everywhere else. Emissions are released in heights between 120 m to 140 m (volume source influence ansatz). Both STILT models use annual emissions from the RAdioactive Discharges Database (RADD, annual emissions available for EU members), while Kuderer et al. (2018) use data from the German Federal Office for Radiation Protection and monthly emissions from nuclear power plant Philippsburg (obtained through personal communication).

As nuclear emissions are mainly released from stacks with a height of typically >100 m, the standard STILT surface source influence ansatz (i.e. releasing all emissions from the ground) used by Ida Storm can result in too large ${}^{14}\mathrm{CO_2}^{\mathrm{nuc}}$ contamination estimates from facilities in the near-field (ca. <50 km) of Heidelberg. Therefore, I split the correction term into a near-field and a far-field component, i.e.

$$\Delta^{14}\mathrm{CO}_2^{\mathrm{nuc}} = \left(\Delta^{14}\mathrm{CO}_2^{\mathrm{nuc}}\right)_{\mathrm{near}} + \left(\Delta^{14}\mathrm{CO}_2^{\mathrm{nuc}}\right)_{\mathrm{far}} . \tag{C.1}$$

In the vicinity of Heidelberg, there are five facilities (Biblis, Karlsruhe, Obrigheim, Neckarwestheim, Philippsburg) too close to use the surface source influence ansatz. Kuderer et al. (2018) calculated nuclear $\Delta^{14}\mathrm{CO}_2$ emissions with HYSPLIT, emitted at the correct stack height, for these five facilities. I combined both data sets (Carbon Portal and Kuderer) to estimate Delta${}^{14}\mathrm{CO_2}^{\mathrm{nuc}}$ in Heidelberg for 2000 to 2017, and added Delta${}^{14}\mathrm{CO_2}^{\mathrm{nuc}}$ emissions of Maier et al. (2021), calculated with the volume source influence ansatz, which assumes that the emissions are released at 120 m to 140 m (typical stack heights) for 2018 to 2020. The Carbon Portal data cover the years 2006 to 2020. For the earlier years 2000 to 2005, the data were extrapolated. I calculated a dilution factor f^{nuc} (in ‰/GBq per year) for every available year (2006 to 2020):

$$f_i^{\mathrm{nuc}} = \frac{\left\langle \left(\Delta^{14}\mathrm{CO}_2^{\mathrm{nuc}}\right)_{\mathrm{far}} \right\rangle_i}{E_i^{\mathrm{far}}} , \tag{C.2}$$

where E_i^{far} are the RADD emissions in year i for far-field sources (i.e. more than 50 km from Heidelberg) and $\left\langle \Delta \left({}^{14}\mathrm{CO_2}^{\mathrm{nuc}}\right)_{\mathrm{far}} \right\rangle_i$ is the annual mean Delta${}^{14}\mathrm{CO_2}^{\mathrm{nuc}}$ influence from far-field sources. In other words, I calculate how much of the emitted $\Delta \left({}^{14}\mathrm{CO_2}^{\mathrm{nuc}}\right)_{\mathrm{far}}$ ends up in Heidelberg. Next, I calculated the mean dilution factor $\overline{f}^{\mathrm{nuc}}$ between 2006 and 2013. After 2013, the dilution factor declines steadily. I read this as a general trend and conclude that it is more appropriate to only average the dilution factors for the earlier years 2006 to 2013 to get a good estimate for the year 2000 ot 2005. I multiply $\overline{f}^{\mathrm{nuc}}$ with the far-field RADD emissions for 2000-2005 to estimate the far-field Delta${}^{14}\mathrm{CO_2}{}^{\mathrm{nuc}}$ influence:

$$\overline{f}^{\mathrm{nuc}} \cdot E_i^{\mathrm{far}} = \left(\Delta^{14}\mathrm{CO}_2^{\mathrm{nuc}}\right)_{i,\,\mathrm{far}} . \tag{C.3}$$

Kuderer et al. (2018) calculated near-field Delta${}^{14}\mathrm{CO_2}{}^{\mathrm{nuc}}$ influences for the years 1986 to 2015. I extrapolated the results from Kuderer et al. (2018) for 2016 and 2017 similarly to the extrapolation for the far-field. The dilution factor this time was based on the years 2011 to 2015, because in 2011, the nuclear power plant Philippsburg Block-I was shut down. Note that, since RADD emissions are only available on a yearly basis, the extrapolated corrections also do not change over the year.

To summarise, the nuclear corrections were split into a near-field and a far-field component. For 2000 to 2017, far-field emissions are based on surface source influence calculations from the Carbon Portal (extrapolated for 2000 to 2005) while near-field emissions are based on Kuderer et al. (2018) calculations (extrapolated for 2016 to 2017). Necessary extrapolations are based on RADD emissions and average dilution factors that describe how much of the ${}^{14}\mathrm{CO_2}{}^{\mathrm{nuc}}$ emissions described in RADD reach Heidelberg on average. For 2018 to 2020, the volume source influence ansatz WRF-STILT calculations of Maier et al. (2021) are used for both near-field and far-field contributions.

The far-field extrapolations I used are rather rough estimates of the nuclear $\Delta^{14}\mathrm{CO_2}$ influence. However, making the estimates more precise, i.e. using a more sophisticated model, does not change the results, because the far-field nuclear influence is very small (on average 1 ‰), smaller than the uncertainty of $\Delta^{14}\mathrm{CO_2}$ measurements (2 ‰). Consequently, a rough estimation of far-field influence is sufficient. $\Delta^{14}\mathrm{CO_2}$ from near-field nuclear facilities occasionally surpass the measurement uncertainty. When Philippsburg Block-I was still running, the $\Delta^{14}\mathrm{CO_2}$ occasionally reached >10 ‰, but since then near-field nuclear influence mostly falls below 2 ‰. Consequently, a rough estimation of near-field influence in 2016 and 2017 is sufficient. Generally speaking, after the shutdown of Philippsburg Block-I, the total nuclear correction for $\Delta^{14}\mathrm{CO_2}$ is smaller than 4.5 ‰, roughly equivalent to $2\,\sigma$ uncertainty of the measurement. It is a necessary correction, since otherwise the measurements are biased, but rough estimates of near and far field influence (in years without modelling of such) suffice.

For the biogenic $\Delta^{14}\mathrm{CO_2}$ contribution from heterotrophic respiration, the model by Naegler (2005) was used. His calculations were extended to the current year by Levin et al. (2011). Naegler and Levin (2009b) provided two scenarios HI(gh) and LO(w) activity of the biosphere. The mean of $\Delta^{14}CO_2$ HI and LO was used for calculations in this thesis.

C.2 Fitting routine

Maksym Gachkivskyi (unpublished) implemented and ran the fitting routine for the whole work group so we would have a consistent data set. For CO_2 and CO in MHD, we used the full CCGRV routine (Carbon Cycle Greenhouse gases Curve Fitting Methods, 2022), including the high-frequency filter. The short-term cutoff parameter was 240 days for $\Delta^{14}CO_2$ and 160 days for ΔCO_2 and CO. This parameter describes at what frequency the filter response is 0.5 on the residuals, evaluated daily (Carbon Cycle Greenhouse gases Curve Fitting Methods, 2022). The daily record was then averaged over the time frames of the integrated samples in Heidelberg.

For $\Delta^{14}CO_2$, we used a more rigid fit of the CCGCRV routine, i.e. only using the harmonic, polynomial and inter-annual parts of the fit function excluding the residual analysis. We argue that this provides a solid curve, that is understood physically: a gradual, polynomial decrease of $\Delta^{14}CO_2$, with a yearly harmonic oscillation superimposed and allowance for small inter-annual variations. Otherwise, we would rely heavily on each measurement point, although we know that the uncertainty of $\Delta^{14}CO_2$ measurements is high. In the wake of this discussion, we also discovered a temporary problem with measurements between 2010 and 2012 in Heidelberg. Consequently, samples measured in the period from June 29, 2010 to July 3, 2012 were excluded from the fit.[35]

C.3 Individual ratio uncertainties

Assigning correct uncertainties is paramount for the interpretation of results. The sources of uncertainty described here are (1) instrument/measurement uncertainty (i.e. how precise are the measurements?), (2) representativeness uncertainty (i.e. how well-defined is our background?), (3) fit uncertainty (i.e. how well does our fit describe the real concentrations?) and (4) model uncertainty.

---

[35] The dates refer to the point in time when the samples were *measured* in Heidelberg, not when they were taken at Mace Head.

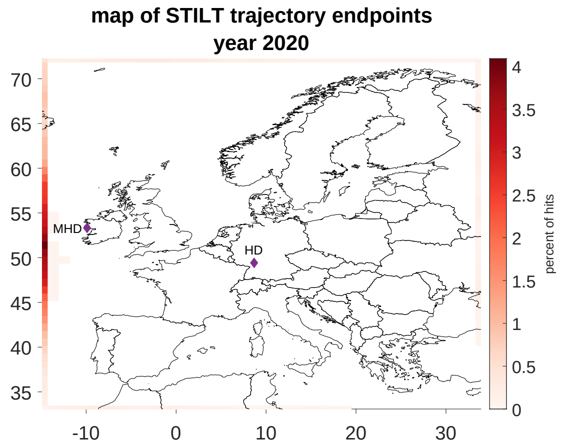

Fig. C.1 Endpoints of back-trajectories for Europe, modelled with STILT by Fabian Maier (unpublished). For every hour in the year 2020, 100 particles were transported 10 days backwards in time. The underlying meteorological data have a 0.25° × 0.25° resolution and were provided by ECMWF. Darker colors indicate higher fraction of trajectories ending in that area. Trajectories that would go beyond the borders of the STILT domain have their endpoints at the edge of the domain. Very few particles actually remain in the STILT domain, consequently most coloration is at the edges of the domain. For visibility, ten vertically adjacent STILT cells are summed and then plotted (i.e. the real STILT resolution is ten times finer than the resolution of the rectangles shown here). MHD (suggested background station) and Heidelberg (release point of particles) are shown as purple diamonds.

Instrument/measurement uncertainty. From instrument inter-comparisons, we determined the measurement uncertainty of our Heidelberg instruments to be $\Delta CO_2 = 0.1\,\mathrm{ppm}$ and $\Delta CO = 3\,\mathrm{ppb}$. $\Delta^{14}CO_2$ uncertainties are well established in the measurement process and usually amount to approximately $\delta\left(\Delta^{14}CO_2\right) \approx 2‰$. This is true for Heidelberg and MHD samples, since they are both measured at the ICOS CRL in Heidelberg. We also transfer the measurement uncertainty found for CO_2 and CO in Heidelberg to MHD, assuming that there is no significant quality difference between the involved instruments.

Representativeness uncertainty. For CO, additional uncertainties have to be estimated. Unlike CO_2 and $\Delta^{14}CO_2$ that differ very little between MHD and other maritime background stations like Izaña in winter, CO has a latitudinal gradient. The latitudinal gradient causes differences in CO between MHD and Izaña of up to 25 ppb in winter. Based on STILT trajectories for 2020 by Fabian Maier (unpublished), we find that most air that arrives in Heidelberg previously passed close to MHD as can be seen in Fig. C.1. I used the spread of the trajectory endpoints on the western edge of the STILT domain in conjunction with an assumed linear latitudinal CO gradient to estimate the representativeness uncertainty and bias. While the bias was small (1.15 ppb CO), the standard

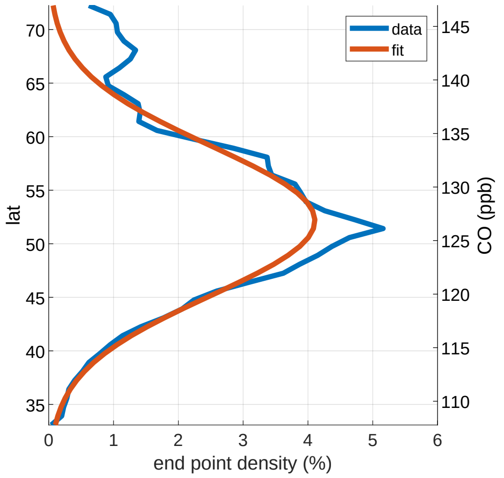

Fig. C.2 Fit of STILT trajectory endpoint distribution at the west edge of the STILT domain. Mace Head is at a latitude of 53.3° N, very close to the peak of the fit curve. I assume a latitudinal CO gradient of 1 ppb/°, i.e. a difference between Mace Head and Izaña (28.3° N) of 25 ppb CO.

deviation of the probability distribution function was 7 ppb CO. This is added as an independent error (i.e. no Gaussian error propagation) to the CO record in MHD. While this suffices for the purpose of estimating the representativeness uncertainty for this case, this method has some shortcomings. First, only the year 2020 was investigated. The magnitude of variations between years could not be investigated in the scope of this thesis. Second, I only used the trajectory endpoints counted on the western edge of the STILT domain (i.e. including all that fall to the west of this), which make up 77 % of all points. The remaining points, mostly counted on the other edges of the STILT domain, are ignored to reduce the problem to one dimension (edge of the domain). Third, we assume a linear latitudinal gradient in CO from Izaña (28.3° N) to Mace Head (53.3° N) with an upper bound 25 ppb CO in winter (based on CO data from Izaña and Mace Head). While this gradient has been described in the literature (Novelli et al., 1998, Fig. 7), assuming it is linear is a simplification. I also ignore the altitude difference between the two stations (Izaña 2373 m, MHD 5 m), i.e. I assume both measure a free troposphere background. Forth, to estimate the width of the distribution of trajectory endpoints I fitted a Gauss-curve to the data, see Fig. C.2. There is not mathematical basis for this, i.e. there is no reason to assume the trajectory endpoints follow this specific probability distribution. Visually, the width of the curve fits the data well enough for me to deem the standard deviation an appropriate parameter to quantify the spread of the trajectory endpoints.

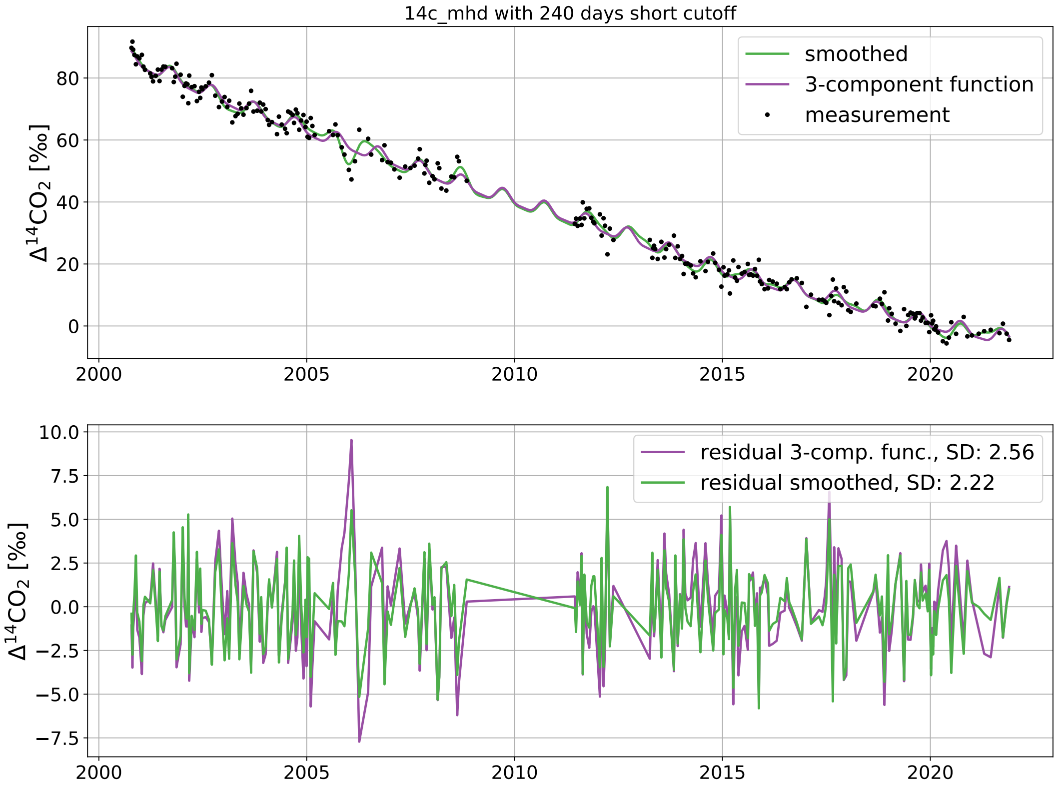

Fig. C.3 MHD $\Delta^{14}CO_2$ fit with CCGCRV routine by Maksym Gachkivskyi (unpublished). While the 'smoothed' fit uses all tools in the CCGCRV routine, the '3-component function' is comprised of the polynomial, the harmonic and the inter-annual variation parts of the fit (no analysis of the residual). The short term cut-off parameter for the FFT was set to 240 days. The results from the '3-component function' fit are used in the evaluation.

Fit uncertainty. The fit routine is another source of uncertainty. I estimate this uncertainty by calculating the standard deviation of the fit with regards to the data points (as expected, the bias is zero). The fit uncertainty is 2.56 ‰ for $\Delta^{14}CO_2$, 1.15 ppm for CO_2 and 9.4 ppb for CO. Figures C.3 to C.5 show data points and fit functions either with ('smoothed') or without ('3-component function') analysis of residuals. The second panel shows residuals from the fit function to the data points. For $\Delta^{14}CO_2$, the '3-component function' fit is used. For CO and CO_2, the 'smoothed' fit was applied. The decision which plot to use is based on our confidence in the data and was described previously in Appendix C.2.

Uncertainty for nuclear and biogenic contributions. The biogenic and nuclear corrections were modelled. For the biogenic heterotrophic $\Delta^{14}CO_2^{\mathrm{bio,het}}$, Naegler and Levin (2009b) give a lower and upper bound, as well as the best estimate. I use the best estimate in my calculations. As an uncertainty I simply use the distance

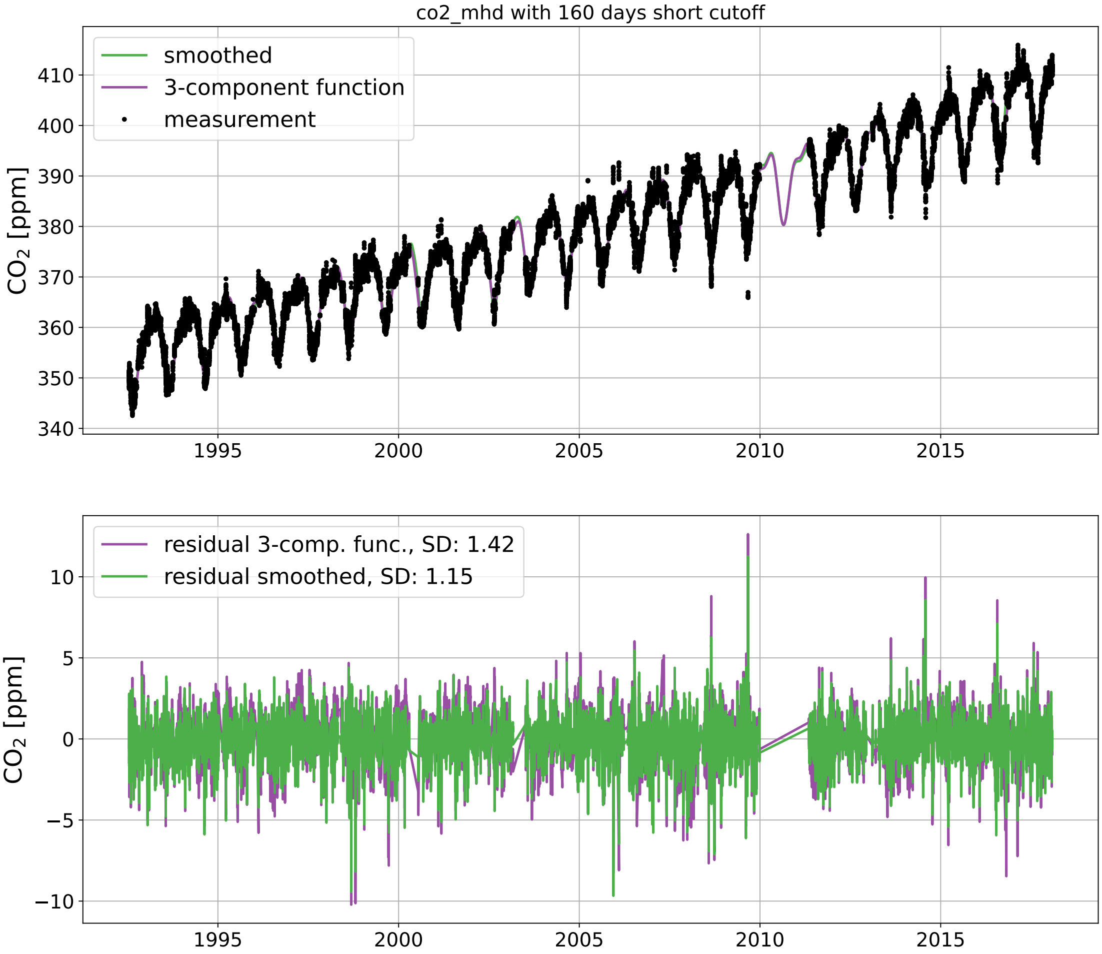

Fig. C.4 MHD CO_2 fit with CCGCRV routine by Maksym Gachkivskyi (unpublished). While the 'smoothed' fit uses all tools in the CCGCRV routine, the '3-component function' is comprised of the polynomial, the harmonic and the inter-annual variation parts of the fit (no analysis of the residual). The short term cut-off parameter for the FFT was set to 160 days. The results from the 'smoothed' fit are used in the evaluation.

to the upper/lower bound. As described in Appendix C.1, the nuclear correction is a compound of different models, mostly based on the RADD nuclear emission inventory. RADD only provides annual emissions without any information on the smaller time scales (months, weeks, days, etc.). Without more detailed information available, I assume a relative uncertainty of 100 %.

Gap uncertainty. The in-situ instruments used for continuous CO_2 and CO measurements in Heidelberg require constant attention and maintenance. Even when running perfectly, calibrations and target cylinder measurements break the continuity of the air measurements periodically. The integrated $\Delta^{14}CO_2$ samples

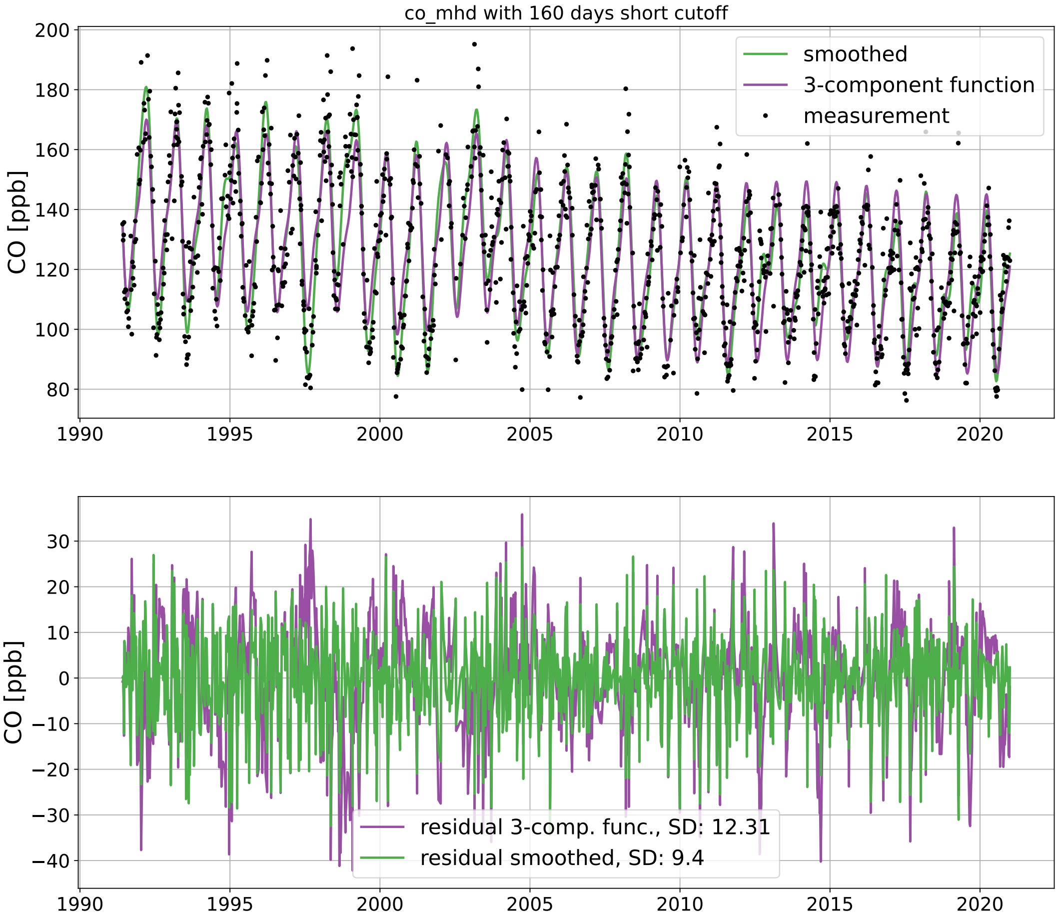

Fig. C.5 MHD CO fit with CCGCRV routine by Maksym Gachkivskyi (unpublished). While the 'smoothed' fit uses all tools in the CCGCRV routine, the '3-component function' is comprised of the polynomial, the harmonic and the inter-annual variation parts of the fit (no analysis of the residual). The short term cut-off parameter for the FFT was set to 160 days. The results from the 'smoothed' fit are used in the evaluation.

are not interrupted when air is collected. Consequently, integrated $\Delta^{14}CO_2$ samples collect in Heidelberg 12 h ambient air every day (18:00 UTC to 6:00 UTC), but the continuous data, which are needed to calculate two-week averages for the integrated $\Delta^{14}CO_2$ sampling periods, do not cover this period fully. I investigate how gaps in the data change means, first for a one-hour mean and then for the two-week integration periods. I am interested in an upper limit for gaps, which is still manageable. This has consequences for the choices I make when designing my thought experiment.

The CRDS (Picarro) instrument data (used 2019 to 2020) is averaged to hours from minutely values, with another column showing how many minutes m go into the hourly mean. For 2018 to 2020, 82.7 % of all hours have $m \geq 58$. Only 3.5 %

have $48 \leq m < 58$. I conducted the test described in this section for different cutoff criteria for m and found that it is not worth it to lower the threshold below $m \geq 58$, i.e. final results did not improve, while accuracy of hourly means were significantly worse. Consequently, I will present the results achieved with the threshold $m \geq 58$.

I calculate the mean uncertainty $\langle \delta X \rangle$ for 2018 to 2020 to estimate how hourly values usually fluctuate (X either CO or CO_2). To cover roughly 95 % of all possible fluctuations, I add twice the standard deviation to the mean. I find $\langle \delta CO_2 \rangle = 2.2 + 2 \cdot 2.5 = 7.2$ ppm and $\langle \delta CO \rangle = 8.8 + 2 \cdot 10.0 = 28.8$ ppb. I then follow the steps below to calculate the possible additional uncertainty $\delta^+ X$:

1. generate a 60-entry synthetic data set D, normally distributed with $\langle \delta X \rangle$ as standard deviation
2. sample 58 entries from the synthetic data set to create the sub-sample $S_i \subset D$ and calculate the mean
3. calculate the difference d_i between the mean of the sub-sample (58 entries) and the mean of the full sample (60 entries)
4. repeat the previous two steps 10000 times
5. calculate $\delta^+ X$ as the standard deviation of all d_i

Note that $\delta^+ X$ is not the mean bias, but the standard deviation of the bias, because this is a better representation of what the bias of an individual hour looks like (between $\pm\delta^+ X$). I find $\delta^+ CO_2 = 0.3$ ppm and $\delta^+ CO = 1.4$ ppb as the upper limit for the bias introduced to an hourly mean by missing 2 entries. Comparing this to the instrument uncertainties (0.1 ppm CO_2, 3 ppb CO) I find that the possible bias in CO_2 is larger than the instrument uncertainty, while for CO the instrument uncertainty is larger.

The question now is, how the means for the integrated samples are affected by hours with such increased uncertainties. On average, 29 hours out of $12 \cdot 14 = 168$ hours are based on less than 58 minutely values (randomly distributed, no more than two in succession). Of the remaining 139 hours, at most 12 are based on 58 to 59 minutely values (the rest has full 60 min coverage). The average variation of the 168-hour mean is ≈15 ppm CO_2 and ≈44 ppb CO. Similar to before, I follow the steps below to calculate the possible additional uncertainty $\Delta^+ X$ due to gaps:

1. generate a 168-entry synthetic data set B, normally distributed with $\langle \Delta X \rangle$ as standard deviation
2. sample $168 - 29 = 139$ entries from B to create the sub-sample $P_i \subset D$
3. sample 12 entries from P_i to create the sub-sub-sample $Q_i \subset P_i$

4. $\forall q \in Q_i$ add $\delta^+ X$ as standard deviation
5. calculate the difference ϵ_i between the sub-sample (139 entries, 12 of them with enlarged uncertainty) mean and the full sample (168 entries) mean
6. repeat four previous steps 10000 times
7. calculate $\Delta^+ X$ as the standard deviation of all ϵ_i

Note that, again, $\Delta^+ X$ is not the mean bias, but the standard deviation of the bias, because this is a better representation of what the bias of an individual hour looks like (between $\pm\Delta^+ X$). I find $\Delta^+CO_2 = 1.0\,\text{ppm}\ (2\,\sigma)$ and $\Delta^+CO = 3.0\,\text{ppb}\ (2\,\sigma)$ as the upper limit (therefore twice the standard deviation) for the bias introduced to an hourly mean by missing 29 entries and having 12 entries averaged over only 58 to 59 minutes (the number of such entries is of little consequence, even for 16, the maximum found, the result is the same at this decimal precision). A quick counter-check confirmed that the increased uncertainty for the hourly means does not affect the bias of the two-week mean. Rather, the bias is a result of the large variability of the occurring concentrations.

In conclusion, based on the occurring data gaps (on average 29 hours per sample of 168 hours), an additional uncertainty of $\Delta^+CO_2 = \pm 1.0\,\text{ppm}\ (2\,\sigma)$ and $\Delta^+CO = \pm 3.0\,\text{ppb}\ (2\,\sigma)$ is applied.

Final uncertainty calculation. For uncorrelated, random (i.e. stochastic) errors, Gaussian error propagation applies. That is, the root of the sum of squares of the errors yields the correct total error. The errors discussed above for measured CO_2, CO, $\Delta^{14}CO_2$ are the instrument or measurement error (Δ_{meas}), the representativeness error (Δ_{repre}), the fit uncertainty (Δ_{fit}) and the gap uncertainty (Δ_{gap}). Uncertainties for Delta$^{14}CO_2{}^{\text{nuc}}$ and $\Delta^{14}CO_2{}^{\text{bio}}$ were also discussed but only have one component and thus do not require an error propagation discussion.

Δ_{repre} is not stochastic, i.e. does not change from measurement to measurement, because it describes how uncertain my choice for the average winter background is. It applies to every measurement during one winter in the same way, so it is not stochastic. Δ_{meas} depends on the instrument, its calibration, and is essentially a result of the basic physical process of the measurement. Consequently, Δ_{meas} is stochastic and not correlated to other errors. Δ_{gap} is purely stochastic, as the derivation above clearly shows. It is correlated to the atmospheric concentration variability, not to Δ_{meas}. As it only applies to the Heidelberg station, it is automatically independent of the fit uncertainty, Δ_{fit}. The fit uncertainty (i.e. the standard deviation of the residuals between fit and measurements) necessarily arises when low-frequency data are fitted correctly (i.e. without over-fitting each point). By using a 3-part fit function with a polynomial, a harmonic and an

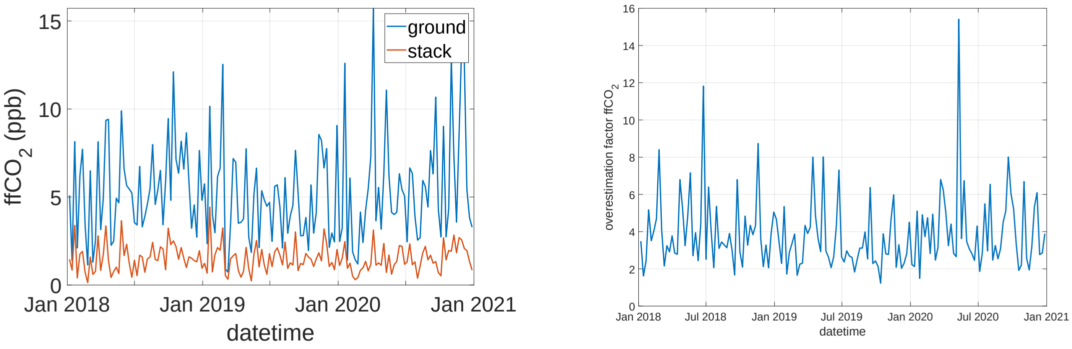

(a) Absolute difference.

(b) Relative difference.

Fig. C.6 Differences between volume source influence ansatz and surface source influence ansatz, adapted from PhD thesis Fabian Meier (unpublished). **(a)** Absolute difference in ffCO_2 between surface-source and volume-source influence ansatz, **(b)** Relative difference in ffCO_2 between surface-source ('ground') and volume-source ('stack') influence ansatz.

inter-annual component, we try to represent physical processes, i.e. a year-to-year trend (increase in case of CO_2, decrease in case of $\Delta^{14}CO_2$), a seasonal cycle and extraordinary events (e.g. a global pandemic), respectively. Conceptually, we can imagine the measurement points as results of the physical processes (represented by the fit) with statistical noise (instrument uncertainty, atmospheric variability) added on top. I argue that Δ_{fit} is the only way to account for atmospheric variability at the background site. In this capacity, it is not correlated to Δ_{meas}. Consequently, even though you could well argue that Δ_{fit} and Δ_{meas} are weakly correlated, I treat them as independent.

In conclusion, I calculate the total error for CO_2, CO, $\Delta^{14}CO_2$ of the background station Mace Head as

$$\Delta_{\mathrm{total}}^{\mathrm{MHD}} = \Delta_{\mathrm{repre}}^{\mathrm{MHD}} + \sqrt{\left(\Delta_{\mathrm{meas}}^{\mathrm{MHD}}\right)^2 + \left(\Delta_{\mathrm{fit}}^{\mathrm{MHD}}\right)^2}. \tag{C.4}$$

The total error for CO_2, CO, $\Delta^{14}CO_2$ of the Heidelberg station is

$$\Delta_{\mathrm{total}}^{\mathrm{HD}} = \sqrt{\left(\Delta_{\mathrm{meas}}^{\mathrm{HD}}\right)^2 + \left(\Delta_{\mathrm{gap}}^{\mathrm{HD}}\right)^2}. \tag{C.5}$$

C.4 Modelled emission ratio uncertainty calculations

Uncertainties for the modelled emission ratios are only based on the uncertainties of the TNO inventory emissions, uncertainties from atmospheric modelling are

Table C.1
Relative uncertainties for TNO inventory emissions for Germany for the year 2017, provided by Ingrid Super (personal communication October 1, 2020). Uncertainties are based on reported uncertainty ranges in NIR reports (for CO_2) and EEA guidelines (CO and NO_x) (Super et al., 2019).

Sector	Relative uncertainty (%)	
	CO_2	CO
Public power	2.93	23.10
Industry	2.69	1.21
Residential heating	4.11	22.14
Road transport	4.69	9.74

unknown and rectified by reducing point source emissions around Heidelberg, as described in Section 5.3. The reduction factor is the mean of the data shown in Fig. C.6b. Fig. C.6a shows the corresponding absolute difference. The uncertainties of the TNO inventory emissions are discussed below.

Necessary considerations. Super et al. (2019) analysed uncertainties in the TNO inventory emissions with a focus on Germany and surrounding countries, see Fig. C.7. The sector-specific relative uncertainties are shown in Table C.1. Note that the sector-specific relative uncertainties are CO and CO_2 for Germany in 2017. I apply them to the total modelled concentration enhancements, implicitly assuming that (1) 2017 is representative for all investigated years, (2) uncertainties for other countries are the same or at least similar and thus well represented by the given values and (3) the uncertainty for CO_2 approximates the uncertainty for ffCO_2. Ingrid Super provided insights on the first points via personal communication (April 26, 2022). According to her, 'uncertainties apply to all years in the reported time series', consequently assumption (1) is permissible. Regarding assumption (2), 'reported uncertainties do not differ much between European countries. There are some exceptions, but those are usually for very small sectors that have a high uncertainty. In the aggregated total, this will have a minor impact.' Pertaining point (3) – that the uncertainty for CO_2 approximates the uncertainty for ffCO_2 – the main argument is that bio fuels play a minor role for power plants, industry, traffic, even residential heating (where it depends on the region how high the bio fuel contribution is). Consequently, since most CO_2 is of fossil origin, the uncertainty for CO_2 approximates the uncertainty for ffCO_2 well.

Calculation. For each winter, I calculate total emission uncertainties as follows:

$$\Delta_{\mathrm{tot}'} = \delta^{\%}_{\mathrm{pp}} c_{\mathrm{pp}} + \delta^{\%}_{\mathrm{ind}} c_{\mathrm{ind}} + \delta^{\%}_{\mathrm{rh}} c_{\mathrm{rh}} + \delta^{\%}_{\mathrm{tr}} c_{\mathrm{tr}} \tag{C.6}$$

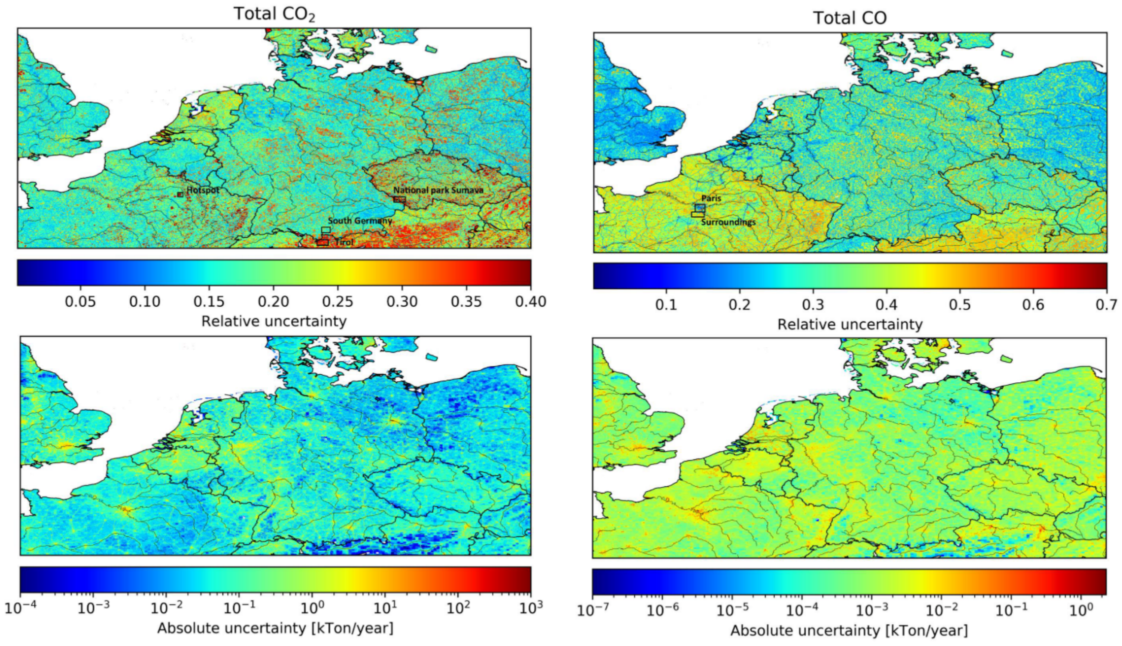

(a) CO$_2$ emission uncertainty.

(b) CO emission uncertainty.

Fig. C.7 Figures taken from Super et al. (2019, Figs. 14 and 15) showing absolute and relative uncertainties in emissions of TNO inventory.

where c is the modelled concentration enhancement in Heidelberg (either for ffCO$_2$ or CO) and $\delta^{\%}$ is the relative uncertainty given in Table C.1. The indices indicate the different sectors: pp – power plants, ind – industry, rh – residential heating and tr – traffic. These are not all the available sectors, only the ones responsible for $f \approx 97\,\%$ of all ffCO$_2$ emissions. To account for this, I assume the relative uncertainty of the remaining emissions are on average equal to $\Delta_{\text{tot}'}$ and calculate the 'true' total uncertainty as $\Delta_{\text{tot}} = \Delta_{\text{tot}'}/f$ (where f is calculated for each year). With this I calculate the total relative uncertainty

$$\delta^{\%}_{\text{tot}} = \frac{\Delta_{\text{tot}}}{c_{\text{tot}}}. \tag{C.7}$$

Using the Gaussian error propagation rule for quotients, the relative uncertainty of the ratio is

$$\Delta^{\%}\left(\frac{\text{CO}}{\text{ffCO}_2}\right) = \sqrt{\left(\delta^{\%}_{\text{tot}}\text{CO}\right)^2 + \left(\delta^{\%}_{\text{tot}}\text{ffCO}_2\right)^2} \tag{C.8}$$

It varies slightly from year to year, staying within the range 12 % to 14 %. The variations come from the different composition of the enhancements, e.g. a larger contribution from the industry sector reduces uncertainties in both ffCO$_2$ and CO.

Appendix D

Auxiliary data

Weighted total least square regressions for measured ratios displayed in Fig. 5.3, calculated according to Wurm (2022).

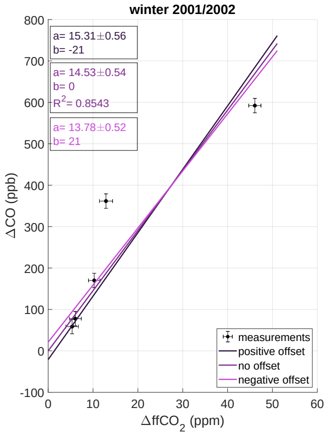

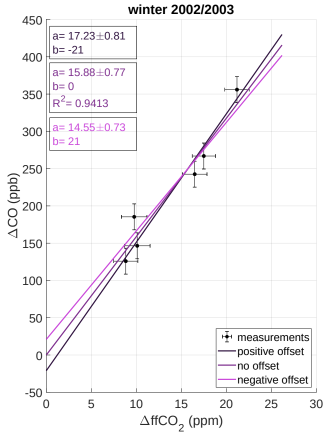

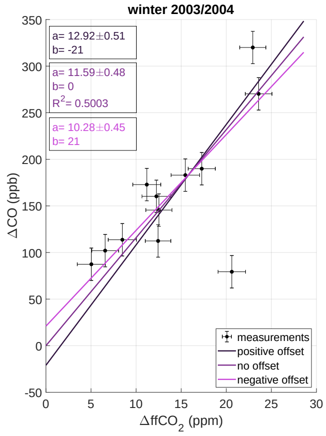

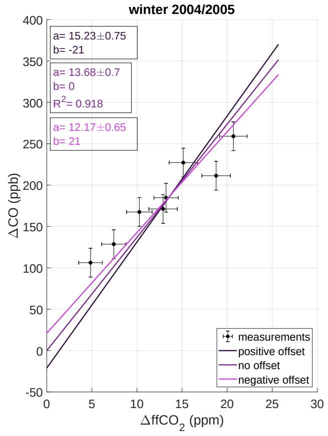

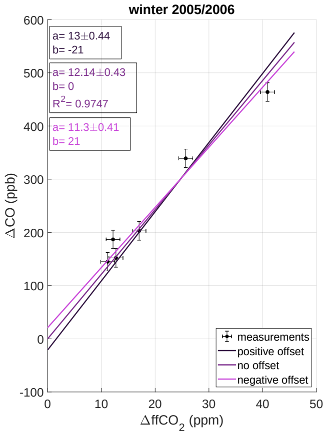

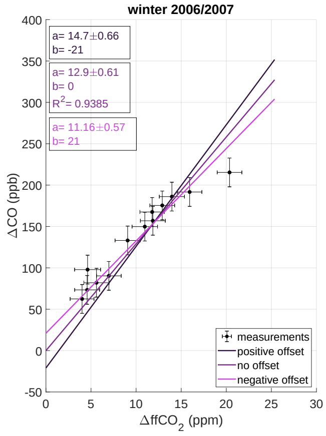

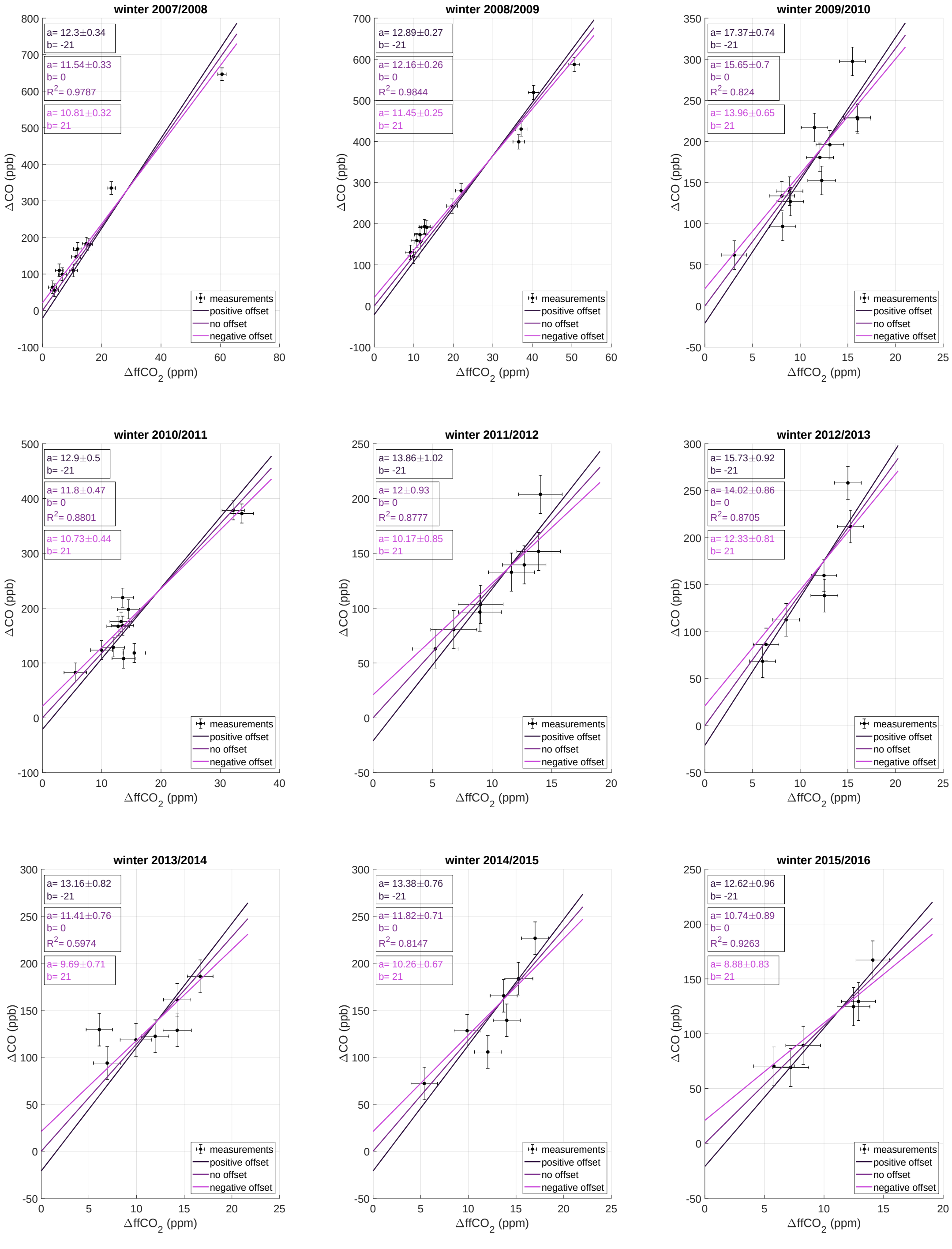
winter 2007/2008
a= 12.3±0.34
b= -21
a= 11.54±0.33
b= 0
R2= 0.9787
a= 10.81±0.32
b= 21
winter 2008/2009
a= 12.89±0.27
b= -21
a= 12.16±0.26
b= 0
R2= 0.9844
a= 11.45±0.25
b= 21
winter 2009/2010
a= 17.37±0.74
b= -21
a= 15.65±0.7
b= 0
R2= 0.824
a= 13.96±0.65
b= 21
winter 2010/2011
a= 12.9±0.5
b= -21
a= 11.8±0.47
b= 0
R2= 0.8801
a= 10.73±0.44
b= 21
winter 2011/2012
a= 13.86±1.02
b= -21
a= 12±0.93
b= 0
R2= 0.8777
a= 10.17±0.85
b= 21
winter 2012/2013
a= 15.73±0.92
b= -21
a= 14.02±0.86
b= 0
R2= 0.8705
a= 12.33±0.81
b= 21
winter 2013/2014
a= 13.16±0.82
b= -21
a= 11.41±0.76
b= 0
R2= 0.5974
a= 9.69±0.71
b= 21
winter 2014/2015
a= 13.38±0.76
b= -21
a= 11.82±0.71
b= 0
R2= 0.8147
a= 10.26±0.67
b= 21
winter 2015/2016
a= 12.62±0.96
b= -21
a= 10.74±0.89
b= 0
R2= 0.9263
a= 8.88±0.83
b= 21
ΔCO (ppb)
ΔffCO2 (ppm)
measurements
positive offset
no offset
negative offset

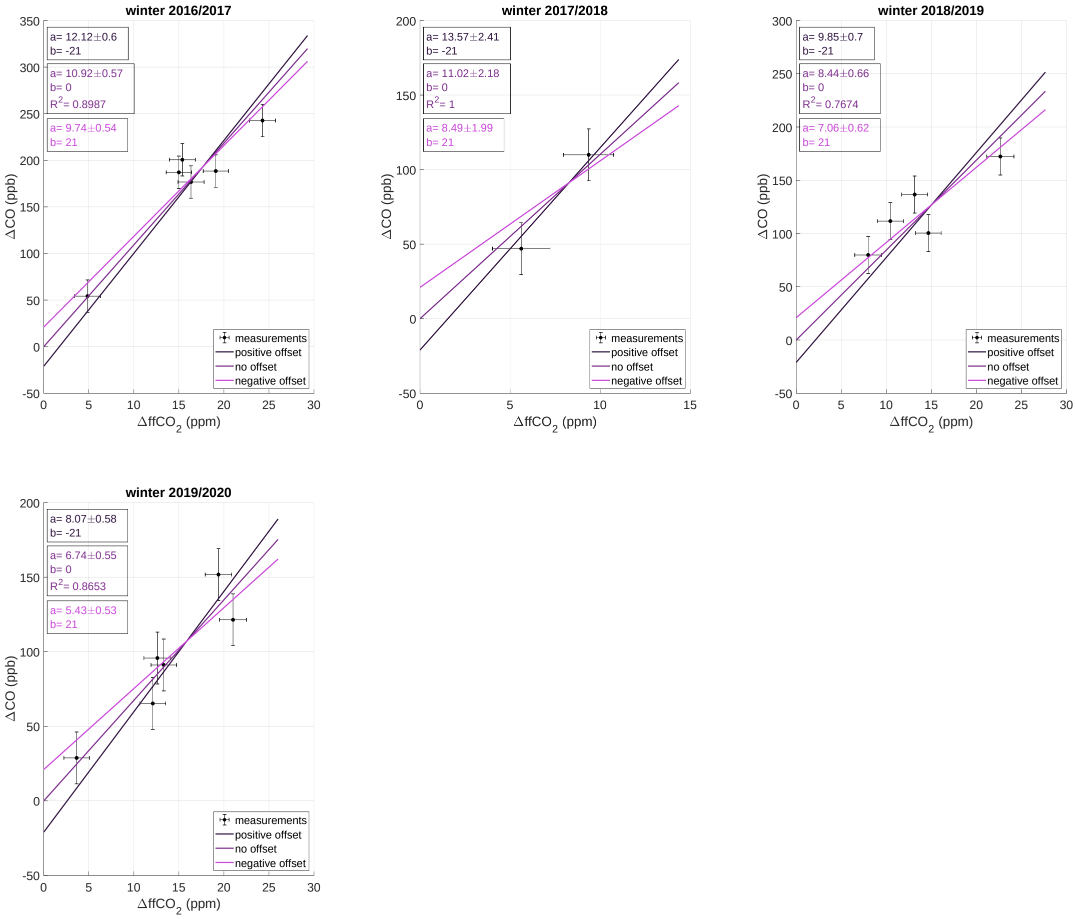
winter 2016/2017
a= 12.12±0.6
b= -21
a= 10.92±0.57
b= 0
R^2= 0.8987
a= 9.74±0.54
b= 21
ΔCO (ppb)
ΔffCO$_2$ (ppm)
measurements
positive offset
no offset
negative offset
winter 2017/2018
a= 13.57±2.41
b= -21
a= 11.02±2.18
b= 0
R^2= 1
a= 8.49±1.99
b= 21
winter 2018/2019
a= 9.85±0.7
b= -21
a= 8.44±0.66
b= 0
R^2= 0.7674
a= 7.06±0.62
b= 21
winter 2019/2020
a= 8.07±0.58
b= -21
a= 6.74±0.55
b= 0
R^2= 0.8653
a= 5.43±0.53
b= 21

Acknowledgements

This dissertation is the result of my work as a doctoral student at the Institute of Environmental Physics at the University of Heidelberg. On this occasion I would like to thank everyone who contributed to the success of this work.

I would like to thank Prof. Dr. Ingeborg Levin for her support and promotion of my scientific work, and the freedom she has given me. I thank Prof. Dr. Werner Aeschbach for his interest in my work and for reviewing this thesis. I also want to thank Dr. Samuel Hammer for his support and guidance.

This project has received funding from the European Union's Horizon 2020 research and innovation programme under grant agreement No 776810.

To Fabian Maier and Makysm Gachkivskyi, my fellow PhD students: thank you for all the practical help, providing data, or plots. But also, thank you for the moral support, for companionship, and enjoyable laid-back discussions.

Thanks to our technicians, Eva Gier, Sabine Kühr, Michael Sabasch, and especially Julian Della Coletta. Without Julian, the laboratory would simply not run. Thanks as well to our student assistants, who prepared samples in the CRL: Mahshid Homayou, Christopher Fuchs, Katharina Bews, and all the others.

Many master students did great work in our group during my PhD, all of them great colleagues. I thank Björn Peter, Christoph Rieß, Tobias Kneuer and Cornelia Jäschke. I also want to mention Lars Zipf, who finished his PhD just as I entered the group, who I had great conversations with.

At this point, a note of thanks to the Institute's workshop crew is appropriate. Thanks to Alexandra Mertens and Heribert Sommer, who helped in many medium-sized tasks around the MLs, and a special thanks to Ralph Pfeiffer, who help with planning, designing and setting everything up. Without these three and especially Ralph Pfeiffer, this would have been an insurmountable task.

Speaking of the mobile laboratories, the measurement campaigns would not have been possible without the support of the following people, who supplied power and place for the MLs: Samuel Hammer (Leimen), Mr. Schoisser (Wieblingen), Jochen Wallenwein (Gaiberg), Peter Beisel (Wieblingen) Peter Schollmeier and Bernd Ulrich (of THW Wieblingen). Special thanks to Bernd Ulrich, who would always come to open the gate for me and who I often had pleasant conversations with. Thanks to Marc Koch of Regierungspräsidium Tübingen for supplying hourly traffic data for the traffic campaign. Thanks to Wolfram Knörr of the Institut für Energie- und Umweltforschung (IFEU) for the TREMOD data. Special thanks to Stefan Hausberger who sat down with me on several occasions to discuss the results of the traffic campaign and who gave insight into how emission factors for the traffic sector are calculated. The FCL team in Jena deserves thanks as well, Armin Jordan, Markus Eritt, Richard Kneißl and Lars Borchardt, for help with flask sampling. Thank you to Denis Pöhler for help with the ICADs. David Griffith of University of Wollongong helped with the FTIR, thanks.

I want to thank my Verify collagues and especially the team of Hugo Denier van der Gon of TNO: Stijn Dellaert, Antoon Visschedijk, and Ingrid Super. They provided data as well as insight and helped in any way they could.

A big thank you to Doug Worthy and Larry Giroux of Toronto University, who provided the Picarro G2301. Thanks to Frank Meinhardt, who provided the Aerolaser instrument. Special thanks also to Olivier Laurant of LSCE who quickly supplied a Picarro G2401 when our instruments failed.

I cannot thank my friends enough: Noa, Daniel, Rainer, who started their studies together with me and stayed by my side all through today; Lukas, Marvin and Benedikt, the board game pals and fellow PhD students at the Institute. Many friends I met through Ultimate (Frisbee): René, Felix, Max, Marco, Friedrich, Julian, Florian, Celine, and many others, but especially Hein, who listened to me with never-ending patience and who showed me how easy it is to be vegan.

Last but not least, I want to thank my family. No words can express how grateful I am for my parents' support. I am also grateful to my brother Philipp, who helped in countless ways and inspires me to strive for more. Thank you.

References

I. air dryer. *https://www.icos-cal.eu/static/images/docs/Manual_ICOS_Air_Dryer.pdf*. Last accessed April 28, 2022.

L. Ammoura, A. Baudic, J.-E. Petit, N. Bonnaire, V. Gros, B. Bonsang, I. Xueref-Remy, J. Sciare, F. Chevallier, and O. Perrussel. Atmospheric measurements of ratios between CO2 and co-emitted species from traffic: a tunnel study in the Paris megacity. *Atmospheric Chemistry and Physics*, 14(23):12871–12882, 2014.

R. M. Andrew. A comparison of estimates of global carbon dioxide emissions from fossil carbon sources. *Earth System Science Data*, 12(2):1437–1465, 2020.

D. Archer, M. Eby, V. Brovkin, A. Ridgwell, L. Cao, U. Mikolajewicz, K. Caldeira, K. Matsumoto, G. Munhoven, A. Montenegro, and K. Tokos. Atmospheric lifetime of fossil fuel carbon dioxide. *Annual Review of Earth and Planetary Sciences*, 37:117–134, 2009.

Automatic traffic counts by Bundesanstalt für Straßenwesen. *https://www.bast.de/DE/Verkehrstechnik/Fachthemen/v2-verkehrszaehlung/Aktuell/zaehl_aktuell_node.html*. Last accessed April 28, 2022.

L. Bava, M. Zucali, A. Sandrucci, and A. Tamburini. Environmental impact of the typical heavy pig production in Italy. *Journal of Cleaner Production*, 140:685–691, 2017.

T. Bayes. An Essay Toward Solving a Problem in the Doctrine of Chances. *Philosophical Transactions of the Royal Society of London*, 1(53):370–418, 1764.

J. Beer, W. Mende, and R. Stellmacher. The role of the sun in climate forcing. *Quaternary Science Reviews*, 19(1-5):403–415, jan 2000.

Beta Analytic Inc. Introduction to Radiocarbon Determination by the Accelerator Mass Spectrometry Method. Technical report, Beta Analytic Limited, London, 2014.

G. A. Bishop and D. H. Stedman. A decade of on-road emissions measurements. *Environmental Science and Technology*, 42(5):1651–1656, 2008.

K. S. Bradley, K. B. Brooks, L. K. Hubbard, P. J. Popp, and D. H. Stedman. Motor vehicle fleet emissions by OP-FTIR. *Environmental Science and Technology*, 34(5): 897–899, 2000.

K. W. Busch and M. A. Busch, editors. *Cavity-Ringdown Spectroscopy*, volume 720 of *ACS Symposium Series*. American Chemical Society, Washington, DC, apr 1999.

M. O. Cambaliza, P. B. Shepson, J. Bogner, D. R. Caulton, B. Stirm, C. Sweeney, S. A. Montzka, K. R. Gurney, K. Spokas, O. E. Salmon, T. N. Lavoie, A. Hendricks, K. Mays, J. Turnbull, B. R. Miller, T. Lauvaux, K. Davis, A. Karion, B. Moser, C. Miller, C. Obermeyer, J. Whetstone, K. Prasad, N. Miles, and S. Richardson. Quantification and source apportionment of the methane emission flux from the city of Indianapolis. *Elementa*, 3:1–18, 2015.

Carbon Cycle Greenhouse gases Curve Fitting Methods. *https://gml.noaa.gov/ccgg/mbl/crvfit/crvfit.html*. Last accessed April 28, 2022.

Carbon Portal. *https://www.icos-cp.eu*. Last accessed April 28, 2022.

Cavity Ring-Down Spectroscopy. *https://www.picarro.com/company/technology/crds*. Last accessed April 28, 2022.

CDIAC. *https://cdiac.ess-dive.lbl.gov/trends/emis/overview_2013.html*. Last accessed April 28, 2022.

Climate Data Operators. *https://code.mpimet.mpg.de/projects/cdo*. Last accessed April 28, 2022.

P. J. Crutzen and J. Fishman. Average concentrations of OH in the troposphere, and the budgets of CH4, CO, H2 and CH3CCl3. *Geophysical Research Letters*, 4 (8):321–324, aug 1977.

K. J. Davis, A. Deng, T. Lauvaux, N. L. Miles, S. J. Richardson, D. P. Sarmiento, K. R. Gurney, R. M. Hardesty, T. A. Bonin, W. A. Brewer, B. K. Lamb, P. B. Shepson, R. M. Harvey, M. O. Cambaliza, C. Sweeney, J. C. Turnbull, J. Whetstone, and A. Karion. The Indianapolis Flux Experiment (INFLUX): A test-bed for developing urban greenhouse gas emission measurements. *Elementa*, 5, 2017.

D. Dell'Antonia, R. Gubiani, D. Maroncelli, and G. Pergher. Gaseous Emissions From Fossil Fuels and Biomass Combustion in Small Heating Appliances. *Journal of Agricultural Engineering*, 41(4):37, 2012.

H. Denier van der Gon, A. Visschedijk, H. van den Brugh, and R. Droge. A high resolution European emission data base for the year 2005. Technical report, Umweltbundesamt, Dessau-Roßlau, 2013.

H. A. Denier Van Der Gon, J. J. P. Kuenen, G. Janssens-Maenhout, U. Döring, S. Jonkers, and A. Visschedijk. TNO CAMS high resolution European emission inventory 2000–2014 for anthropogenic CO2 and future years following two different pathways. *Earth System Science Data Discussions*, 1(November):1–30, 2017.

S. Dey, G. C. Dhal, D. Mohan, and R. Prasad. Application of hopcalite catalyst for controlling carbon monoxide emission at cold-start emission conditions. *Journal of Traffic and Transportation Engineering (English Edition)*, 6(5):419–440, 2019.

S. Djuricin, D. E. Pataki, and X. Xu. A comparison of tracer methods for quantifying CO2 sources in an urban region. *Journal of Geophysical Research Atmospheres*, 115 (11):1–13, 2010.

H. Dörr and K. O. Münnich. Annual variation in soil respiration in selected areas of the temperate zone. *Tellus B*, 39 B(1-2):114–121, 1987.

H. Dorr and K. O. Munnich. 222Rn flux and soil air concentration profiles in West-Germany. Soil 222Rn as tracer for gas transport in the unsaturated soil zone. *Tellus, Series B*, 42 B(1):20–28, 1990.

EDGAR. *https://edgar.jrc.ec.europa.eu*. Last accessed April 28, 2022.

Emisia. *http://lat.eng.auth.gr/content/emisia-sa*. Last accessed April 28, 2022.

P. S. Farrugia and A. Micallef. Vectorial statistics for the standard deviation of wind direction. *Meteorology and Atmospheric Physics*, 129(5):495–506, 2017.

P. S. Farrugia, J. L. Borg, and A. Micallef. On the algorithms used to compute the standard deviation of wind direction. *Journal of Applied Meteorology and Climatology*, 48(10):2144–2151, 2009.

R. Friedrich and S. Hammer. How much bio is in fuel? *10th International Carbon Dioxide Conference*, 2017.

H. Gadd and S. Werner. Heat load patterns in district heating substations. *Applied Energy*, 108:176–183, 2013.

U. Gamnitzer, U. Karstens, B. Kromer, R. E. Neubert, H. A. Meijer, H. Schroeder, and I. Levin. Carbon monoxide: A quantitative tracer for fossil fuel CO<inf>2</inf>? *Journal of Geophysical Research Atmospheres*, 111(22):1–19, 2006.

C. Gerbig, D. Kley, A. Volz-Thomas, J. Kent, K. Dewey, and D. S. McKenna. Fast response resonance fluorescence CO measurements aboard the C-130: Instrument characterization and measurements made during North Atlantic Regional Experiment 1993. *Journal of Geophysical Research: Atmospheres*, 101 (D22):29229–29238, dec 1996.

P. Glarborg, J. A. Miller, B. Ruscic, and S. J. Klippenstein. Modeling nitrogen chemistry in combustion. *Progress in Energy and Combustion Science*, 67:31–68, 2018.

J. A. Gowlett. The discovery of fire by humans: A long and convoluted process. *Philosophical Transactions of the Royal Society B: Biological Sciences*, 371(1696), 2016.

H. D. Graven, B. B. Stephens, T. P. Guilderson, T. L. Campos, D. S. Schimel, J. E. Campbell, and R. F. Keeling. Vertical profiles of biospheric and fossil fuel-derived CO2 and fossil fuel CO2: CO ratios from airborne measurements of Δ14C, CO2 and CO above Colorado, USA. *Tellus, Series B: Chemical and Physical Meteorology*, 61(3):536–546, 2009.

D. W. Griffith. Synthetic calibration and quantitative analysis of gas-phase FT-IR spectra. *Applied spectroscopy*, 50(1):59–70, 1996.

R. L. Grob and E. F. Barry, editors. *Modern Practice of Gas Chromatography*. John Wiley & Sons, Inc., Hoboken, NJ, USA, 4 edition, may 2004.

M. Guevara, O. Jorba, C. Tena, H. Denier van der Gon, J. Kuenen, N. Elguindi-Solmon, S. Darras, C. Granier, and C. Pérez García-Pando. CAMS-TEMPO: global and European emission temporal profile maps for atmospheric chemistry modelling. *Earth System Science Data Discussions*, 1(February):1–60, 2020.

K. R. Gurney, I. Razlivanov, Y. Song, Y. Zhou, B. Benes, and M. Abdul-Massih. Quantification of fossil fuel CO2 emissions on the building/street scale for a large U.S. City. *Environmental Science and Technology*, 46(21):12194–12202, 2012.

S. Hammer, H. Glatzel-Mattheier, L. Müller, M. Sabasch, S. Schmitt, C. Schönherr, F. Vogel, D. E. Worthy, and I. Levin. A gas chromatographic system for high-precision quasi-continuous atmospheric. *Research Gate*, 2008.

S. Hammer, D. W. Griffith, G. Konrad, S. Vardag, C. Caldow, and I. Levin. Assessment of a multi-species in situ FTIR for precise atmospheric greenhouse gas observations. *Atmospheric Measurement Techniques*, 6(5):1153–1170, 2013.

S. Hammer, R. Friedrich, B. Kromer, A. Cherkinsky, S. J. Lehman, H. A. Meijer, T. Nakamura, V. Palonen, R. W. Reimer, A. M. Smith, J. R. Southon, S. Szidat, J. Turnbull, and M. Uchida. Compatibility of Atmospheric 14CO2 Measurements: Comparing the Heidelberg Low-Level Counting Facility to International Accelerator Mass Spectrometry (AMS) Laboratories. *Radiocarbon*, 59(3):875–883, 2017.

S. Hausberger, M. Rexeis, M. Zallinger, and R. Luz. Emission Factors from the Model PHEM for the HBEFA Version 3. Technical Report I, Graz University of Technology, 2009.

L. Hazan, J. Tarniewicz, M. Ramonet, O. Laurent, and A. Abbaris. Automatic processing of atmospheric CO2 and CH4 mole fractions at the ICOS Atmosphere Thematic Centre. *Atmospheric Measurement Techniques*, 9(9):4719–4736, 2016.

HBEFA. *https://www.hbefa.net/e/index.html*. Last accessed April 28, 2022.

Heidelberg ATC panel. *https://icos-atc.lsce.ipsl.fr/panelboard/HEI*. Last accessed April 28, 2022.

W. Heitkoetter, W. Medjroubi, T. Vogt, and C. Agert. Regionalised heat demand and power-to-heat capacities in Germany – An open dataset for assessing renewable energy integration. *Applied Energy*, 259(November 2019):114161, 2019.

W. Heitkoetter, W. Medjroubi, T. Vogt, and C. Agert. Regionalised heat demand and power-to-heat capacities in Germany – An open dataset for assessing renewable energy integration. *Applied Energy*, 259(June 2019):114161, 2020.

C. Helfter, A. H. Tremper, C. H. Halios, S. Kotthaus, A. Bjorkegren, C. S. B. Grimmond, J. F. Barlow, and E. Nemitz. Spatial and temporal variability of urban fluxes of methane, carbon monoxide and carbon dioxide above London, UK. *Atmospheric Chemistry and Physics*, 16(16):10543–10557, 2016.

A. M. Helmenstine. Gas Chromatography - What It Is and How It Works., 2021.

Hestia. *https://hestia.rc.nau.edu/About.html*. Last accessed April 28, 2022.

D. J. Hofmann, J. H. Butler, and P. P. Tans. A new look at atmospheric carbon dioxide. *Atmospheric Environment*, 43(12):2084–2086, 2009.

M. Horbanski, D. Pöhler, J. Lampel, and U. Platt. The ICAD (iterative cavity-enhanced DOAS) method. *Atmospheric Measurement Techniques*, 12(6):3365–3381, 2019.

ICOS CRL. *https://www.icos-cal.eu/crl*. Last accessed April 28, 2022.

ICOS Flask Sampler. *https://www.icos-cal.eu/static/images/docs/Manual_ICOS_Flask_Sampler.pdf*. Last accessed April 28, 2022.

Ifeu. *https://www.ifeu.de/en/*. Last accessed April 28, 2022.

Informative Inventory Report. *https://www.ceip.at/webdab-emission-database/reported-emissiondata*. Last accessed April 28, 2022.

Intergonvernmental Panel on Climate Change. *https://www.ipcc.ch*. Last accessed April 28, 2022.

IPCC. Fifth Assessment Report. Technical report, IPCC, Geneva, 2014.

C. Janssen, M. Schmidt, V. Gros, O. Perrussel, M. Lopez, P. Bousquet, A. Colomb, M. Ramonet, D. Mondelain, M. Delmotte, I. Xueref-Remy, and S. J. Lehman. CO, NOx and 13CO2 as tracers for fossil fuel CO2: results from a pilot study in Paris during winter 2010. *Atmospheric Chemistry and Physics*, 13(15):7343–7358, 2013.

L. S. Johansson, B. Leckner, L. Gustavsson, D. Cooper, C. Tullin, and A. Potter. Emission characteristics of modern and old-type residential boilers fired with wood logs and wood pellets. *Atmospheric Environment*, 38(25):4183–4195, 2004.

A. Jordan and M. Schumacher. Quality Control Report. Technical report, ICOS CAL-FCL, Jena, 2022.

J. Joyce. Bayes' Theorem. In E. N. Zalta, editor, *The Stanford Encyclopedia of Philosophy*. Metaphysics Research Lab, Stanford University, fall 2021 edition, 2021.

H. P. S. Juchem. *Straßenrand-Messungen der NO x -Emissionen von Fahrzeugen mit einem ICAD-Messgerät*. PhD thesis, Heidelberg, 2021.

U. Karstens, C. Schwingshackl, D. Schmithüsen, and I. Levin. A process-based 222Rn flux map for Europe and its comparison to long-term observations. *Atmospheric Chemistry and Physics Discussions*, 15(12):17397–17448, 2015.

M. Keller, S. Hausberger, C. Matzer, P. Wüthrich, and B. Notter. HBEFA. Technical Report April, Institute for internal combustion engines and thermodynamics, TU Graz, Graz, 2017.

T. Kneuer. *Fossil fuel CO2 from an industral area source based on a Lagrangian two station approach*. Master thesis, Heidelberg, 2020.

I. B. Konovalov, E. V. Berezin, P. Ciais, G. Broquet, R. V. Zhuravlev, and G. Janssens-Maenhout. Estimation of fossil-fuel CO2 emissions using satellite measurements of "proxy" species. *Atmospheric Chemistry and Physics*, 16(21):13509–13540, 2016.

B. Kromer and K. O. Münnich. Co2 Gas Proportional Counting in Radiocarbon Dating — Review and Perspective. In *Radiocarbon After Four Decades*, pages 184–197. Springer New York, New York, NY, 1992.

M. Krystek and M. Anton. A weighted total least-squares algorithm for fitting a straight line. *Measurement Science and Technology*, 18(11):3438–3442, 2007.

M. Kuderer, S. Hammer, and I. Levin. The influence of 14CO2 releases from regional nuclear facilities at the Heidelberg 14CO2 sampling site (1986-2014). *Atmospheric Chemistry and Physics*, 18(11):7951–7959, 2018.

J. Kuenen, S. Dellaert, A. Visschedijk, J. P. Jalkanen, I. Super, and H. Denier Van Der Gon. CAMS-REG-v4: a state-of-the-art high-resolution European emission inventory for air quality modelling. *Earth System Science Data*, 14(2):491–515, 2022.

J. J. Kuenen, A. J. Visschedijk, M. Jozwicka, and H. A. Denier Van Der Gon. TNO-MACC-II emission inventory; A multi-year (2003-2009) consistent high-resolution European emission inventory for air quality modelling. *Atmospheric Chemistry and Physics*, 14(20):10963–10976, 2014.

LandScan. *https://landscan.ornl.gov*. Last accessed April 28, 2022.

T. Lauvaux, N. L. Miles, A. Deng, S. J. Richardson, M. O. Cambaliza, K. J. Davis, B. Gaudet, K. R. Gurney, J. Huang, D. O'Keefe, Y. Song, A. Karion, T. Oda, R. Patarasuk, I. Razlivanov, D. Sarmiento, P. Shepson, C. Sweeney, J. Turnbull, and K. Wu. High-resolution atmospheric inversion of urban CO2 emissions during the dormant season of the Indianapolis flux experiment (INFLUX). *Journal of Geophysical Research*, 121(10):5213–5236, 2016.

I. Levin and U. Karstens. Inferring high-resolution fossil fuel CO2 records at continental sites from combined 14CO2 and CO observations. *Tellus, Series B: Chemical and Physical Meteorology*, 59(2):245–250, 2007.

I. Levin and C. Rödenbeck. Can the envisaged reductions of fossil fuel CO2 emissions be detected by atmospheric observations? *Naturwissenschaften*, 95(3): 203–208, 2008.

I. Levin, J. Schuchard, B. Kromer, and K. O. Münnich. The Continental European Suess Effect. *Radiocarbon*, 31(03):431–440, jul 1989.

I. Levin, M. Born, M. Cuntz, U. Langendörfer, S. Mantsch, T. Naegler, M. Schmidt, A. Varlagin, S. Verclas, and D. Wagenbach. Observations of atmospheric variability and soil exhalation rate of radon-222 at a Russian forest site. Technical approach and deployment for boundary layer studies. *Tellus B: Chemical and Physical Meteorology*, 54(5):462–475, 2002.

I. Levin, B. Kromer, M. Schmidt, and H. Sartorius. A novel approach for independent budgeting of fossil fuel CO2 over Europe by 14CO2 observations. *Geophysical Research Letters*, 30(23):1–5, 2003.

I. Levin, S. Hammer, B. Kromer, and F. Meinhardt. Radiocarbon observations in atmospheric CO2: Determining fossil fuel CO2 over Europe using Jungfraujoch observations as background. *Science of the Total Environment*, 391(2-3):211–216, 2008.

I. Levin, S. Hammer, E. Eichelmann, and F. R. Vogel. Verification of greenhouse gas emission reductions: The prospect of atmospheric monitoring in polluted areas. *Philosophical Transactions of the Royal Society A: Mathematical, Physical and Engineering Sciences*, 369(1943):1906–1924, 2011.

I. Levin, U. Karstens, M. Eritt, F. Maier, S. Arnold, D. Rzesanke, S. Hammer, M. Ramonet, G. Vítková, S. Conil, M. Heliasz, D. Kubistin, and M. Lindauer. A dedicated flask sampling strategy developed for Integrated Carbon Observation System (ICOS) stations based on CO2 and CO measurements and Stochastic Time-Inverted Lagrangian Transport (STILT) footprint modelling. *Atmospheric Chemistry and Physics*, 20(18):11161–11180, 2020.

J. C. Lin, C. Gerbig, S. C. Wofsy, A. E. Andrews, B. C. Daube, K. J. Davis, and C. A. Grainger. A near-field tool for simulating the upstream influence of atmospheric observations: The Stochastic Time-Inverted Lagrangian Transport (STILT) model. *Journal of Geophysical Research: Atmospheres*, 108(16), 2003.

J. Lux. *A new target preparation facility for high precision AMS measurements and strategies for efficient 14CO2 sampling*. Dissertation, Heidelberg, 2018.

F. Maier. *Testing flask sampling instruments and strategies for an optimal quantification of the fossil fuel emissions from hotspots*. Master thesis, Heidelberg, 2018.

F. Maier, C. Gerbig, I. Levin, I. Super, J. Marshall, and S. Hammer. Effects of point source emission heights in WRF-STILT: a step towards exploiting nocturnal observations in models. *Geoscientific Model Development Discussions*, 2021(December):1–25, 2021.

R. McDonald. Evaluation of Gas, Oil and Wood Pellet Fueled Residential Heating System Emissions Characteristics. Technical report, Brookhaven National laboratory, Upton, 2009.

N. L. Miles, S. J. Richardson, T. Lauvaux, K. J. Davis, N. V. Balashov, A. Deng, J. C. Turnbull, C. Sweeney, K. R. Gurney, R. Patarasuk, I. Razlivanov, M. O. L. Cambaliza, and P. B. Shepson. Quantification of urban atmospheric boundary layer greenhouse gas dry mole fraction enhancements in the dormant season: Results from the Indianapolis Flux Experiment (INFLUX). *Elementa*, 5, 2017.

N. L. Miles, K. J. Davis, S. J. Richardson, T. Lauvaux, D. K. Martins, A. J. Deng, N. Balashov, K. R. Gurney, J. Liang, G. Roest, J. A. Wang, and J. C. Turnbull. The influence of near-field fluxes on seasonal carbon dioxide enhancements: results from the Indianapolis Flux Experiment (INFLUX). *Carbon Balance and Management*, 16(1):1–15, 2021.

J. Miller, S. Lehman, C. Wolak, J. Turnbull, G. Dunn, H. Graven, R. Keeling, H. A. J. Meijer, A. T. Aerts-Bijma, S. W. L. Palstra, A. M. Smith, C. Allison, J. Southon, X. Xu, T. Nakazawa, S. Aoki, T. Nakamura, T. Guilderson, B. LaFranchi, H. Mukai, Y. Terao, M. Uchida, and M. Kondo. Initial Results of an Intercomparison of AMS-Based Atmospheric 14 CO 2 Measurements. *Radiocarbon*, 55(3):1475–1483, feb 2013.

I. model guide. *https://gaftp.epa.gov/Air/aqmg/SCRAM/models/other/isc3/isc3v2.pdf*. Last accessed April 28, 2022.

T. Naegler. *Simulating Bomb Radiocarbon: Implications for the Global Carbon Cycle*. Dissertation, Heidelberg, 2005.

T. Naegler and I. Levin. Biosphere-atmosphere gross carbon exchange flux and the δ13CO2 and Δ14CO2 disequilibria constrained by the biospheric excess radiocarbon inventory. *Journal of Geophysical Research Atmospheres*, 114(17):1–12, 2009a.

T. Naegler and I. Levin. Observation-based global biospheric excess radiocarbon inventory 1963-2005. *Journal of Geophysical Research Atmospheres*, 114(17):1–8, 2009b.

T. Nehrkorn, J. Eluszkiewicz, S. C. Wofsy, J. C. Lin, C. Gerbig, M. Longo, and S. Freitas. Coupled weather research and forecasting-stochastic time-inverted lagrangian transport (WRF-STILT) model. *Meteorology and Atmospheric Physics*, 107(1):51–64, 2010.

S. Newman, S. Jeong, M. L. Fischer, X. Xu, C. L. Haman, B. Lefer, S. Alvarez, B. Rappenglueck, E. A. Kort, A. E. Andrews, J. Peischl, K. R. Gurney, C. E. Miller, and Y. L. Yung. Diurnal tracking of anthropogenic CO2 emissions in the Los Angeles basin megacity during spring 2010. *Atmospheric Chemistry and Physics*, 13(8):4359–4372, 2013.

D. K. Nicks Jr, J. S. Holloway, T. B. Ryerson, R. W. Dissly, D. D. Parrish, G. J. Frost, M. Trainer, S. G. Donnelly, S. Schauffler, E. L. Atlas, G. Hübler, D. T. Sueper, and F. C. Fehsenfeld. Fossil-fueled power plants as a source of atmospheric carbon monoxide. *Journal of Environmental Monitoring*, 5(1):35–39, jan 2003.

NIR. *https://unfccc.int/documents/226313*. Last accessed April 28, 2022.

P. C. Novelli, K. A. Masarie, and P. M. Lang. Distributions and recent changes of carbon monoxide in the lower troposphere. *Journal of Geophysical Research Atmospheres*, 103(D15):19015–19033, 1998.

ODIAC. *http://odiac.org/index.html*. Last accessed April 28, 2022.

D. Paillard. Glacial Cycles: toward a new paragidm. *AGU*, 39(3):325–346, 2001.

F. Pasquill. The estimation of the dispersion of windborne material. *Australian Meteorological Magazin*, 90(1):33–49, 1961.

B. Peter. *Benchmarking of the TNO emission inventory based on in situ measurements of NOX, CO and ffCO2 at the Heidelberg sampling site*. Master thesis, Heidelberg, 2020.

U. Platt, D. Perner, and H. W. Pätz. Simultaneous measurement of atmospheric CH 2 O, O 3 , and NO 2 by differential optical absorption. *Journal of Geophysical Research*, 84(C10):6329, 1979.

U. Platt, J. Meinen, D. Pöhler, and T. Leisner. Broadband cavity enhanced differential optical absorption spectroscopy (CE-DOAS) - Applicability and corrections. *Atmospheric Measurement Techniques*, 2(2):713–723, 2009.

M. E. Popa, M. K. Vollmer, A. Jordan, W. A. Brand, S. L. Pathirana, M. Rothe, and T. Röckmann. Vehicle emissions of greenhouse gases and related tracers from a tunnel study: CO : CO2, N2O : CO2, CH4 : CO2, O2 : CO2 ratios, and the stable isotopes 13C and 18O in CO2 and CO. *Atmospheric Chemistry and Physics*, 14(4): 2105–2123, feb 2014.

M. J. Potosnak, S. C. Wofsy, A. S. Denning, T. J. Conway, J. W. Munger, and D. H. Barnes. Influence of biotic exchange and combustion sources on atmospheric CO2 concentrations in New England from observations at a forest flux tower. *Journal of Geophysical Research Atmospheres*, 104(D8):9561–9569, 1999.

M. Reuter, M. Buchwitz, O. Schneising, S. Krautwurst, C. W. O'Dell, A. Richter, H. Bovensmann, and J. P. Burrows. Towards monitoring localized CO2 emissions from space: Co-located regional CO2 and NO2 enhancements observed by the OCO-2 and S5P satellites. *Atmospheric Chemistry and Physics*, 19(14):9371–9383, 2019.

S. J. Richardson, N. L. Miles, K. J. Davis, T. Lauvaux, D. K. Martins, J. C. Turnbull, K. McKain, C. Sweeney, and M. O. L. Cambaliza. Tower measurement network of in-situ CO 2 , CH 4 , and CO in support of the Indianapolis FLUX (INFLUX) Experiment. *Elementa*, 5, 2017.

C. Rieß. *Setup and first results of a two-station based monitoring of urban fossil fuel emissions in the upper Rhine valley and the Paris metropolitan area*. Master thesis, Heidelberg, 2019.

RINGO. *http://www.ringo-project.eu*. Last accessed Mai 1, 2022.

C. Rosendahl, S. Hammer, C. Alberti, and F. Hase. Observation-based system for monitoring and verification of greenhouse gases. Technical report, University Heidelberg, Karlsruhe Institute of Technology, 2021.

K. N. Schuldt, T. Aalto, A. Andrews, B. Baier, P. Bergamaschi, and T. Biermann. Multi-laboratory compilation of atmospheric carbon monoxide data for the period 1989-2020 (GLOBALVIEWplus v2.0). Technical report, NOAA Earth System Research Laboratory, Global Monitoring Laboratory, 2021a.

K. N. Schuldt, J. Mund, and I. T. Luijkx. Multi-laboratory compilation of atmospheric carbon dioxide data for the period 1957-2020 (GLOBALVIEWplus v7.0). Technical report, NOAA Earth System Research Laboratory, Global Monitoring Laboratory, 2021b.

U. Schulzweida. CDO User Guide (Version 2.0.0). Technical report, MPI-MET, Hamburg, 2021.

M. Stuiver and H. A. Polach. Discussion Reporting of 14 C Data. *Radiocarbon*, 19 (3):355–363, jul 1977.

H. E. Suess. Radiocarbon Concentration in Modern Wood. *Science*, 122(3166): 415–417, sep 1955.

I. Super, H. A. Denier van der Gon, A. J. Visschedijk, M. M. Moerman, H. Chen, M. K. van der Molen, and W. Peters. Interpreting continuous in-situ observations of carbon dioxide and carbon monoxide in the urban port area of Rotterdam. *Atmospheric Pollution Research*, 8(1):174–187, 2017.

I. Super, S. N. C. Dellaert, A. J. H. Visschedijk, and H. A. C. D. V. D. Gon. Uncertainty analysis of a European high-resolution emission inventory of CO 2 and CO to support inverse modelling and network design. *Atmospheric Chemistry and Physics Discussions*, 2019.

I. Super, S. N. Dellaert, A. J. Visschedijk, and H. A. Van Der Gon. Uncertainty analysis of a European high-resolution emission inventory of CO2 and CO to support inverse modelling and network design. *Atmospheric Chemistry and Physics*, 20(3):1795–1816, 2020.

U. Tietge, J. Dornoff, S. Dìaz, P. Mock, M. Allekotte, C. Heidt, W. Knörr, H.-J. Althaus, B. Notter, Q. Oberpriller, A. Läderach, S. Hausberger, C. Matzer, C. Eisenmann, and T. Kuhnimhof. Erarbeitung einer Methode zur Ermittlung und Modellierung der CO2-Emissionen des Kfz-Verkehrs. Technical report, Umweltbundesamt, Dessau-Rosslau, 2020.

TREMOD. *https://www.ifeu.de/en/project/uba-tremod-2019/*. Last accessed April 28, 2022.

J. C. Turnbull, J. B. Miller, S. J. Lehman, P. P. Tans, R. J. Sparks, and J. Southon. Comparison of 14CO2, CO, and SF6 as tracers for recently added fossil fuel CO2 in the atmosphere and implications for biological CO2 exchange. *Geophysical Research Letters*, 33(1):2–6, 2006.

J. C. Turnbull, C. Sweeney, A. Karion, T. Newberger, S. J. Lehman, P. P. Tans, K. J. Davis, T. Lauvaux, N. L. Miles, S. J. Richardson, M. O. Cambaliza, P. B. Shepson, K. Gurney, R. Patarasuk, and I. Razlivanov. Toward quantification and source sector identification of fossil fuel CO 2 emissions from an urban area: Results from the INFLUX experiment. *Journal of Geophysical Research: Atmospheres*, 120 (1):292–312, jan 2015.

J. C. Turnbull, S. E. Fletcher, I. Ansell, G. W. Brailsford, R. C. Moss, M. W. Norris, and K. Steinkamp. Sixty years of radiocarbon dioxide measurements at Wellington, New Zealand: 1954-2014. *Atmospheric Chemistry and Physics*, 17(23): 14771–14784, 2017.

D. B. Turner. *Workbook of atmospheric dispersion estimates*. U. S. Department of Health, Education, and Welfare, Cincinnati, 1970.

Umweltbundesamt. *https://www.umweltbundesamt.de*. Last accessed April 28, 2022.

UNFCCC. *https://unfccc.int*. Last accessed April 28, 2022.

T. Varga, I. Major, V. Gergely, A. Lencsés, T. Bujtás, A. J. Jull, M. Veres, and M. Molnár. Radiocarbon in the atmospheric gases and PM10 aerosol around the Paks Nuclear Power Plant, Hungary. *Journal of Environmental Radioactivity*, 237(May), 2021.

Vehicle Groups according to Bundesamt für Straßenwesen. *https://www.bast.de/DE/Verkehrstechnik/Fachthemen/v2-verkehrszaehlung/pdf-dateien/erfassungsarten.pdf*. Last accessed April 28, 2022.

F. R. Vogel, S. Hammer, A. Steinhof, B. Kromer, and I. Levin. Implication of weekly and diurnal 14C calibration on hourly estimates of CO-based fossil fuel CO2 at a moderately polluted site in southwestern Germany. *Tellus, Series B: Chemical and Physical Meteorology*, 62(5):512–520, 2010.

M. K. Vollmer, N. Juergens, M. Steinbacher, S. Reimann, M. Weilenmann, and B. Buchmann. Road vehicle emissions of molecular hydrogen (H2) from a tunnel study. *Atmospheric Environment*, 41(37):8355–8369, 2007.

M. K. Vollmer, S. Walter, S. W. Bond, P. Soltic, and T. Röckmann. Molecular hydrogen (H2) emissions and their isotopic signatures (H/D) from a motor vehicle: Implications on atmospheric H2. *Atmospheric Chemistry and Physics*, 10 (12):5707–5718, 2010.

T. J. Wallington, E. W. Kaiser, and J. T. Farrell. Automotive fuels and internal combustion engines: A chemical perspective. *Chemical Society Reviews*, 35(4): 335–347, 2006.

M. Weiss, P. Bonnel, J. Kühlwein, A. Provenza, U. Lambrecht, S. Alessandrini, M. Carriero, R. Colombo, F. Forni, G. Lanappe, P. Le Lijour, U. Manfredi, F. Montigny, and M. Sculati. Will Euro 6 reduce the NO x emissions of new diesel cars? - Insights from on-road tests with Portable Emissions Measurement Systems (PEMS). *Atmospheric Environment*, 62(2):657–665, 2012.

K. M. Win, T. Persson, and C. Bales. Particles and gaseous emissions from realistic operation of residential wood pellet heating systems. *Atmospheric Environment*, 59:320–327, 2012.

M. Wurm. A universal and fast method to solve linear systems with correlated coefficients using weighted total least squares. *Measurement Science and Technology*, 33(1), 2022.

Y. B. Zeldovich. The oxidation of nitrogen in combustion and explosions. *Acta Physicochem USSR*, 21(1):577–628, 1946.

A. Zondervan and H. A. J. Meijer. Isotopic characterisation of CO2 sources during regional pollution events using isotopic and radiocarbon analysis. *Tellus B*, 48 (4):601–612, sep 1996.

This document has 143 references.